Modeling the atmospheric propagation of electromagnetic waves in 2D and 3D using fourier and wavelet transforms

Hang Zhou

THÈSE

En vue de l'obtention du

DOCTORAT DE L'UNIVERSITÉ DE TOULOUSE

Délivré par : *l'Université Toulouse 3 Paul Sabatier (UT3 Paul Sabatier)*

Présentée et soutenue le *6 avril 2018* **par :**

HANG ZHOU

Modélisation de la Propagation Atmosphérique d'Ondes Electromagnétiques en 2D et 3D à Partir de Transformées de Fourier et en Ondelettes

Modeling the Atmospheric Propagation of Electromagnetic Waves in 2D and 3D Using Fourier and Wavelet Transforms

---

JURY

FUNDA AKLEMAN	Professeur	Rapporteur
CHRISTOPHE BOURLIER	Directeur de Recherche CNRS	Rapporteur
ALEXANDRE CHABORY	Enseignant-Chercheur HDR	Co-Directeur
RÉMI DOUVENOT	Enseignant-Chercheur	Directeur
OLIVIER PASCAL	Professeur	Examinateur
PHILIPPE POULIGUEN	Ingénieur HDR	Examinateur

École doctorale et spécialité :
GEET : Électromagnétisme et Systèmes Haute Fréquence
Unité de Recherche :
ENAC Lab - Equipe TELECOM
Directeur(s) de Thèse :
Rémi Douvenot et *Alexandre Chabory*
Rapporteurs :
Funda Akleman et *Christophe Bourlier*

Acknowledgments

Foremost, I would like to express my sincere gratitude to my supervisors Dr. Rémi DOUVENOT and Dr. Alexandre CHABORY. Their patient guidance, friendly advice, and immense knowledge have helped me a lot. Studying and living in ENAC have really been a fantastic period of time. With your guidance, I have made progress on both knowledge and studying methodology. With responsible supervisors as you, my study has been motivated and full of fun.

I would also like to thank my committee members, Dr. Funda Akleman, Dr. Christophe Bourlier, Dr. Olivier Pascal, and Dr. Philippe Pouliguen. Thank you very much for your constructive and brilliant questions, comments and suggestions. The Ph.D. defense will always be a precious memory in my life.

I gratefully acknowledge the support and generosity of Civil Aviation University of China without which the present study could not have been completed. The colleagues of the Sino-European Institute of Aviation Engineering have given me a lot of supports. I am always grateful for being chosen to study abroad and I am looking forward to work with you in the future.

Thanks to all my friends in ENAC and ISAE-Supaero. With you, I have felt happy since the first time I arrived in Toulouse. Thanks for all your helps in these years. In addition, it is my honor for having joined the two most important associations of Chinese students in Toulouse: UCECF-ST and AASFC. It has been my pleasure to work with you.

Moreover, I wish to thank my parents Xiangming Zhou and Baoqin Zhang, for their support and encouragement throughout my study. They are concern with my life and study. In my heart, they are the best parents among the world. No matter what difficulties I come across, I know that they always stand behind me. Here, give my deepest gratitude to you.

Especially, thanks to my girl friend Yuwei Zhao. Long-distance relationship and six or seven hours of time difference make us know better how to cherish. Warm words and encourages stimulate me into working still harder. Thanks to you, everyday is full of sunshine.

Contents

Introduction

Context

The long-range electromagnetic wave propagation is a major issue in the domain of radio frequencies. There exists a need for fast and accurate methods for predicting the propagation at large distances, up to several hundreds of kilometers. Up to now, a large number of methods have been developed for this purpose, but are either fast or accurate.

The fields of applications of these modeling tools are numerous. They concern the terrestrial, naval, airborne, and space systems that are used for communication, surveillance, navigation, and observation both in civil and defense domains.

In the context of civil aviation systems [7], such methods are particularly important for the definition, design, and implementation of ground facilities associated with communication (air-ground vocal and data links), navigation (VOR, DME, and GBAS), and surveillance (primary and secondary radar, multilateration) systems. The possible applications are: choice of the best location for a ground antenna taking into account the local topology of the terrain, analysis of the perturbations observed on existing systems in particular meteorological conditions (ducts, etc.), impact of the implementation of man-made structures, such as windfarms or solar farms, on the system performances [8][9].

Besides, the prediction of the propagation is also a key-element during the definition phase of new systems because it allows to estimate the coverage and performances in different scenarii, e.g., in different atmospheric/meteorological conditions. The context of civil aviation systems renders this problem particularly complex to tackle because of the primary importance of safety, which means that the accuracy of the model must be completely mastered for any system and environment.

The lowest layer of Earth's atmosphere - the troposphere - plays a major role in the domain of radio communications. This layer contains most of the oxygen and almost all the atmospheric water vapors. Many weather phenomenons, e.g. cloud formation, also occur in the troposphere. At radiowave frequencies, the propagation is affected mainly by scattering, absorption, turbulence, and refraction. The scattering refers to the field diffusion by small particles suspended in a medium, like ice or water drops. Moreover, atmospheric molecules can absorb radiowaves, especially in the absorption bands of water vapor and oxygen. The scattering and absorption lead to an attenuation of the field. The turbulence refers to small-variation of the atmosphere characteristics and leads to signal

fluctuations. The refraction is the large-scale variation of the atmosphere parameters, which affects the field distribution in space, resulting in bending or ducting effects. These phenomenons are characterized by a parameter, which is the refraction index [10][11].

In the low atmosphere, the ground characteristics also affect the propagation. Over the sea, the interface is planar and can be approximated at first order by a perfect conducting condition. A more accurate model is required for the propagation over a dielectric ground or over rough surfaces [12][13]. Moreover, the presence of relief also has a major influence since it induces reflections and diffractions [12].

State of the art

We begin by explaining how the atmosphere is described from an electromagnetic point of view. Then propagation models are reviewed going from general computational electromagnetic tools to the specific tools dedicated to the atmospheric environment. The last element of the state-of-the-art concerns models based on a self-consistent discrete electromagnetic theory.

Atmosphere description

The refraction is characterized by the variable refractive index, which mainly depends on vapor pressure, temperature, and atmospheric pressure. These are the main meteorological parameters that have a strong influence on the radio waves propagation in the troposphere [14]. In order to estimate atmospheric effects, there exists many refraction index models, such as the ones proposed by the international telecommunication union (ITU) [15]. The refraction index can also be obtained from weather models as the weather research and forecasting model (WRF) [16].

Propagation methods

There exists a variety of numerical methods for the propagation of electromagnetic fields. These methods can be grouped in two main branches: rigorous and asymptotic methods. With rigorous methods, exact equations derived from Maxwell's equations are numerically solved. With asymptotic methods, approximated equations are solved by assuming a parameter tends towards either zero or infinity.

Rigorous methods refer to methods where no approximation is assumed. They include the finite-difference time-domain (FDTD) method [17], the finite element method (FEM) [18], and the method of moments (MoM) [19][20]. They usually require fine spatial and/or temporal meshes of spatial size, typically of order $\lambda/8$. For a wave propagation at 1 GHz, the mesh size is thus about 4 cm. Consequently, for our application, *i.e.* long-range propagation, they require huge computer resources. Thus, these methods are not suitable.

Another group of methods are based on approximate formulations. They are more suitable for modeling the propagation at large distances. Ray tracing [21], physical optics (PO)

[22], parabolic equation (PE) [23], and Gaussian/wavelet-based methods [24] are the major tools to tackle long distance propagation problems.

The ray tracing method is based on ray optics which solves the Maxwell's equations in the high-frequency regime. The concept of ray is used in Geometrical Optics (GO) [25][21] and the Uniform Theory of Diffraction (UTD) [26][27]. In our application, refraction of the atmosphere yields bent rays while the interaction with the ground induces reflected and diffracted rays. As the environment becomes more complex, the number of rays significantly increases which drastically increases the computation time.

Physical optics is an asymptotic method that treats well an interface of large size in a homogeneous medium. This method can be used for simulating the propagation over a smooth ground in a homogeneous atmosphere. However, it cannot handle an inhomogeneous atmosphere, *i.e.*, with a variable index of refraction. Besides, its accuracy worsens when the relief variation increases. In addition, it does not work well at grazing angles.

Parabolic equation methods

To predict the propagation of electromagnetic waves over the ground at large distances, the methods based on the parabolic approximation are good candidates. The parabolic approximation was introduced by Feit and Fock [28] in 2D. Since then, this method has been widely studied to model the electromagnetic propagation in complex atmospheric environments.

The first numerical schemes for PE were based on Finite-Differences (FD) [29]. Split-step Fourier (SSF) methods are more recent. They have been derived by Hardin and Tappert [30]. They are more efficient because they permit larger mesh increments. They are widely used for long-range acoustic and radio wave propagations [31][23][12]. Such methods can generally take into account the terrain profile, a possible ground wave, and the electrical characteristics of the atmosphere [12]. An impedance ground can also be modeled by using the discrete mixed Fourier transform (DMFT) proposed by Dockery and Kuttler [32]. These methods were initially applied in 2D due to the computation burden of 3D scenes.

Since the computational ability increased rapidly after 1980, propagation methods in 3D have been developed. FD and SSF have been used for acoustic propagation under the sea [33][34][35][36]. These 3D methods model the lateral couplings. Later on, for electromagnetic propagation, extensions to 3D of split-step Fourier methods have been developed in Cartesian coordinates [37][38][39].

Propagation methods based on Gaussian and wavelet decompositions

Gaussian beams have firstly been used in the domain of optics to solve analytically the paraxial propagation of lasers beams [40][41]. In the radio frequency domain, formulations of Gaussian beams have also been extensively studied [42][43][44]. For modeling the propagation of any fields, a preliminary decomposition on a set of elementary beams is performed. Lots of decomposition methods have been developed, including multimodal decompositions [45][46][47], the Gabor decomposition [48][49][50][51][52][53],

or other physics-based decompositions [54][55][56][57][58][59] for describing the radiation from apertures in 2D and 3D. For our application, this method can model the refraction effects [60][29]. However, relief with large variations can not be considered.

Another decomposition method, the wavelet transform, has similarities with the Gabor transform [61][62]. The signal is also expanded on elementary wavelike functions. It is a very efficient tool for data compression and analysis. Moreover, it has a higher computation efficiency than the Gabor decomposition and the Fourier transform. A wavelet-based algorithm has already been proposed to solve PE [63][64]. This method has the ability to model the propagation as accurately as SSF. The refraction and the ground conditions are also considered. However, the computation complexity is the same as SSF since Fourier transforms are used. Thus, the efficiency is not improved compared to SSF.

Self-consistency

The discrete electromagnetic theory [65][66] aims at developing a self-consistent electromagnetic theory on a discrete grid. Derivatives in the continuous equations are replaced by finite-differences in the discrete domain. The self-consistency avoids spurious solutions in the numerical computation.

For propagation modeling, the discrete mixed Fourier transform (DMFT) [32] has been a first effort towards this discrete formulation. Indeed, the transform is obtained in the discrete domain by expressing the vertical derivation of the field with a finite-difference approximation.

Objectives

The objective of this Ph.D. thesis is to develop a fast and self-consistent method for modeling the tropospheric propagation for both 2D and 3D complex environments. More precisely, this work focuses on the refraction effect of the atmosphere and the impacts of the ground characteristics or relief. Moreover, the methods will be self-consistent in the discrete domain to avoid spurious errors. Finally, the methods shall be computationally efficient, which could be achieved by means of wavelets.

In this thesis, three main research axes towards this objective are investigated:

I. Based on the split-step Fourier and parabolic equation methods, a self-consistent method in the discrete domain is developed in 2D.

II. Directly derived from the propagation equation, a self-consistent propagation method in the discrete domain is developed in 3D. In addition, a sectoral propagation method is presented to alleviate the computation burden.

III. To improve the computation efficiency, the wavelet decomposition and compression are used. A new split-step wavelet method is proposed. The objective is to have a better efficiency than SSF while keeping a good accuracy.

Outline

The thesis is composed of four chapters:

In the **first chapter**, the objective is to develop propagation methods in 2D. The parabolic equation and the split-step Fourier method are presented. In the first five sections, the methods for the propagation over a PEC ground are presented. The method with a continuous formulation is reminded and a self-consistent method in the discrete domain is introduced. In Section 6, the methods for the propagation over a dielectric ground are presented. Apodization, refractivity and irregular relief are also modeled. Numerical experiments are performed to test the methods and to compare classical and self-consistent formulations.

In the **second chapter**, the objective is to derive propagation methods over a PEC or an impedance ground in 3D cylindrical coordinates. Methods derived from the continuous and discrete equations are both presented. Then the explicit numerical scheme in an inhomogeneous atmosphere is obtained from the phase screens and the split-step algorithm. In addition, a sectoral propagation is introduced to reduce the computation time. Finally, numerical tests are performed in different environments to show the accuracy of the method.

In the **third chapter**, the objective is to present the discrete wavelet transform. The multilevel analysis, the fast wavelet transform, and data compression are exposed. The choice of the wavelet parameters is discussed and numerical tests are performed to compare the compression results.

In the **fourth chapter**, the objective is to develop a split-step wavelet method, which is an alternative method to SSF by replacing the Fourier transform by the wavelet transform. This new method is described. Domain truncation, ground condition, irregular atmosphere, and relief are also considered. Then, the computational complexities of the split-step wavelet and split-step Fourier methods are compared. Numerical tests are performed to show the accuracy and computational efficiency of the split-step wavelet method.

Chapter 1

2D Discrete Split-Step Fourier Method

1.1 Introduction

1.1.1 State of the art

Parabolic equation (PE) methods are among the most reliable numerical methods to simulate the propagation in an inhomogeneous atmosphere. They are based on an approximation of the wave equation valid along a paraxial direction and neglecting backward propagation [23].

The two most used methods for applying PE are based on the finite-difference (FD) method [29] and the split-step Fourier (SSF) method [30]. The FD method has the advantage of a straightforward implementation of complex boundaries. However, SSF is more numerically efficient because it permits larger mesh increments. Consequently, SSF is widely used for long-range wave propagation. The computation is performed marching on in distance. At each step, the wave is transformed from the spatial to the spectral domain by applying a spectral transform along the vertical.

Refractivity, ground boundary condition, and irregular relief can be considered in SSF. The phase-screens method is applied to take into account the refractivity in the spatial domain [12]. The relief can be modeled by various algorithms [12][31][67][68].

A spectral transform consistent with the boundary condition is chosen to consider the ground composition. A perfectly conducting ground is accounted by a sine or cosine transform depending on the polarization. A dielectric ground is approximated by an impedance boundary condition. Then, to model the propagation over an impedance ground, the discrete mixed Fourier transform (DMFT) has been proposed by Dockery and Kuttler [32].

1.1.2 Self-consistency: a motivation for a discrete formulation

The concept of a self-consistent electromagnetic theory on a regular lattice has been derived by Chew [65]. The discrete forms of many electromagnetic theorems have notably been demonstrated. The preservation of these theorems implies that the use of this discretized form of Maxwell equations for numerical simulation will not give rise to spurious solutions.

Our aim is to model the propagation in an inhomogeneous atmosphere over a metallic or an impedance ground with an irregular relief.

To overcome the inconsistencies in existing SSF methods, a discrete formulation is proposed. The complete method is derived from discrete equations. Therefore, it is self-consistent.

1.1.3 Outline

In Section G.1.2, the configuration is presented. Firstly, the methods for the propagation over a PEC ground are presented. The continuous formulation is exposed in Section G.1.5. This method is discretized in Section 1.4. A self-consistent method, i.e. derived directly in the discrete domain is proposed in Section 1.5. The methods with a PEC ground are synthesized in Section 1.6. Secondly, the methods for the propagation over a dielectric ground are presented in Section 1.7. Numerical experiments are performed to test the methods and to compare formulations in Section 1.8.

This chapter corresponds to the content of Zhou *et al.* [1][2].

1.2 Configuration

In this chapter, we are concerned with a 2D problem. The 3D problem is reduced to 2D by assuming an invariance along y in Cartesian coordinates or an azimuthal invariance along θ in cylindrical coordinates.

The problem is firstly treated in cylindrical coordinates. The propagation is performed in a 2D vertical plane with the coordinates system (r, z). The wave propagation is along the direction $+r$. The case in Cartesian coordinates will be introduced afterwards.

We work at a given frequency $f = \omega/2\pi$. The $\exp(j\omega t)$ time-dependence of the field is omitted. The field is assumed to be known at $r = r_0$. The propagation is computed in the region $r > r_0, z \geq 0$, as illustrated in Fig. G.1.

An inhomogeneous atmosphere is considered. The atmospheric characteristic is represented by the refractive index n. Because n is close to 1, it is convenient to use N, defined by

$$N = 10^6 \times (n - 1). \tag{1.1}$$

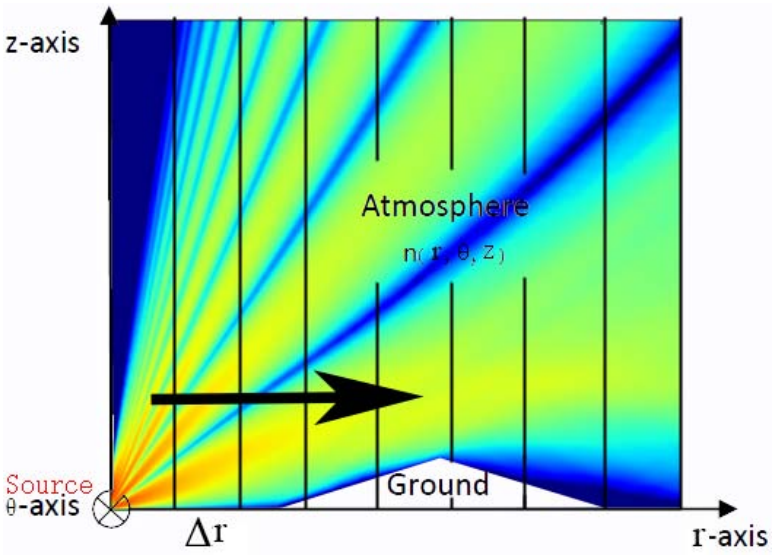

Figure 1.1: Split-step Fourier method.

The refractivity N can be expressed from the Smith-Weintraub equation [69]

$$N = \frac{77.6}{T}\left(P + 4810\frac{e}{T}\right), \tag{1.2}$$

with P the atmosphere pressure (hPa), e the water pressure (hPa), and T the absolute temperature (K). This expression may be used for radio frequencies up to 100 GHz with errors smaller than 0.5%.

To account for the Earth's curvature, an Earth flattening transform can also be applied. This can be done by replacing N by the modified refractivity M [70]. For various places on Earth, parametric descriptions of M exist [15]. They are often used as an input of the propagation model. These models and the modified refractivity are both introduced in Appendix A.

The configuration has been described. We will now introduce the continuous formulation of the split-step Fourier (SSF) method for simulating the wave propagation.

1.3 Continuous SSF over a PEC ground

In this section, the continuous SSF for the propagation over a perfect electric conductor (PEC) ground is presented. The solution is derived from continuous equations. This section is organized as follows.

First, the propagation equation is split into a forward and a backward equations. Only the forward-propagation is considered. Second, the PEC ground condition is introduced. Third, the continuous spectral transform is presented. Last, the split-step and phase-screens methods are detailed.

1.3.1 Equations for forward and backward propagations

In a medium with a refractive index $n(r, z)$, the electric field is solution of the 2D scalar Helmholtz equation

$$\nabla^2 \boldsymbol{E} + k_0^2 n^2 \boldsymbol{E} = 0, \tag{1.3}$$

with $\nabla^2 = \frac{\partial^2}{\partial r^2} + \frac{1}{r}\frac{\partial}{\partial r} + \frac{\partial^2}{\partial z^2}$ in cylindrical coordinates and $k_0 = \omega/c_0$ the vacuum wavenumber. The variation of n with r and z is omitted for a better readability.

The field can be decomposed in a transverse electric (TE) and a transverse magnetic (TM) components with respect to z. In 2D, for TE polarization, the electric field $\boldsymbol{E}$ only has a non-zero component E_θ. For TM polarization, the magnetic field $\boldsymbol{H}$ only has a non-zero component H_θ.

For the sake of simplicity, we define an appropriate variable representing the scalar field, denoted as Ψ. In this variable, the field decrease associated with cylindrical coordinates in $1/\sqrt{k_0 r}$ is removed. For TE polarization, the expression of Ψ is given by

$$\Psi(r, z) = \sqrt{k_0 r} E_\theta(r, z). \tag{1.4}$$

For TM polarization, we have

$$\Psi(r, z) = \sqrt{k_0 r} H_\theta(r, z). \tag{1.5}$$

For a wave mainly propagating along the $+r$ direction, a field u with reduced phase variation is given by

$$u(r, z) = e^{jk_0 r} \Psi(r, z). \tag{1.6}$$

This reduced field slowly varies in range.

Substituting (G.9) in (G.8) yields

$$\frac{\partial^2 u(r, z)}{\partial r^2} - 2jk_0 \frac{\partial u(r, z)}{\partial r} + \frac{\partial^2 u(r, z)}{\partial z^2} + k_0^2 (n^2 - 1) u(r, z) = -\frac{1}{4r^2} u(r, z). \tag{1.7}$$

Upon assuming r is greater than few wavelengths, the term $u(r, z)/4r^2$ is neglected.

Then (G.10) is factorized into two terms corresponding to forward and backward propagations

$$\left\{ \frac{\partial}{\partial r} - jk_0 (1 - \sqrt{1 + \mathcal{Z}}) \right\} \left\{ \frac{\partial}{\partial r} - jk_0 (1 + \sqrt{1 + \mathcal{Z}}) \right\} u(r, z) = 0, \tag{1.8}$$

with

$$\mathcal{Z} = \frac{1}{k_0^2} \frac{\partial^2}{\partial z^2} + n^2 - 1. \tag{1.9}$$

Note here that the calligraphic font is used for operators. Besides, the square-root symbol in (1.8) represents the composition of operators, i.e. it is such that

$$\sqrt{1 + \mathcal{Z}} \left(\sqrt{1 + \mathcal{Z}}(u) \right) = (1 + \mathcal{Z})(u). \tag{1.10}$$

Therefore, the forward-propagation wave fulfills

$$\frac{\partial u(r,z)}{\partial r} = jk_0(1-\sqrt{1+\mathcal{Z}})u(r,z), \tag{1.11}$$

whereas the backward-propagation wave fulfills

$$\frac{\partial u(r,z)}{\partial r} = jk_0(1+\sqrt{1+\mathcal{Z}})u(r,z). \tag{1.12}$$

In this method, only the forward-propagation is considered. Therefore, the field is assumed to satisfy (1.11).

The formulation would be similar in Cartesian coordinates where we would work with the coordinates (x,z). The scalar field would be defined by $\Psi = E_y(x,z)$ for TE and $\Psi = H_y(x,z)$ for TM. In addition, (G.10) is exact in Cartesian coordinates, no approximation is assumed. Thus, by replacing r by x, the proposed formulations are the same as in cylindrical coordinates.

1.3.2 PEC ground condition

A perfect electric conductor is an idealized material exhibiting infinite electric conductivity, i.e., zero resistivity. If a PEC planar ground is assumed at $z = 0$, the TE component fulfills the Dirichlet boundary condition

$$u\big|_{z=0} = 0. \tag{1.13}$$

The TM component fulfills the Neumann boundary condition

$$\left.\frac{\partial u}{\partial z}\right|_{z=0} = 0. \tag{1.14}$$

1.3.3 Spectral transform

The continuous spectral transform applied on the field u along z is denoted as $\mathcal{T}$, i.e.

$$\mathcal{T} : u(r,z) \longrightarrow U(r,k_z), \tag{1.15}$$

where k_z is the spectral variable in $[m]^{-1}$. The explicit form of the spectral transform $\mathcal{T}$ depends on the ground condition.

In the following sections, only the TE component is considered. The transforms for the TM component can be derived similarly.

If a PEC ground is assumed at $z = 0$, the spectral transform corresponds to a sine transform, denoted as $\mathcal{T}_\mathrm{s}$. It can be expressed as

$$U(r,k_z) = \mathcal{T}_\mathrm{s}u(r,z) = \sqrt{\frac{2}{\pi}}\int_0^{+\infty} u(r,z)\sin(k_z z)dz \qquad \forall r \geq 0. \tag{1.16}$$

The inverse spectral transform is given by

$$u(r,z) = \mathcal{T}_{\mathrm{s}}^{-1} U(r,k_z) = \sqrt{\frac{2}{\pi}} \int_0^{+\infty} U(r,k_z) \sin(k_z z) dk_z \qquad \forall r \geq 0. \tag{1.17}$$

For the TM component, the direct and inverse transforms would be cosine transforms, denoted as $\mathcal{T}_{\mathrm{c}}$ and $\mathcal{T}_{\mathrm{c}}^{-1}$.

1.3.4 Split-step method

The split-step method is applied on the forward-propagation equation (1.11). The main ideas are as follows:

- The wave propagation is computed iteratively in propagation distance.
- At each range step, the propagation and refraction terms are split and treated separately, so that:
  - The field is propagated through a slice of homogeneous medium. The propagation is computed in the spectral domain. The wave radiation and reflection over the boundary are modeled by this propagation term.
  - The refraction is modeled by a series of phase screens. This corresponds to a multiplication in the spatial domain.
  - Relief is considered in the spatial domain.

In the following, these algorithms are comprehensively introduced. First, the paraxial approximation is introduced to split the propagation and refraction terms. Second, the spectral representation and the phase-screens methods are presented.

1.3.4.a Splitting the propagation and refraction terms

A paraxial approximation is assumed to split the propagation and refraction terms. Several approximations can be applied. Then, the iterative solution in distance is derived.

- **Paraxial approximation**

  With a paraxial approximation, the calculation is only valid for propagation directions included in a paraxial cone centered along the r-direction, as illustrated in Fig. 1.2. Out of this cone, the error increases with the propagation angle.

  With this assumption, the second-order partial derivation of the field along z is assumed to be small, i.e., $\|\frac{\partial^2 u}{\partial z^2}\| \ll 1$. Moreover, the refractivity satisfies $n-1 \ll 1$. Hence, $\|\mathcal{Z}u\| \ll \|u\|$ in (1.8). This implies that the square-root operator $\sqrt{1+\mathcal{Z}}$ can be approximated.

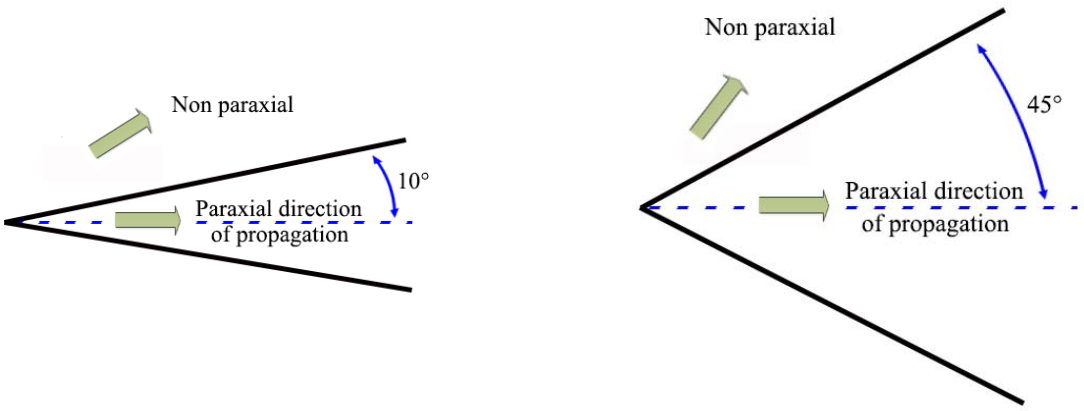

(a) Small-angle approximation (b) Wide-angle approximation

Figure 1.2: Paraxial approximation.

The most simple approximation is the first-order Taylor series, $\sqrt{1+\mathcal{Z}} \backsimeq 1+\mathcal{Z}/2$. It leads to the standard parabolic equation (SPE) valid for propagation limited to small angles ($< 10°$) around the paraxial direction [12], as illustrated in Fig. 1.2a.

A better approximation of the operator $\sqrt{1+\mathcal{Z}}$ corresponding to a wider propagation angle has been given by Feit and Fleck [71], as illustrated in Fig. 1.2b. They have applied a splitting operator computationally efficient and simple to incorporate in the split-step algorithm. It is given by

$$\sqrt{1+\mathcal{Z}} \simeq \sqrt{1+\mathcal{A}} + \sqrt{1+\mathcal{B}} - 1, \tag{1.18}$$

with

$$\mathcal{Z} = \mathcal{A} + \mathcal{B}, \quad \mathcal{A}u = \frac{1}{k_0^2}\frac{\partial^2 u}{\partial z^2}, \quad \mathcal{B}u = (n^2-1)u. \tag{1.19}$$

Note that (1.18) is exact in vacuum.

This formulation leads to a significant improvement in the accuracy of predictions based on the split-step algorithm. The propagation angle can be up to 45° [71].

After applying this approximation on (1.11), we have

$$\frac{\partial u(r,z)}{\partial r} = -jk_0(\sqrt{1+\mathcal{A}} - 1)u(r,z) - jk_0(n-1)u(r,z). \tag{1.20}$$

- **Propagation at increasing distances**

  The forward-propagation equation (1.20) is a differential equation of first-order in r. Thus, the propagation from r to $r+\Delta r$ is given by

$$u(r+\Delta r, z) = \exp\left(-\epsilon(\mathcal{C}+\mathcal{D})\right) u(r,z), \quad \Delta r > 0 \tag{1.21}$$

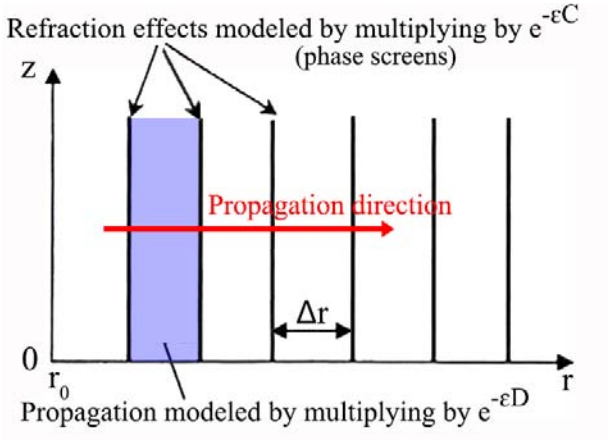

Figure 1.3: Split-step and phase-screens methods.

with $\epsilon = jk_0\Delta r$ and

$$\mathcal{C}u = (n-1)\,u, \quad \mathcal{D}u = \left(\sqrt{1+\mathcal{A}} - 1\right) u. \tag{1.22}$$

Our objective is to split the refraction term $\mathcal{C}$ and the propagation term $\mathcal{D}$, such that

$$e^{-\epsilon(\mathcal{C}+\mathcal{D})} = e^{-\epsilon\mathcal{C}} e^{-\epsilon\mathcal{D}}. \tag{1.23}$$

This split is not exact for an inhomogeneous medium. Nevertheless, the error is acceptable and the envelope of the error is given in [71].

Assuming (1.23), (1.21) becomes

$$u(r+\Delta r, z) = \exp(-\epsilon\mathcal{C})\left\{\exp(-\epsilon\mathcal{D})u(r,z)\right\}. \tag{1.24}$$

For each rang step, the propagation is computed as in a homogeneous medium, such that $n = 1$, by the operator $\exp(-\epsilon\mathcal{D})$ in the space domain. Then a phase screen is applied to consider the refractivity by means of the refraction operator $\mathcal{R}$, defined by

$$\mathcal{R} : u(r,z) \longrightarrow \exp(-\epsilon\mathcal{C})u(r,z), \tag{1.25}$$

where $\exp(-\epsilon\mathcal{C}) = \exp\left(-jk_0(n-1)\Delta r\right)$, which corresponds to a phase screen.

By splitting the propagation and the refraction terms, these parts are treated separately. In the next section, the propagation through a slice of homogeneous medium is treated in the spectral domain.

1.3.4.b Spectral propagation

The propagation term $\exp(-\epsilon\mathcal{D})$ is hard to compute in the spatial domain due to the second-order derivative in z. However, in the spectral domain, it is much easier, since derivatives in the spatial domain become multiplications in the spectral domain. In this

section, only the propagation term is treated, a homogeneous medium, such that $n = 1$, is thus considered here.

The spectral propagation term is computed by applying the spectral transform (1.16) to (1.20) with $n = 1$. This yields the spectral propagation equation in a homogeneous medium, given by

$$\left(\frac{\partial}{\partial r} + j\left(\sqrt{k_0^2 - k_z^2} - k_0\right)\right) U(r, k_z) = 0, \tag{1.26}$$

where $U(r, k_z)$ is the spectrum of $u(r, z)$ and $\mathrm{Im}\left(\sqrt{k_0^2 - k_z^2}\right) \leq 0$.

The solution of (1.26) for a propagation from r to $r + \Delta r$ is given by

$$U(r + \Delta r, k_z) = P_\mathrm{s}(k_z) U(r, k_z), \tag{1.27}$$

with

$$P_\mathrm{s}(k_z) = \exp\left(-j\Delta r\left(\sqrt{k_0^2 - k_z^2} - k_0\right)\right). \tag{1.28}$$

The propagation is realized by multiplying the field in the spectral domain by P_s. This latter is called the *spectral propagator*. The propagation operator in the spectral domain is denoted as $\mathcal{P}_\mathrm{s}$, defined by

$$\mathcal{P}_\mathrm{s} : U(r, k_z) \longrightarrow P_\mathrm{s}(k_z) U(r, k_z). \tag{1.29}$$

1.3.5 Propagation algorithm in a continuous domain

To conclude, the propagation over a PEC ground from r to $r + \Delta r$ can be simulated by

$$u(r + \Delta r, z) = \mathcal{R}\mathcal{T}_\mathrm{s}^{-1}\mathcal{P}_\mathrm{s}\mathcal{T}_\mathrm{s} u(r, z). \tag{1.30}$$

It is repeated at increasing distances to simulate the long-range propagation.

The continuous formulation of the split-step Fourier method has been presented. The propagation is simulated in the spectral domain and the refraction effects are modeled by applying phase screens in the spatial domain.

In numerical application, this method cannot be directly applied because a discretization is required. The discretization of the continuous formulation is detailed in the next section.

1.4 A-posteriori discretization of the continuous SSF over a PEC ground

For numerical reasons, the computation domain is discretized along r and z and of finite size. Consequences are twofold. First, an apodization is necessary to remove the reflection over the top boundary. Second, the continuous transform and propagator must be discretized.

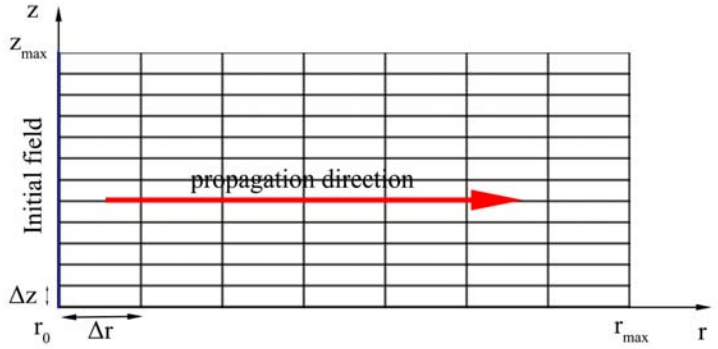

Figure 1.4: Discretization for the SSF.

1.4.1 Grid

The vertical domain is limited to $z \in [0, z_{\max}]$ and the propagation is simulated from r_0 to $r_{\max}$. A PEC ground condition is assumed at $z = 0$. The following uniform grid is used

$$\begin{aligned} r &= r_0 + p_r \Delta r \quad \text{for} \quad p_r = \{0, ..., N_r\}, \\ z &= p_z \Delta z \quad\;\; \text{for} \quad p_z = \{0, ..., N_z\}, \end{aligned} \tag{1.31}$$

with $\Delta r = (r_{\max} - r_0)/N_r$, and $\Delta z = z_{\max}/N_z$. This grid is shown in Fig. G.2. The field $u(r_{p_r}, p_z \Delta z)$, with $r_{p_r} = r_0 + p_r \Delta r$, is denoted by u_{p_r, p_z}.

1.4.2 Apodization

The vertical height is limited to $z_{\max}$. The top boundary must be perfectly transparent, letting all the energy coming from below the boundary propagate to infinity. There are many methods that could be used: an apodization layer, perfectly matched layers, or non-local boundary conditions [12].

In this work, an apodization is applied with a Hanning window on the top half of the spatial domain. For each iteration in range, i.e. in p_r, this amounts to a multiplication by a diagonal matrix $\mathbf{H}$, in which the diagonal elements are

$$\mathbf{H}_{p_z} = \begin{cases} 1 & \text{for } p_z \in [0, N_z/2], \\ \frac{1+\cos(\pi(\frac{2p_z\Delta z}{z_{\max}} - 1))}{2} & \text{for } p_z \in [N_z/2, N_z], \end{cases} \tag{1.32}$$

where a bold font is used for discrete operators, i.e. matrices.

As illustrated in Fig. 1.5a, the region with $p_z \in [0, N_z/2]$ is the computation domain of interest and the apodization is applied in the region with $p_z \in [N_z/2, N_z]$. The derivatives at $p_z = N_z/2$ and $p_z = N_z$ are zero, which ensures a smooth transition between both domains.

The Hanning window works very well for paraxial propagation (attenuation of at least 100 dB for propagation angles smaller than 2.75° [12]). However, for large propagation angles, the error increases. Other windows are possible for the absorbing layers as described in the literature [12].

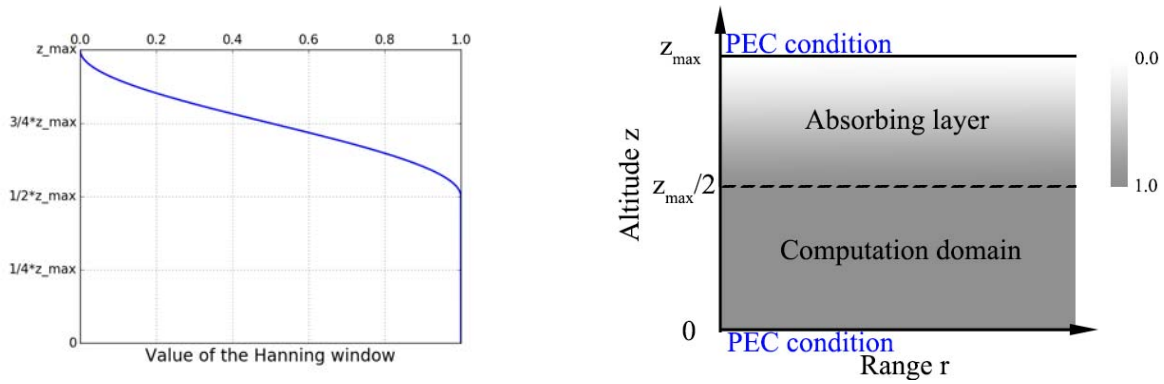

(a) Hanning window (b) Apodization

Figure 1.5: Domain truncation.

After applying the apodization, as no field reaches the top boundary, any boundary condition can be applied on the top of the apodization area at $z = z_{\max}$. Here, the top boundary is assumed the same as the ground condition, as illustrated in Fig. 1.5b.

Since PEC condition is assumed at $z = 0$ and $z = z_{\max}$, the propagation is regarded as in a waveguide. Hence, $u_{p_r,0} = 0$ and $u_{p_r,N_z} = 0$. For the propagation, only the field u_{p_r,p_z} with $p_z = \{1, ..., N_z - 1\}$ has to be considered.

1.4.3 Irregular relief modeling

An irregular relief can be considered by different models. The simplest solution is modeling the relief slopes by staircases, which is detailed in Appendix B. The operator modeling the relief in the spatial domain is denoted as $\mathbf{L}$.

1.4.4 Discretization of the continuous spectral transform

Since the vertical domain is of finite height and discretized by (1.31), the continuous spectral transforms (1.16) and (1.17) are discretized and of finite size.

Since a PEC condition is assumed at the boundaries, the spectral transform corresponds to a discrete sine transform (DST). It is denoted as $U_{p_r,\bullet} = \mathbf{T}_{\mathrm{s}} u_{p_r,\bullet}$, which satisfies

$$U_{p_r,q_z} = \frac{1}{\sqrt{2(N_z+1)}} \sum_{p_z=1}^{N_z-1} u_{p_r,p_z} \sin\left(\pi \frac{p_z q_z}{N_z}\right), \tag{1.33}$$

with $q_z \in [1, N_z - 1]$.

The inverse spectral transform is the inverse discrete sine transform (IDST), denoted as

$u_{p_r,\bullet} = \mathbf{T_s}^{-1} U_{p_r,\bullet}$. It satisfies

$$u_{p_r,p_z} = \frac{1}{\sqrt{2(N_z+1)}} \sum_{q_z=1}^{N_z-1} U_{p_r,q_z} \sin\left(\pi \frac{p_z q_z}{N_z}\right). \tag{1.34}$$

1.4.5 Discretization of the continuous propagator

A limitation of the vertical computation domain and a discretization on z are applied on the continuous spatial equations in Section G.1.5. The propagator (1.29) is discretized and of a finite size, denoted here as $\mathbf{P_s}$. Notice here, $\mathbf{P_s}$ corresponds to a diagonal matrix. The propagated spectrum is denoted with an upperscript 'p', which satisfies $U^{\mathrm{p}}_{p_r+1,\bullet} = \mathbf{P_s} U_{p_r,\bullet}$. Thus, we have

$$U^{\mathrm{p}}_{p_r+1,q_z} = P_{\mathrm{s}}(k_z) U_{p_r,q_z}, \tag{1.35}$$

with $P_{\mathrm{s}}(k_z)$ are the diagonal elements of $\mathbf{P_s}$, expressed by

$$P_{\mathrm{s}}(k_z) = \exp\left[-j\Delta r \left(\sqrt{k_0^2 - k_z^2} - k_0\right)\right], \tag{1.36}$$

where $\mathrm{Im}\left(\sqrt{k_0^2 - k_z^2}\right) \leq 0$ and the discretized spectral variable k_z is

$$k_z = q_z \Delta k_z, \tag{1.37}$$

with $q_z = \{1, \ldots, N_z - 1\}$ and

$$\Delta k_z = \pi / z_{\max}. \tag{1.38}$$

1.4.6 Algorithm from the a-posteriori discretization: the SSF-ST

The propagation from r_{p_r} to r_{p_r+1} is simulated by

$$u_{p_r+1,\bullet} = \mathbf{HRLT_s}^{-1} \mathbf{P_s} \mathbf{T_s} u_{p_r,\bullet}, \tag{1.39}$$

with $\mathbf{R}$ corresponding to the refraction operator $\mathcal{R}$ discretized at $z = p_z \Delta z$. The computation is performed marching on in distance to reach $r_{\max}$. We remind that $\mathbf{T_s}$ and $\mathbf{T_s}^{-1}$ are the spectral transform and its inverse. $\mathbf{P_s}$ is the spectral propagator. $\mathbf{L}$ accounts for the relief and $\mathbf{H}$ for the apodization.

In this algorithm, the discretization is applied *a posteriori* from the continuous formulation. This method for the propagation over a PEC ground is denoted as SSF-ST. In the following section, we propose a discrete formulation of SSF, where the discretization is applied *a priori*: the calculations start from the discrete propagation equation.

1.5 Self-consistent discrete formulation of the SSF over a PEC ground

In this section, a discrete formulation of SSF for a PEC planar ground is proposed, denoted as DSSF-DST. The discretization along z is performed *a priori* on the Helmholtz equation. The spectral transform and the propagator are derived entirely in the discrete domain, where the grid defined in Section G.1.3 is used.

1.5.1 Discrete equations

In the discrete domain, the differential operator along z in (G.10) is approximated by finite-differences [65]. The continuous derivative along r is kept and solved afterwards. The discrete counterpart of the Helmholtz equation applied to the reduced field is

$$\frac{\partial^2 u_{r,p_z}}{\partial r^2} - 2jk_0\frac{\partial u_{r,p_z}}{\partial r} + \mathbf{d}_z^2 u_{r,p_z} + k_0^2(n_{r,p_z}^2 - 1)u_{r,p_z} = 0, \tag{1.40}$$

where $u_{r,p_z} = u(r, p_z\Delta z)$ and $n_{r,p_z} = n(r, p_z\Delta z)$. The term $\mathbf{d}_z^2$ is the second-order central-difference approximation given by

$$\mathbf{d}_z^2 u_{r,p_z} = \frac{1}{\Delta z^2}(u_{r,p_z+1} - 2u_{r,p_z} + u_{r,p_z-1}). \tag{1.41}$$

Only the forward propagation is considered. The paraxial approximation is applied as introduced in the continuous formulation (see Section 1.3.4).

The discrete forward propagation equation is given by

$$\frac{\partial u_{r,p_z}}{\partial r} = -j(\sqrt{k_0 + \mathbf{d}_z^2} - k_0)u_{r,p_z} - jk_0(n-1)u_{r,p_z}. \tag{1.42}$$

The solution of (1.42), which represents the propagation from r_{p_r} to r_{p_r+1}, can be expressed as

$$u_{p_r+1,\boldsymbol{\cdot}} = \mathbf{R}\mathbf{D}u_{p_r,\boldsymbol{\cdot}}, \tag{1.43}$$

where $\mathbf{D} = \exp\left(-\epsilon(\sqrt{1 + \mathbf{d}_z^2/k_0^2} - 1)\right)$, $\epsilon = jk_0\Delta r$, and $\mathbf{R}$ is as in (1.39).

1.5.2 Spectral transforms

The objective is to derive the spectral propagator associated with the discrete formulation by means of the diagonalization of $\mathbf{d}_z^2$ with Dirichlet boundaries.

The diagonalization of $\mathbf{d}_z^2$ is obtained by calculating

$$\begin{aligned}\mathbf{d}_z^2\left(\sin\left(\pi\frac{p_z q_z}{N_z}\right)\right) &= \frac{1}{\Delta z^2}\left(\sin\left(\pi\frac{(p_z-1)q_z}{N_z}\right) - 2\sin\left(\pi\frac{p_z q_z}{N_z}\right) + \sin\left(\pi\frac{(p_z+1)q_z}{N_z}\right)\right)\\ &= -(k_z^{\mathrm{d}})^2\sin\left(\pi\frac{p_z q_z}{N_z}\right),\end{aligned} \tag{1.44}$$

where

$$k_z^{\mathrm{d}} = \frac{2}{\Delta z} \sin\left(\frac{\pi q_z}{2N_z}\right), \tag{1.45}$$

with $q_z = \{1, \ldots, N_z - 1\}$.

Thus, for the operator $\mathbf{d}_z^2$, the eigenvalues are $-(k_z^{\mathrm{d}})^2$ with the eigenvectors $\sin\left(\pi \frac{p_z q_z}{N_z}\right)$ [72]. DST is still the transform to be used and the spectral propagation equation in a homogeneous atmosphere is

$$\frac{\partial^2 U_{r,q_z}}{\partial r^2} - 2jk_0 \frac{\partial U_{r,q_z}}{\partial r} - (k_z^{\mathrm{d}})^2 U_{r,q_z} = 0, \tag{1.46}$$

with $U_{r,q_z} = U(r, q_z \Delta k_z)$. Following the same method to split forward and backward propagations as in Section 1.3.1, the spectral forward propagation equation is given by

$$\left(\frac{\partial}{\partial r} + j\left(k_r^{\mathrm{d}} - k\right)\right) U_{r,q_z} = 0, \tag{1.47}$$

with $k_r^{\mathrm{d}} = \sqrt{k_0^2 - (k_z^{\mathrm{d}})^2}$. The propagated spectrum $U_{p_r+1,q_z}^{\mathrm{p}}$ is given by

$$U_{p_r+1,q_z}^{\mathrm{p}} = P_{\mathrm{s}}^{\mathrm{d}}[q_z] U_{p_r,q_z}, \tag{1.48}$$

with $U_{p_r,q_z} = U(r_{p_r}, q_z \Delta k_z)$. The propagator is given by

$$P_{\mathrm{s}}^{\mathrm{d}}[q_z] = \exp\left\{-j\Delta r \left(\sqrt{k_0^2 - (k_z^{\mathrm{d}})^2} - k_0\right)\right\}, \tag{1.49}$$

where $\mathrm{Im}\left(\sqrt{k_0^2 - (k_z^{\mathrm{d}})^2}\right) \leq 0$ and the corresponding propagation diagonal operator is denoted as $\mathbf{P}_{\mathrm{s}}^{\mathrm{d}}$.

The propagator has the same expression as in Section 1.4.5 except for the expression of k_z, which is replaced by k_z^{d}. When $q_z \ll N_z$, i.e. for the first modes, they are almost equal. When the order increases, differences appear.

1.5.3 Self-consistent algorithm: the DSSF-DST

The propagation from r_{p_r} to r_{p_r+1} is simulated by

$$u_{p_r+1,\cdot} = \mathbf{HRLT}_{\mathrm{s}}{}^{-1} \mathbf{P}_{\mathrm{s}}^{\mathrm{d}} \mathbf{T}_{\mathrm{s}} u_{p_r,\cdot}. \tag{1.50}$$

The computation is performed marching on in distance. Compared to SSF-ST in (1.39), the only difference is the propagation operator $\mathbf{P}_{\mathrm{s}}$, which is replaced by $\mathbf{P}_{\mathrm{s}}^{\mathrm{d}}$.

1.6 Synthesis of the methods over a PEC ground

The methods for the propagation over a PEC ground have now been completely presented. A synthesis can be made. The formulation has firstly been established from the continuous

	Discretization	Spectral transform	Propagator
SSF-ST	*a-posteriori*	DST	Discretized from continuous formulation
DSSF-DST	*a-priori*	DST	Discrete formulation

Table 1.1: Comparison of the different methods for propagation over a PEC ground.

equation. Then, two numerical schemes have been obtained, as shown in Table 1.1. First, SSF-ST has been derived in the continuous domain. The discretization is performed *a posteriori*. Second, DSSF-DST has been derived directly from the discrete equations. Hence, it is self-consistent in the discrete domain. Only the propagators are different in SSF-ST and DSSF-DST.

In the next section, the propagation methods over an impedance ground are formulated.

1.7 Propagation over an impedance ground

In a realistic environment, a perfectly conducting ground may not be adequate. A dielectric ground condition is generally more realistic. According to Leontovich [73], this can be approximated by an impedance ground for a plane wave illumination.

In this section, propagation methods over an impedance ground are presented. First, a continuous formulation is presented. This method is discretized for numerical application. Then, a self-consistent discrete method is proposed. Last, an inconsistency in the widely-used method SSF-DMFT is highlighted.

1.7.1 Continuous SSF over an impedance ground

The continuous SSF using the mixed Fourier transform [23] is the first approach that has been proposed to simulate the propagation over an impedance ground. Firstly, the continuous impedance boundary condition is introduced. Secondly, the corresponding spectral transform is described. Thirdly, the spectral propagators are derived. Finally, the propagation scheme is exposed.

1.7.1.a Continuous impedance boundary condition

Considering the propagation of a plane wave, a dielectric ground can be approximated by an impedance ground. The continuous impedance ground condition is given by [73]

$$\boldsymbol{n} \times \boldsymbol{E} = \zeta \, \boldsymbol{n} \times \boldsymbol{n} \times \boldsymbol{H}. \tag{1.51}$$

with $\boldsymbol{n}$ is the outgoing normal vector. The quantity $\zeta \in \mathbb{C}$ is the surface impedance in $[\Omega]$. From (1.51), the local boundary condition on u is given by

$$\left.\frac{\partial u(r,z)}{\partial z}\right|_{z=0} + \alpha u(r,0) = 0, \tag{1.52}$$

where

$$\alpha = jk_0 \cos\theta_i \left[\frac{1-\Gamma}{1+\Gamma}\right], \tag{1.53}$$

with θ_i the plane wave angle of incidence, i.e. measured from the surface normal, and Γ is the reflection coefficient. More information about the impedance boundary condition can be found in Appendix C.

A method to model surface roughness is given in [74]. The idea is to modify the smooth-surface reflection coefficient to account for the reduction of the specular reflection due to roughness.

1.7.1.b Mixed Fourier transform

Considering an impedance ground, the mixed Fourier transform (MFT) [23] is used to incorporate a surface impedance with PE. The corresponding spectral transform $\mathcal{T}_\mathrm{m}$ is defined by

$$U(r,k_z) = \mathcal{T}_\mathrm{m} u(r,z) = \int_0^{+\infty} u(r,z)[\alpha \sin(k_z z) - k_z \cos(k_z z)]dz. \tag{1.54}$$

The inverse transform is given by

$$u(r,z) = {\mathcal{T}_\mathrm{m}}^{-1} U(r,k_z) = K(r)e^{-\alpha z} + \int_0^{+\infty} U(p,z)\frac{\alpha \sin(k_z z) - k_z \cos(k_z z)}{\alpha^2 + k_z^2}dk_z, \tag{1.55}$$

where k_z is the spectral variable. In TE polarization, $Re(\alpha) < 0$ and there is no surface wave. This yields

$$K(r) = 0. \tag{1.56}$$

On the other hand, in TM polarization, $Re(\alpha) > 0$. There is a non-zero homogeneous solution that must be added. It is given by

$$K(r) = 2\alpha \int_0^{+\infty} u(r,z)e^{-\alpha z}. \tag{1.57}$$

This corresponds to a surface wave.

1.7.1.c Spectral propagators

According to [23], the propagator applied on $U(r,k_z)$ is the same as in Section 1.3.4.b, i.e.

$$P_\mathrm{m}(k_z) = \exp\left(-j\Delta r\left(\sqrt{k_0^2 - k_z^2} - k_0\right)\right), \tag{1.58}$$

with $\mathrm{Im}\left(\sqrt{k_0^2 - k_z^2}\right) \leq 0$. The wave-surface propagator P_m^sw satisfies

$$K(r + \Delta r) = P_\mathrm{m}^\mathrm{sw} K(r), \tag{1.59}$$

with

$$P_{\mathrm{m}}^{\mathrm{sw}} = \exp\left(-j\Delta r\left(\sqrt{k_0^2+\alpha^2}-k_0\right)\right). \tag{1.60}$$

The diagonal propagation operator $\mathcal{P}_{\mathrm{m}}$ amounts to multiply term-by-term the propagators $P_{\mathrm{m}}(k_z)$ and $P_{\mathrm{m}}^{\mathrm{sw}}$ to the space wave $U(r,k_z)$ and the surface wave $K(r)$, respectively.

The propagators are here derived with the approximation given by Feit and Fleck [71] as in (1.18). The expressions here are different from the propagators given in [23], which are based on the small angle approximation.

1.7.1.d Propagation algorithm in a continuous domain

The propagation over an impedance ground from r to $r+\Delta r$ is simulated as

$$u(r+\Delta r,\bullet) = \mathcal{R}{\mathcal{T}_{\mathrm{m}}}^{-1}\mathcal{P}_{\mathrm{m}}\mathcal{T}_{\mathrm{m}}u(r,\bullet). \tag{1.61}$$

This method has the capacity of considering an impedance ground. However, in numerical application, this method cannot be directly applied and an *a-posteriori* discretization is needed.

1.7.2 A-posteriori discretization of the continuous method using MFT

For numerical implementation, the continuous method using MFT is discretized *a posteriori* on the same discrete grid as in Section G.1.3. This discretized method is denoted as SSF-MFT. Both the continuous spectral transform and propagators are discretized in this subsection.

1.7.2.a Discretization of the continuous spectral transform

The spectral transforms in Section 1.7.1.b is discretized on $p_z\Delta z$ with $p_z \in \{0, N_z\}$. The discretized MFT is given by

$$U_{p_x,q_z} = {\sum_{p_z=0}^{N}}' u_{p_x,p_z}\left[\alpha\sin\left(\pi\frac{p_zq_z}{N_z}\right) - q_z\Delta k_z\cos\left(\pi\frac{p_zq_z}{N_z}\right)\right], \tag{1.62}$$

where $q_z \in \{0,\dots,N_z\}$. The prime on the sum means that the first and last values have to be weighted with a factor $1/2$. The discretized inverse MFT is given by

$$u_{p_x,p_z} = K_{\mathrm{d}}e^{-\alpha p_z\Delta z} + {\sum_{q_z=0}^{N}}' U_{p_x,q_z}\frac{\alpha\sin\left(\pi\frac{p_zq_z}{N_z}\right) - q_z\Delta k_z\cos\left(\pi\frac{p_zq_z}{N_z}\right)}{\alpha^2+(q_z\Delta k_z)^2}, \tag{1.63}$$

where in TE polarization, $K_{\mathrm{d}} = 0$ and in TM polarization,

$$K_{\mathrm{d}} = 2\alpha{\sum_{p_z=0}^{N}}' e^{-\alpha p_z\Delta z}u_{p_x,p_z}. \tag{1.64}$$

1.7.2.b Discretization of the continuous propagator

The discretized form of the continuous propagator is the same as in Section 1.4.5. The propagator is discretized as

$$P_{\mathrm{m}}(k_z) = \exp\left[-j\Delta r\left(\sqrt{k_0^2 - k_z^2} - k_0\right)\right], \tag{1.65}$$

with $\mathrm{Im}\left(\sqrt{k_0^2 - k_z^2}\right) \leq 0$. The spectral variable is

$$k_z = q_z \Delta k_z, \tag{1.66}$$

where $q_z = \{1, \ldots, N_z - 1\}$ and $\Delta k_z = \pi / z_{\max}$.

The propagator for the surface wave component K_{d} is as in (1.60).

The discretized method of the continuous formulation, SSF-MFT, has been presented. It is known that this method could lead to numerical instabilities in certain conditions [75]. In the next section, a self-consistent discrete method is described.

1.7.3 Self-consistent discrete method for the propagation over an impedance ground

The objective in this subsection is to develop a self-consistent method in the discrete domain for the propagation over an impedance ground. The discretization is performed *a priori*. The formulation is based on the discrete impedance boundary condition and propagation equation to achieve self-consistency [65]. This method is called DSSF-DMFT.

The same discrete grid is used as in Section G.1.3. Here, $u_{p_r,0}$ and u_{p_r,N_z} represent the surfaces waves at the boundaries. Thus, the field u_{p_r,p_z} with $p_z = \{0, \ldots, N_z\}$ is considered in this section.

1.7.3.a Discrete impedance boundary condition

In the discrete formulation, the differential operator in (1.52) is approximated by finite-differences. Thus, the discrete impedance boundary condition at ground $z = 0$ is

$$\mathbf{d}_z(u_{p_r,p_z})|_{p_z=0} + \alpha u_{p_r,0} = 0, \tag{1.67}$$

with $\mathbf{d}_z$ the centered first order finite-difference approximation of step $2\Delta z$. The same boundary condition is assumed at $z = z_{\max}$.

1.7.3.b Discrete mixed Fourier transform

The discrete mixed Fourier transform (DMFT) [32] is the spectral transform adapted to the discrete impedance boundary condition (1.67). The discretization is performed *a priori*.

To alleviate the computation load, the discrete impedance boundary condition can be replaced by a Dirichlet condition with a variable substitution from u to w, such that

$$w_{p_r,p_z} = \frac{u_{p_r,p_z+1} - u_{p_r,p_z-1}}{2\Delta z} + \alpha u_{p_r,p_z}, \tag{1.68}$$

with $p_z = \{1, \ldots, N_z - 1\}$ and $w_{p_r,p_z} = w(r_{p_r}, p_z\Delta z)$.

Thus, the impedance condition at the boundaries becomes

$$\begin{aligned} w_{p_r,0} &= 0, \\ w_{p_r,N_z} &= 0. \end{aligned} \tag{1.69}$$

Therefore, w is propagated over Dirichlet boundaries. In this way, the combination of sine and cosine transforms on u is replaced by a sine transform on w [32]. The computation load is reduced by 2.

After applying DMFT, the spectrum W is obtained. The spectrum W_{p_r,q_z} with $q_z \in [1, N_z - 1]$ corresponds to the space wave, whereas $W_{p_r,0}$ and W_{p_r,N_z} correspond to the surface waves associated with each boundary.

The operators corresponding to DMFT and its inverse transform are denoted as $\mathbf{T}_\mathrm{m}$ and $\mathbf{T}_\mathrm{m}^{-\mathbf{1}}$. The details of these transforms can be found in Appendix D.

1.7.3.c Spectral propagator of DSSF-DMFT

The propagation of W_{p_r,q_z} with $q_z = \{0, \ldots, N_z\}$ for Δr is given by

$$W^\mathrm{p}_{p_r+1,q_z} = P^\mathrm{d}_\mathrm{m}[q_z] W_{p_r,q_z}, \tag{1.70}$$

where $P^\mathrm{d}_\mathrm{m}[q_z]$, with $q_z = \{1, \ldots, N_z - 1\}$, represents the propagators of the space waves. Furthermore, $P^\mathrm{d}_\mathrm{m}[0]$ and $P^\mathrm{d}_\mathrm{m}[N_z]$ represent the propagators of the surface waves. The corresponding propagation operator is $\mathbf{P}^\mathrm{d}_\mathrm{m}$, satisfying $W^\mathrm{p}_{p_r+1,\boldsymbol{\cdot}} = \mathbf{P}^\mathrm{d}_\mathrm{m} W_{p_r,\boldsymbol{\cdot}}$.

The propagators are developed as follows:

- Space waves:

  For the space wave, since w satisfies the Dirichlet ground condition at the boundaries, the propagator $P^\mathrm{d}_\mathrm{m}[q_z]$ for w with $q_z = \{1, \ldots, N_z - 1\}$ is the same as the one for u of DSSF-DST given in Section 1.5.2. It is given by

  $$P^\mathrm{d}_\mathrm{m}[q_z] = \exp\left(-j\Delta r \left(\sqrt{k_0^2 - (k_z^\mathrm{d})^2} - k_0\right)\right), \tag{1.71}$$

  with $\mathrm{Im}\left(\sqrt{k_0^2 - (k_z^\mathrm{d})^2}\right) \leq 0$ and

  $$k_z^\mathrm{d} = \frac{2}{\Delta z} \sin\left(\frac{\pi q_z}{2N_z}\right). \tag{1.72}$$

- Surface waves:

  The surface wave terms $W_{p_r,0}\gamma^{p_z}$ and $W_{p_r,N_z}(-1/\gamma)^{p_z}$ satisfy the discrete propagation equation

$$\frac{\partial^2 u}{\partial r^2} - 2jk_0\frac{\partial u}{\partial r} + \mathbf{d}_z^2 u = 0, \tag{1.73}$$

  with $\mathbf{d}_z^2$ defined in (G.12). The detailed formulation can be found in Appendix D. Therefore, the propagators corresponding to the forward propagating surface waves are

$$\begin{aligned} P_{\mathrm{m}}^{\mathrm{d}}[0] &= \exp\left\{-j\Delta x\left(\sqrt{k_0^2 + \tfrac{\gamma+\gamma^{-1}-2}{\Delta z^2}} - k_0\right)\right\}, \\ P_{\mathrm{m}}^{\mathrm{d}}[N_z] &= \exp\left\{-j\Delta x\left(\sqrt{k_0^2 + \tfrac{(-\gamma)+(-\gamma)^{-1}-2}{\Delta z^2}} - k_0\right)\right\}. \end{aligned} \tag{1.74}$$

1.7.3.d Synthesis of the algorithm

To simulate the propagation, the computation is performed marching on in distance. At each iteration from r_{p_r} to r_{p_r+1}, the propagation, the refractivity, the apodization, and the relief are considered using the steps as described below:

$$u_{p_r+1,\bullet} = \mathbf{HRLT}_{\mathrm{m}}{}^{-1}\mathbf{P}_{\mathrm{m}}^{\mathrm{d}}\mathbf{T}_{\mathrm{m}}u_{p_r,\bullet}, \tag{1.75}$$

with $\mathbf{P}_{\mathrm{m}}^{\mathrm{d}}$ the propagation operator for space and surface waves, $\mathbf{L}$ the operator modeling the irregular relief, $\mathbf{R}$ the refraction operator, and $\mathbf{H}$ the apodization operator. The operators $\mathbf{L}$, $\mathbf{R}$, and $\mathbf{H}$ are the same as in (1.39).

1.7.4 Inconsistent formulation: SSF-DMFT

For simulating the propagation over an impedance ground, the discrete method proposed by Dockery *et al.* [32] is widely used. This method is denoted as SSF-DMFT. An inconsistency between the spectral transform and the propagator is here pointed out.

1.7.4.a Spectral transform

In SSF-DMFT, the spectral transform is the DMFT, introduced in Section 1.7.3.b, which is based on the discrete impedance boundary condition (1.67).

1.7.4.b Spectral propagators

Although the spectral transform is based on the discrete boundary condition, the spectral propagators are based on the continuous propagation equation (G.10). Indeed, their values are as follows:

- Space waves:

  The propagator $P_{\mathrm{m}}[q_z]$ with $q_z = \{1, \ldots, N_z - 1\}$ is the one given in Section 1.4.5.

- Surface waves:

  According to SSF-DMFT [32], $W_{p_r,0}\gamma^{z/\Delta z}$ and $W_{p_r,N_z}(-1/\gamma)^{z/\Delta z}$ satisfy the continuous propagation equation

  $$\frac{\partial^2 u}{\partial r^2} - 2jk_0\frac{\partial u}{\partial r} + \frac{\partial^2 u}{\partial z^2} = 0, \tag{1.76}$$

  with k_0 is the wavenumber in the impedance boundaries and γ is a parameter defined in DMFT, which is detailed in Appendix D.

  The propagators of the forward propagating surface waves are:

  $$\begin{aligned} P_{\mathrm{m}}[0] &= \exp\left\{-\tfrac{j\Delta x}{2k_0\Delta z^2}\left(\ln\gamma\right)^2\right\}, \\ P_{\mathrm{m}}[N_z] &= \exp\left\{-\tfrac{j\Delta x}{2k_0\Delta z^2}\left(\ln(-\gamma)\right)^2\right\}. \end{aligned} \tag{1.77}$$

The correspond propagation operator is denoted as $\mathbf{P}_{\mathrm{m}}$.

1.7.4.c Synthesis of the algorithm

The propagation from r_{p_r} to r_{p_r+1} is computed by

$$u_{p_r+1,\boldsymbol{.}} = \mathbf{HRLT}_{\mathrm{m}}{}^{-1}\mathbf{P}_{\mathrm{m}}\mathbf{T}_{\mathrm{m}}u_{p_r,\boldsymbol{.}}. \tag{1.78}$$

The only difference between the SSF-DMFT and DSSF-DMFT is that $\mathbf{P}_{\mathrm{m}}^{\mathrm{d}}$ in (1.75) is here replaced by $\mathbf{P}_{\mathrm{m}}$.

1.7.4.d Inconsistency

In SSF-DMFT, the spectral transforms $\mathbf{T}_{\mathrm{m}}$ and $\mathbf{T}_{\mathrm{m}}{}^{-1}$ are derived form the discrete boundary condition. However, the spectral propagator $\mathbf{P}_{\mathrm{m}}$ is based on the continuous equation. This is an inconsistency in this method.

1.7.5 Synthesis of the methods with an impedance ground

The methods for modeling the propagation over an impedance ground are shown in Table 1.2. In this table, the spectral transform and the propagator are derived either from the continuous equation (G.10) or the discrete equation (G.11).

First, in SSF-MFT (see Section 1.7.1.b), the transform and the propagator are both derived from the continuous equations. Then, for numerical applications, the discretization

	Spectral transform	Propagator	Consistency	Discretization
SSF-MFT	continuous:MFT	continuous	consistent	*a posteriori*
SSF-DMFT	discrete:DMFT	continuous	inconsistent	*a priori*/*a posteriori*
DSSF-DMFT	discrete:DMFT	discrete	consistent	*a priori*

Table 1.2: Different methods for propagation over an impedance ground.

is applied *a posteriori*. This causes some numerical problems. Certain combinations of parameters can occasionally cause numerical instabilities [75].

Second, in SSF-DMFT, the spectral transform is DMFT, derived from the discrete equation, while the propagator is derived from the continuous equation. This is an inconsistency.

In our proposed DSSF-DMFT method, both the spectral transform and the propagator are derived from the discrete equation. According to the discrete electromagnetic theory [65], it achieves self-consistency in the discrete domain.

1.8 Numerical experiments

In this section, several tests are performed to test the continuous and discrete formulations for propagation without ground reflection and for propagation over impedance grounds. In addition, a test for a long-range propagation in a complex environment is also performed.

The simulations are performed on a desktop computer with a CPU frequency of 1.60 GHz and a memory of 32 Gb. The programming language is *Python*.

1.8.1 Comparison of the propagators of SSF and DSSF

In the first step, numerical tests are performed to compare the propagators of SSF and DSSF as defined in Sections 1.4.5 and 1.5.2.

The frequency is 300 MHz. The parameters of the simulation are $\Delta r = 1$ m, $z_{\max} = 30$ m, and $\Delta z = 0.2$ m.

The propagator values are shown in Fig. 1.6. For clarity purpose, we only show 30 out of 100 propagator values of (1.28) with the continuous and discrete formulations. In Fig. 1.6a, the values located on the circle of radius 1.0 correspond to the propagative modes, whereas the other ones correspond to the evanescent modes. Explicitly, the propagative modes correspond to a real k_r, whereas for evanescent modes k_r is a pure negative imaginary number.

The norm and phase of the propagators are shown in Fig 1.6b and 1.6c. We notice that, for the propagative modes of small order (approximately smaller than 20), the propagators of SSF and DSSF are very close. Differences become greater as the order increases.

Moreover, if we choose Δz smaller, the difference between the 2 propagators becomes smaller. Indeed, in DSSF, we apply the finite-difference approximation to the propagation equation. This approximation is closer to the exact expression when Δz is chosen small.

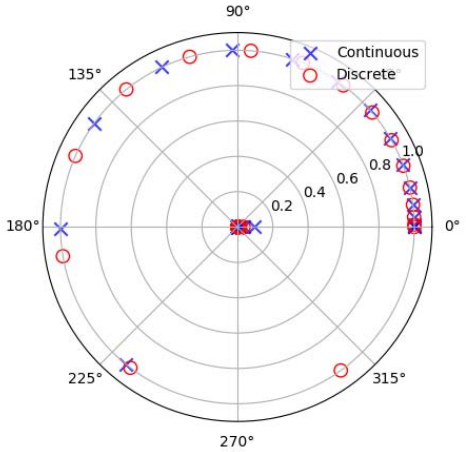

(a) Propagators in the complex plane

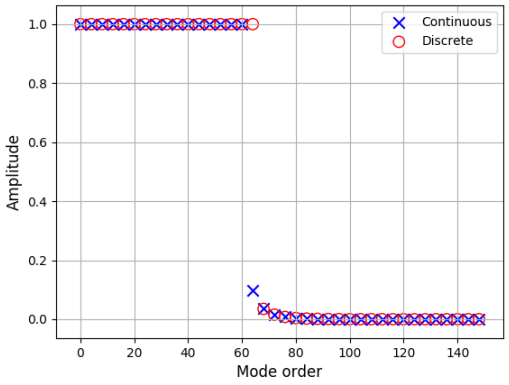

(b) Magnitude of the propagators

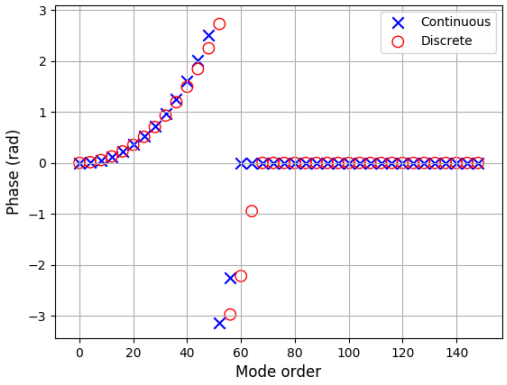

(c) Phase of the propagators

Figure 1.6: Values of the propagators of SSF (contiuous) and DSSF (discrete) with $\Delta z = 0.2\lambda$.

1.8.2 Propagation without reflection over the ground

In this section, we compare the electromagnetic wave propagation without reflection over the ground with SSF and DSSF.

1.8.2.a Complex source point

A complex source point (CSP) [76] is used as the source of the wave. The source is localized at a complex position $(x_\mathrm{s}, y_\mathrm{s}, z_\mathrm{s})$ with $x_\mathrm{s} \in \mathbf{C}$ such that $x_\mathrm{s} = x_{w0} - jkW_0^2/2$, $y_\mathrm{s} = 0$, and $z_\mathrm{s} = 0$. Its radiation can be obtained analytically by means of the 2D/3D Green's function. Its expression in 2D is given by

$$G_\mathrm{2D}(\tilde{r}) = \frac{j}{4} H_0^{(2)}(k_0 \tilde{r}), \tag{1.79}$$

and the expression in 3D is

$$G_{3D}(\tilde{r}) = -\frac{\exp(-jk_0\tilde{r})}{4\pi\tilde{r}}, \tag{1.80}$$

with $\tilde{r}$ is the distance between the point of observation and the source point, defined as

$$\tilde{r} = \sqrt{(x-x_s)^2 + (y-y_s)^2 + (z-z_s)^2}. \tag{1.81}$$

A complex source point excites a collimated beam. This beam can be approximated by a Gaussian beam for $kW_0 > 5$. In free space, the simulation results of SSF and DSSF are compared to the analytic solution of the CSP.

The parameters of the CSP are: frequency $f = 300$ MHz, $z_s = 1000$ m, $x_{w0} = -50$ m, and $W_0 = 3$ m (3λ). The height z_s is chosen high for the wave not to reach the ground.

The parameters of the simulation are as follows: r_{max} is 2000 m, Δr is 100 m, and z_{max} is 4000 m.

First, we make a test with $\Delta z = 0.5$ m (0.5λ). The propagation of the CSP is shown in Fig. 1.7a. The radiation of the CSP in free space is very close to a Gaussian beam. The final normalized fields are shown in Fig. 1.7b. Both SSF and DSSF yield a good accuracy. Nevertheless, at lower and higher altitudes, SSF is more precise. The reason is that an additional finite-difference approximation is applied to the propagation equation in DSSF. If the vertical step is reduced to $\Delta z = 0.2$ m (0.2λ), as shown in Fig. 1.7c, there is a very good match between SSF and DSSF. This is because the error due to finite differences is reduced.

In this test, the propagation of a beam excited by a complex source point has been simulated. This corresponds to a field with smooth variation. A field with stronger variations is now simulated. It is obtained from a uniform aperture.

1.8.2.b Uniform aperture excitation

An aperture of width a is considered centered at z_s. the field on the aperture is given by

$$u(0,z) = \begin{cases} E_0 & \text{if} \quad z_s - a/2 \le z \le z_s + a/2, \\ 0 & \text{otherwise.} \end{cases} \tag{1.82}$$

Under the far field assumption ($d > 2a^2/\lambda$), the analytic solution for this aperture is given by

$$u(r,z) = E_0 a \cos\theta \sqrt{\frac{jk_0}{2\pi d}} \operatorname{sinc}\left(\frac{k_0 a \sin\theta}{2}\right) e^{-jk_0 d}, \tag{1.83}$$

where $d = \sqrt{(r-r_s)^2 + (z-z_s)^2}$ and θ is the radiation angle as illustrated in Fig. 1.8.

The frequency is 300 MHz. The parameters of the source are $E_0 = 1$ V/m, $a = 3$ m, $r_s = 0$ m, and $z_s = 4000$ m. The parameters of the simulation are $r_0 = 0$ m, $r_{max} = 500$ m, $\Delta r = 10$ m, $z_{max} = 8000$ m, and $\Delta r = 0.2$ m.

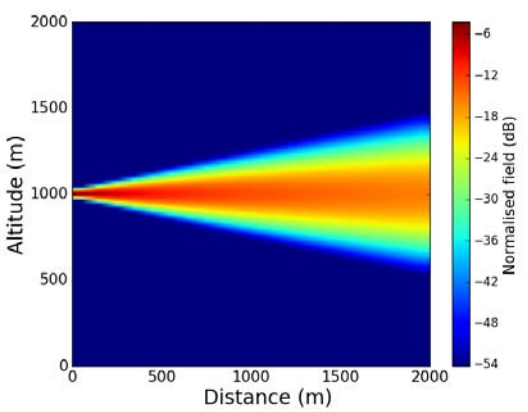

(a) Case $\Delta z = 0.5$ m: Electric field by DSSF

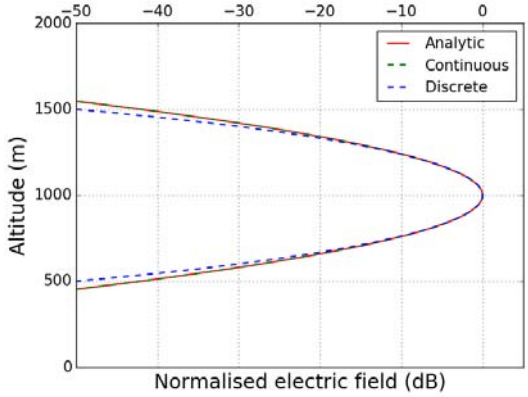

(b) Case $\Delta z = 0.5$ m: Final electric field

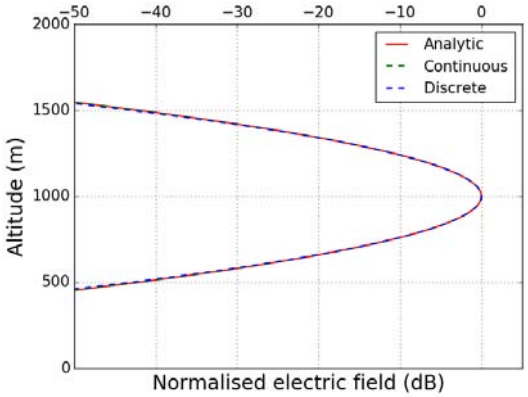

(c) Case $\Delta z = 0.2$ m: Final electric field

Figure 1.7: Free-space propagation of a 2D complex source at altitude 1000 m.

The propagation of the electric field using DSSF is shown in Fig. 1.9a. The secondary lobes can be clearly seen. The final electric fields of SSF, DSSF, and the analytic solution are plotted in Fig. 1.9b. Both SSF and DSSF are accurate compared to the analytic solution. The final electric fields between 3500 m to 4000 m are plotted in Fig. 1.9c. We can see that the maximum and minimum values of the amplitude of SSF and analytic solution match well. In DSSF, the maximum and minimum values are slightly shifted compared to the analytic solution. The displacements are due to the finite-difference approximation in DSSF.

1.8.3 Propagation over a dry ground

In this test, we simulate the propagation over a planar impedance ground. We compare the simulation results of SSF-DMFT and DSSF-DMFT to the 2-ray model.

The altitude of the source center is 20 m, $r_{\max}$ is 5000 m, and Δz is 0.2 m (0.2λ). The

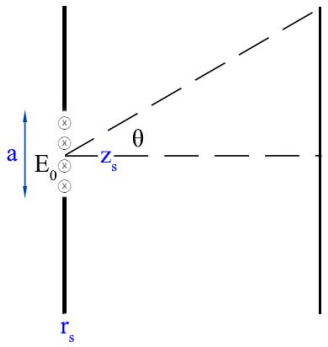

Figure 1.8: 2D uniform aperture.

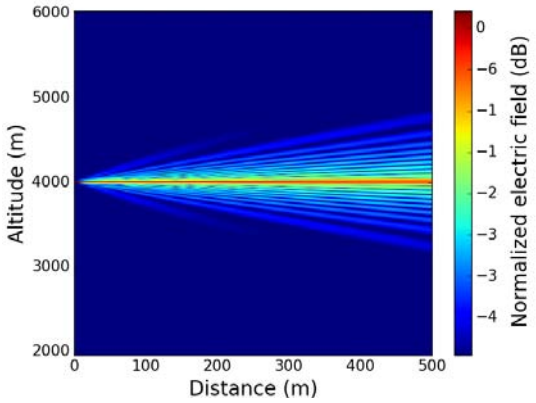

(a) Propagation of the electric field using DSSF-DMFT

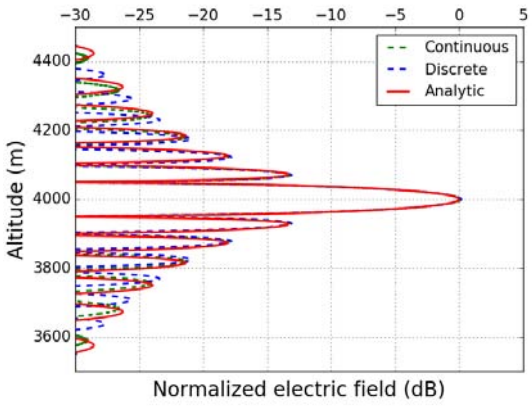

(b) Final electric fields

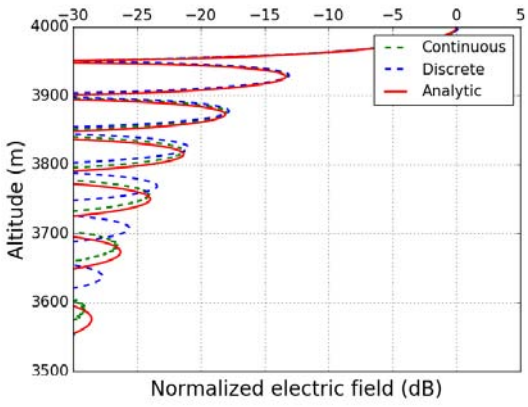

(c) Final electric fields zoomed between 1500 m to 2000 m

Figure 1.9: Free space propagation of a 2D aperture at altitude 2000 m.

other parameters are the same as in the previous test. A dry ground is considered with $\epsilon_r = 20$ and $\sigma = 0.02$ S/m.

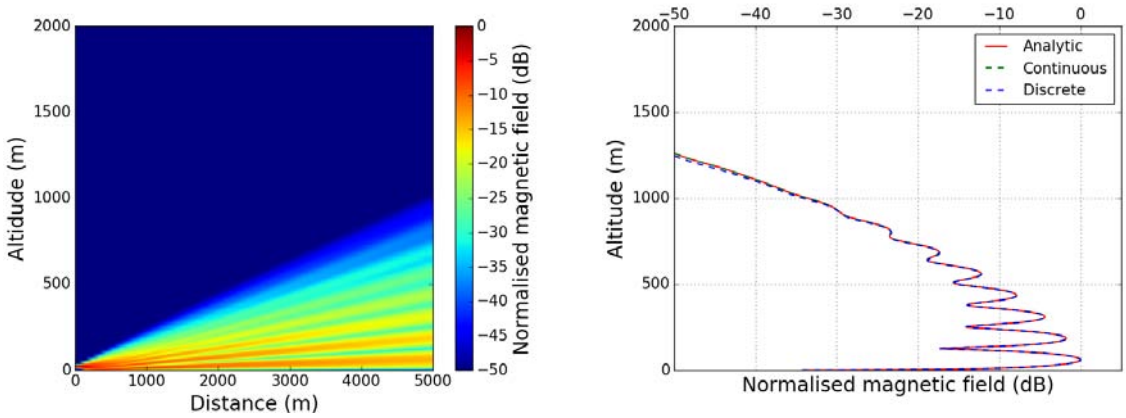

(a) Propagation using DSSF-DMFT (b) Final electric field comparison

Figure 1.10: Propagation of a 2D complex source over a dry ground.

The propagation of the source with TM polarization using DSSF-DMFT is shown in Fig. G.3a. The reflection over the impedance ground is well simulated. The final fields of the two formulations and 2-ray model are shown in Fig. G.3b. The simulation results are the same as the 2-ray model for both propagators.

Note here, for TE polarization, the simulation results with both formulations are accurate.

1.8.4 Propagation over a very dry ground

We now choose a ground with a relative permittivity $\epsilon_r = 2$ and a conductivity $\sigma = 0.001$ S/m. The other parameters are the same as in the previous test.

The field with TM polarization is firstly considered. The propagation using SSF-DMFT is shown in Fig. G.4a. The field has spurious oscillations.

The result of DSSF-DMFT is shown in Fig. G.4b. The result remains accurate. It simulates the propagation as accurately as the 2-ray model.

The final magnetic fields are shown in Fig. G.4c. The final electric fields of DSSF-DMFT and 2-ray model are the same with an acceptable error. SSF-DMFT has much spurious oscillations.

The interest of DSSF-DMFT over SSF-DMFT is that DSSF-DMFT is a self-consistent method in the discrete domain. Thus, as shown in our test, it avoids spurious numerical problems that can occur for certain conditions.

When the simulation is performed for a longer distance $r_{\max} = 7000$ m, for SSF-DMFT, numerical instabilities become so great that the simulated field becomes a numerical noise as shown in Fig. 1.12a. It is believed this spurious solution is due to the inconsistency in SSF-DMFT. DSSF-DMFT avoids these instabilities, as shown in Fig. 1.12b. The self-consistent method remains accuracy.

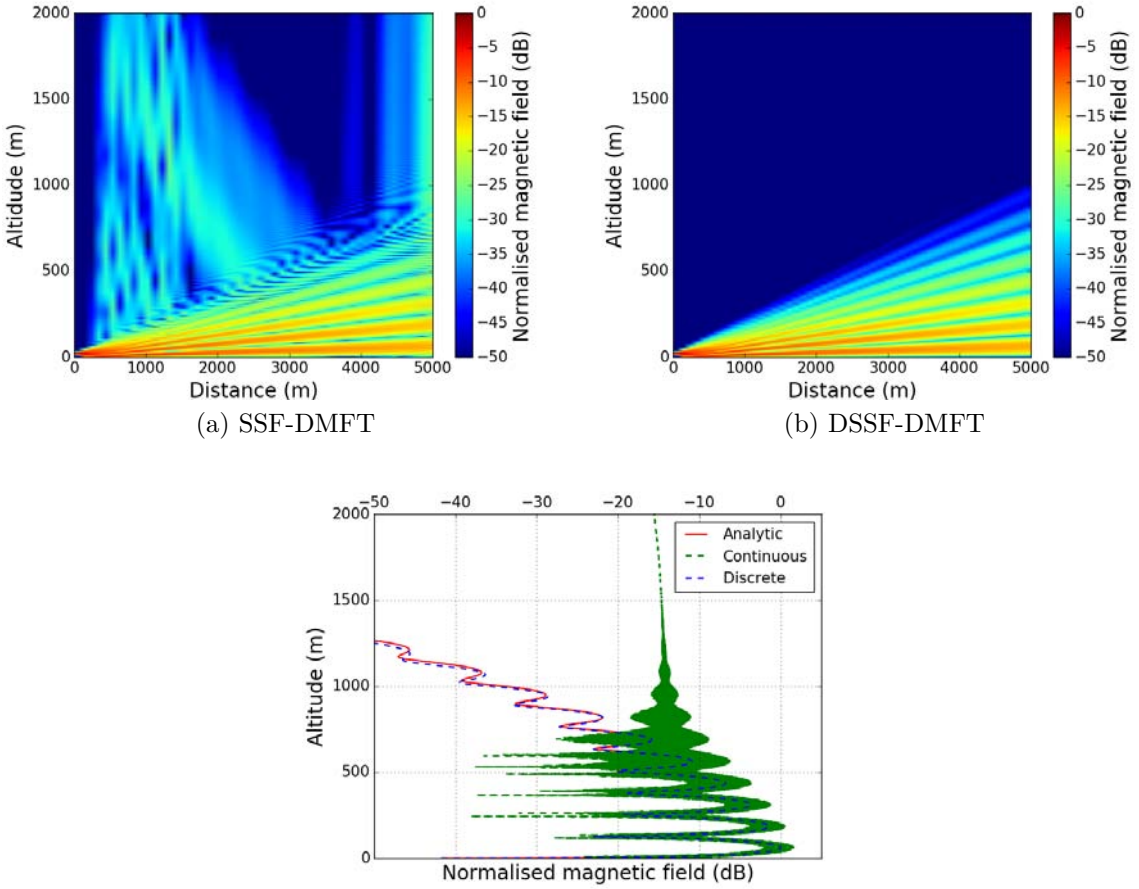

(a) SSF-DMFT

(b) DSSF-DMFT

(c) Final magnetic fields

Figure 1.11: Propagation of a 2D complex source (TM polarization) over a very dry ground for 5000 m.

This spurious error in SSF-DMFT is not present in TE polarization. Therefore, it is believed to come from the ground wave term. This error also disappears when Δz is chosen larger. The theoretical explanation of this instability and its solving with DSSF are still to be studied.

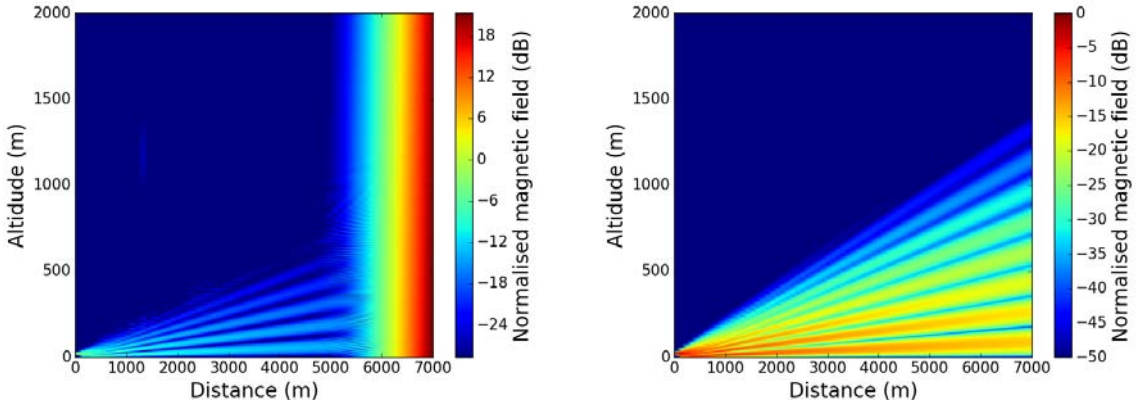

(a) SSF-DMFT (b) DSSF-DMFT

Figure 1.12: Propagation of a 2D complex source (TM polarization) over a very dry ground for 7000 m.

1.8.5 Propagation in a complex environment

In this part, a test of a long-range propagation over an irregular relief in an inhomogeneous atmosphere is tested using DSSF-DMFT.

The parameters of the source are the same as in Section 1.8.2.a except for $z_s = 20$ m.

The simulation parameters are $r_{\max} = 100$ km, $\Delta r = 100$ m, $z_{\max} = 2000$ m, and $\Delta z = 1$ m.

In the vertical direction, we consider a surface-based duct (detailed in Appendix A), which is modelled by a trilinear modified refractivity, as illustrated in Fig. 1.13a. The parameters are: $M_0 = 330$ M-units, $z_b = 100$ m, $z_t = 200$ m, $z_{\max} = 1000$ m, with gradients $c_0 = 0.118$ M-units/m, $c_2 = -0.1$ M-units/m.

The relief is chosen as 2 small triangular hills of heights 100 m and 200 m. The geometric parameters are shown in Fig. 1.13b. The characteristics of the impedance ground are $\epsilon_r = 20$ and $\sigma = 0.02$ S/m.

The propagation is illustrated in Fig. 1.13c. The refraction effect of the atmospheric duct is well simulated. At range 20 km and altitude 200 m, we can clearly see that the propagation direction is bent due to the duct. Furthermore, the effects of the irregular dielectric ground are also accounted. The computation time is 15.2 s. Thus, DSSF-DMFT has the capacity to simulate the long-range propagation in a complex environment.

1.9 Conclusion

In this chapter, the methods for modeling a long-range propagation with an irregular relief in an inhomogeneous atmosphere have been introduced in 2D.

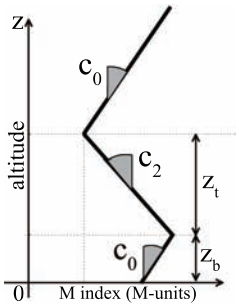

(a) Trilinear model of refractivity

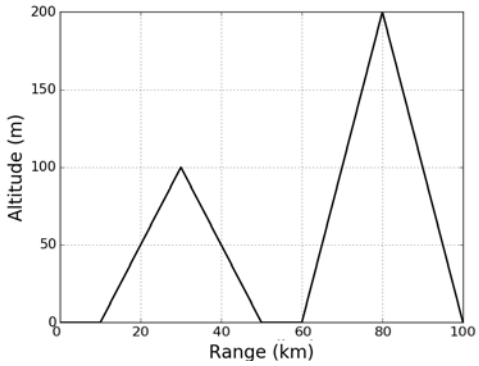

(b) Relief with 2 small triangular hills of heights 100 m and 200 m

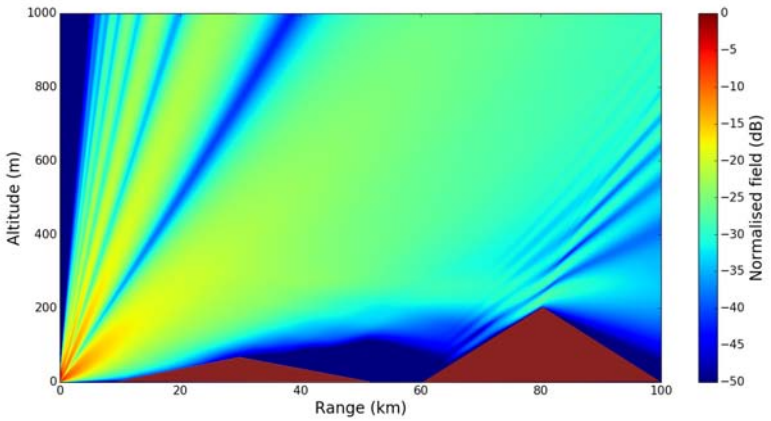

(c) Wave propagation along range

Figure 1.13: Illustration of wave propagation using DSSF-DMFT.

The propagation methods with a PEC ground has been derived. Firstly, the continuous method has been introduced. With a paraxial approximation, the propagation and refraction terms have been treated separately in the spectral and spatial domains. The spectral transform and propagator have been derived from the continuous formulation. The split-step method has been applied to simulate the propagation.

Secondly, for numerically applying the method, a discretization has been performed *a posteriori* on the previous continuous method. The vertical domain is limited to a maximum height, which requires an apodization. The model for considering an irregular relief has been briefly introduced. In this discretized method, SSF-ST, the spectral transform and propagator are all discretized.

Thirdly, by applying the discretization *a priori*, we have proposed a self-consistent discrete formulation for a PEC ground, named DSSF-DST. The spectral transform and the propagator are based on the discrete equations. The propagator is different from the one with SSF-ST.

Then, the propagation methods over an impedance ground have been presented. Firstly, a continuous method with the mixed Fourier transform has been detailed. Secondly, this continuous method has been discretized *a posteriori* to be numerically applied. This method is known to produce spurious errors in certain conditions. Thirdly, a self-consistent method in the discrete domain, DSSF-DMFT, has been proposed. The transform and propagator are derived from the discrete equations. Fourthly, the widely-used SSF-DMFT method has also been described. An inconsistency in this method has been pointed out. Its propagator is derived from the continuous equation, whereas the spectral transform is derived from the discrete one. Thus, the use of the self-consistent method DSSF-DMFT is recommended.

Numerical experiments have been performed. First, the comparisons of the continuous and discrete propagators have been performed. Then, the propagation without ground using SSF and DSSF have been compared. The results are both accurate. For the propagation over an impedance ground, in certain conditions, the continuous operator has spurious oscillations, whereas the discrete propagator remains accurate. Indeed, the discrete propagator is self-consistent and avoids numerical instabilities. Finally, a successful test of a long-range propagation over an irregular relief in an inhomogeneous atmosphere has shown the usefulness of the DSSF-DMFT method.

Chapter 2

3D Discrete Split-Step Fourier Method

2.1 Introduction

In Chapter G.1, the split-step Fourier method has been studied for 2D scene, with either an invariance along y in Cartesian coordinates or a rotational symmetry about the vertical axis in cylindrical coordinates. To model a 3D scene with the latter, a $N\times$ 2D model approximation consisting in scanning all azimuth angles independently is classically used [30]. However, $N\times$ 2D models neglect lateral effects. These latter can be significant, especially in the case of an irregular relief and/or non-constant refractive index. To handle 3D effects, 3D split-step Fourier algorithms are required to simulate properly the propagation in a complex three-dimensions environment. In this chapter, a 3D self-consistent SSF method is proposed.

2.1.1 Context and state of the art

In the context of underwater propagation of acoustic waves, 3D finite-difference or split-step Fourier methods have been extensively used [33][34][35][36]. The 3D models demonstrate a better accuracy than $N\times$ 2D models where azimuthal couplings are present. The acoustic pressure and electromagnetic fields both satisfy the 3D Helmholtz equation, so the 3D propagation can be developed similarly for acoustic and electromagnetic propagations. Later on, for electromagnetic propagation, an extension of split-step methods based on the parabolic equation to 3D has been developed in Cartesian coordinates [37][38][39].

The previous 3D methods are based on the parabolic equation, in which a paraxial approximation is applied to split the vertical and azimuthal derivative components. In this chapter, this approximation is bypassed by using an exact spectral representation of the field in a homogeneous atmosphere. This representation is obtained through a diagonalization of the vertical operator as proposed by Chabory *et al.* [77]. Janaswamy has also derived a similar representation [78]. Besides, this operator has been extended to

3D in cylindrical coordinates in [79]. These methods are more accurate since no paraxial approximation is assumed. Indeed, they are derived from the Helmholtz equation, not from its parabolic approximated form.

Since the aforementioned methods are used for numerical simulations, the computed fields or potentials are expressed in the discrete domain. Therefore, as in the previous chapter, a discrete formulation of the propagation equation is derived to achieve self-consistency according to the discrete electromagnetic theory [65]. The discrete mixed Fourier transform (DMFT) [32] has been a first effort towards this discrete formulation. Indeed, the boundary condition is given in the discrete domain by expressing the partial derivative along z with a finite-difference approximation. However, the propagator is derived from the continuous spectral equation. This is an inconsistency in the DMFT theory as seen in the previous chapter.

2.1.2 Objective

In this chapter, the objective is to extend the work presented in Chapter G.1 by deriving a 3D model directly from the discrete Helmholtz equation. Consequently, it is self-consistent in the framework of the discrete electromagnetic theory. Moreover, the algorithm proposed in cylindrical coordinates is more consistent with radar configurations than those in Cartesian coordinates. The atmosphere effect is considered in the spatial domain as in 2D methods. A planar ground is assumed. The theoretical developments are given over both a perfect metallic ground and an impedance ground. Considering a slowly varying inhomogeneous atmosphere, the 3D split-step Fourier method is applied. Its explicit numerical scheme is introduced.

This chapter corresponds to the content of Zhou *et al.* [3][4][5].

2.1.3 Outline

In Section G.2.1, a homogeneous atmosphere is considered to express the problem in cylindrical coordinates by means of potentials. The propagation is expressed by means of the discrete spectral representation. In Section 2.3, the continuous formulation of SSF in 3D with a PEC ground, denoted as 3D-SSF-ST, is derived. Then, its discrete counterpart is presented. In Section G.2.3, the self-consistent discrete method for 3D-SSF with a PEC ground, 3D-DSSF-ST, is proposed. In Section 2.5, the explicit numerical scheme in an inhomogeneous atmosphere is obtained from the phase-screens and split-step algorithms. In Section 2.6, for the propagation over an impedance ground, both 3D-SSF-DMFT and 3D-DSSF-DMFT are presented. In Section 2.7, a sectoral propagation method is introduced to reduce the computation time. In Section G.2.6, the sectoral propagation method and the 3D formulation are validated by comparisons with an analytic expression. Finally, numerical tests are performed in the presence of inhomogeneous atmospheres to show the accuracy of the methods.

2.2 Configuration

2.2.1 Geometry

The work is treated in cylindrical coordinates with unit vectors $(\hat{\boldsymbol{r}}, \hat{\boldsymbol{\theta}}, \hat{\boldsymbol{z}})$. We assume that the sources are located in the cylinder $r \leq r_0$ and that the fields are known at $r = r_0$. In a preliminary step, a homogeneous atmosphere, *i.e.*, n is constant, and a PEC planar ground at $z = 0$ are assumed. The propagation is computed in the region $r \geq r_0$, $z \geq 0$.

2.2.2 Hertz potentials

The fields can be decomposed in one transverse electric (TE) and one transverse magnetic (TM) components with respect to z by means of Hertz potentials oriented along z. For the electric field, omitting the time-dependence $e^{j\omega t}$ yields

$$\boldsymbol{E} = k_0^2 n^2 \boldsymbol{\Pi}_\mathrm{e} + \boldsymbol{\nabla}\boldsymbol{\nabla} \cdot \boldsymbol{\Pi}_\mathrm{e} - k_0 \eta_0 n \boldsymbol{\nabla} \times \boldsymbol{\Pi}_\mathrm{h}, \tag{2.1}$$

with k_0 the wavenumber in vacuum, η_0 the impedance in vacuum, $\boldsymbol{\Pi}_\mathrm{e}$ the electric vectorial potential for TM polarization, and $\boldsymbol{\Pi}_\mathrm{h}$ the magnetic vectorial potential for TE polarization. Finally, replacing $\boldsymbol{\Pi}_\mathrm{e}$ by $\frac{\Psi}{\sqrt{r}}\hat{\boldsymbol{z}}$ gives the TM electric field

$$\boldsymbol{E} = \frac{\partial}{\partial r}\left(r^{-\frac{1}{2}}\frac{\partial}{\partial z}\Psi\right)\hat{\boldsymbol{r}} + r^{-\frac{3}{2}}\frac{\partial^2\Psi}{\partial z \partial \theta}\hat{\boldsymbol{\theta}} + \left(r^{-\frac{1}{2}}\frac{\partial^2\Psi}{\partial z^2} + k_0^2 n^2 \Psi\right)\hat{\boldsymbol{z}}. \tag{2.2}$$

Note that the TE component can be formulated in a similar way from a z-directed magnetic potential $\boldsymbol{\Pi}_\mathrm{h} = \frac{\Psi}{\sqrt{r}}\hat{\boldsymbol{z}}$. The main difference in the expression of the electric field.

2.3 Continuous formulation in a homogeneous atmosphere over a PEC ground

In this section, the continuous formulation for 3D propagation in a homogeneous atmosphere over a PEC ground is derived. It is denoted as 3D-SSF-ST. The formulation is based on continuous equations. For numerical applications, a discretization is applied *a posteriori* to the continuous formulation.

2.3.1 Continuous equation

The potential Ψ is the solution of the wave equation in 3D cylindrical coordinates. Hence, it is solution of

$$\frac{\partial^2\Psi}{\partial r^2} + \frac{1}{r^2}\frac{\partial^2\Psi}{\partial \theta^2} + \frac{\partial^2\Psi}{\partial z^2} + \left(k_0^2 n^2 + \frac{1}{4r^2}\right)\Psi = 0. \tag{2.3}$$

Furthermore, due to the PEC ground at $z = 0$, the potential Ψ fulfils the Dirichlet condition

$$\Psi|_{z=0} = 0. \tag{2.4}$$

Note here, for TE polarization, a Neumann boundary should be used.

In the proposed method, the potentials are propagated. The electric field is obtained afterwards from the potentials.

2.3.2 Continuous spectral representation

Since periodic and Dirichlet boundary conditions are imposed along θ and z, the spectral representation amounts to a Fourier series along θ and a continuous sine transform along z, respectively. Hence, the spectral transform, denoted as $\tilde{\Psi} = \mathcal{T}_{\text{f,s}}\Psi$, is explicitly given by

$$\tilde{\Psi}(r, k_z, q_\theta) = \frac{1}{2\pi}\int_0^{2\pi}\int_0^{+\infty} \Psi(r, \theta, z)\sin(k_z z)e^{-jq_\theta\theta}dzd\theta, \tag{2.5}$$

with k_z the spectral variable and $q_\theta \in \mathbb{Z}$.

Applying $\mathcal{T}_{\text{f,s}}$ to (2.3) yields

$$r^2\frac{\partial^2\tilde{\Psi}}{\partial r^2} + (r^2k_r^2 - q_\theta^2)\tilde{\Psi} + \frac{1}{4}\tilde{\Psi} = 0, \tag{2.6}$$

with $k_r^2 = k_0^2n^2 - k_z^2$.

In a homogeneous atmosphere, the potential can be propagated from r_0 to any distance $r > r_0$ in the spectral domain. Indeed, the analytical solution of (2.6) is [80]

$$\tilde{\Psi}(r, k_z, q_\theta) = \frac{H_{q_\theta}^{(2)}(k_r r)}{H_{q_\theta}^{(2)}(k_r r_0)}\sqrt{\frac{r}{r_0}}\tilde{\Psi}(r_0, k_z, q_\theta), \tag{2.7}$$

where $H_{q_\theta}^{(2)}$ denotes the Hankel function of the second kind and of order q_θ. They represent the cylindrical harmonics in free space [81].

When q_θ or $|k_r r|$ is very large, the Hankel function can be approximated by an exponential function, as detailed in Appendix E.

2.3.3 Discretization of the continuous formulation

For obvious numerical reasons, the computation domain is discretized and of finite size. This leads to the discretization of the continuous formulation.

2.3.3.a Grid

The vertical domain is limited to $z \in [0, z_{\max}]$ and the following uniform grid is used

$$\begin{aligned} z &= p_z\Delta z \quad \text{for} \quad p_z = \{0, ..., N_z\}, \\ \theta &= p_\theta\Delta\theta \quad \text{for} \quad p_\theta = \{0, ..., N_\theta - 1\}, \end{aligned} \tag{2.8}$$

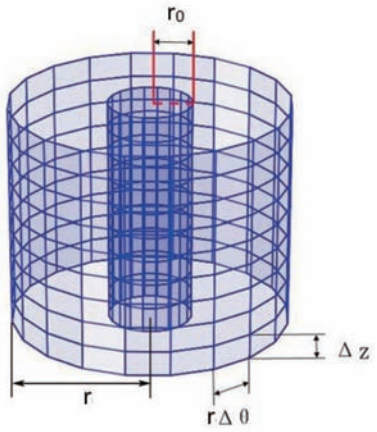

Figure 2.1: Grids along z and θ on the initial cylinder at distance r_0 and on a cylinder at distance $r > r_0$.

with $\Delta z = z_{\max}/N_z$ and $\Delta\theta = 2\pi/N_\theta$. The grid is shown in Fig. G.5.

The potential $\Psi(r_0 + p_r\Delta r, p_z\Delta z, p_\theta\Delta\theta)$ is denoted as Ψ_{p_r,p_z,p_θ}.

2.3.3.b Apodization

As the 2D case in Section G.1.4, the boundary at $z = z_{\max}$ must be perfectly transparent. An apodization is applied and it corresponds to a multiplication by a diagonal matrix $\mathbf{H}$ applied on $\Psi_{p_r,\cdot,\cdot} = \{\Psi_{p_r,p_z,p_\theta}\}_{\forall p_z,p_\theta}$ and the diagonal elements of $\mathbf{H}$ are

$$\mathbf{H}_{p_z,\cdot} = \begin{cases} 1 & \text{for } p_z \in [0, N_z/2], \\ \frac{1+\cos(\pi(\frac{2p_z\Delta z}{z_{\max}}-1))}{2} & \text{for } p_z \in [N_z/2, N_z]. \end{cases} \tag{2.9}$$

After applying the apodization, as no energy reaches the top boundary, any boundary condition can be applied at $z = z_{\max}$. Here, the top boundary is assumed the same as the ground condition. Hence, the problem is simplified to the propagation in a waveguide. The potentials at $p_z = 0$ and $p_z = N_z$ are zeros. Thus, only indices $p_z = \{1, ..., N_z - 1\}$ are considered in Ψ_{p_r,p_z,p_θ}.

2.3.3.c Discretization of the continuous spectral representation

Since discretization is applied on θ and z, the spectral representation (2.5) is discretized. This amounts to a discrete Fourier transform along θ and a discrete sine transform along z. Hence, the spectral transform, denoted as $\tilde{\Psi} = \mathbf{T}_{\text{f,s}}\Psi$, is explicitly given by

$$\tilde{\Psi}_{r,q_\theta,q_z} = \frac{1}{\sqrt{N_\theta}} \frac{1}{\sqrt{2(N_z+1)}} \sum_{p_\theta=0}^{N_\theta-1} \sum_{p_z=1}^{N_z-1} \Psi_{r,p_\theta,p_z} e^{-j\frac{2\pi p_\theta q_\theta}{N_\theta}} \sin\left(\pi \frac{p_z q_z}{N_z}\right), \tag{2.10}$$

where $q_z = \{1, \ldots, N_z - 1\}$, $q_\theta = \{0, \ldots, N_\theta - 1\}$, and $\Psi_{r,p_z,p_\theta} = \Psi(r, p_\theta\Delta\theta, p_z\Delta z)$. Notice here, due to the discretization on z and θ, q_z and q_θ are of finite size.

Using fast trigonometric transforms, the computation of either $\mathbf{T}_{\mathrm{f,s}}\Psi$ or $\mathbf{T}_{\mathrm{f,s}}^{-1}\tilde{\Psi}$ can be efficiently performed, typically in $N_\theta N_z \log_2 N_\theta N_z$ operations.

2.3.3.d Discretized propagator from the continuous formulation

Using the previous discretization, the propagation from $r_{p_r} = r_0 + p_r \Delta r$ r_{p_r+1} is given by

$$\tilde{\Psi}^{\mathrm{p}}_{p_r+1,q_z,q_\theta} = P_{\mathrm{f,s}}[p_r, q_z, q_\theta]\tilde{\Psi}_{p_r,q_z,q_\theta}, \tag{2.11}$$

where $\tilde{\Psi}^{\mathrm{p}}$ represents the propagated spectrum with an upperscript 'p'. The propagator is given by

$$P_{\mathrm{f,s}}[p_r, q_z, q_\theta] = \frac{H^{(2)}_{q_\theta}(k_r r_{p_r+1})}{H^{(2)}_{q_\theta}(k_r r_{p_r})}\sqrt{\frac{r_{p_r+1}}{r_{p_r}}} \tag{2.12}$$

where $q_z = \{1, \ldots, N_z - 1\}$, $q_\theta = \{0, \ldots, N_\theta - 1\}$ and $H^{(2)}_{q_\theta}$ denotes the Hankel function of the second kind and order q_θ. The corresponding diagonal propagation operator is denoted as $\mathbf{P}_{\mathrm{f,s}}$. In addition, $(k_r)^2 = k_0^2 n^2 - (k_z)^2$, and

$$k_z = q_z \Delta k_z, \tag{2.13}$$

with

$$\Delta k_z = \frac{\pi}{z_{\max}}. \tag{2.14}$$

The spectral variable k_z is discretized due to the limited height $z_{\max}$.

The discretization of the continuous formulation has been derived. This discretization is performed *a posteriori*. In the next section, an entire discrete formulation is derived, where the discretization is applied *a priori*.

2.4 Discrete formulation in a homogeneous atmosphere over a PEC ground

In this section, we propose a discrete formulation of the spectral propagator to achieve self-consistency. Unlike the previous section, the discrete formulation is based on the discrete propagation equation. This method is called 3D-DSSF-DST.

2.4.1 Discrete equation

The discretization is applied on directions θ and z. The differential term on r is kept and solved afterwards. To obtain the discretized counterpart of (2.3), the second-order spatial derivatives with respect to θ and z are discretized on the interior points of the grid using the central-difference approximation. This yields

$$\frac{\partial^2 \Psi_{r,p_z,p_\theta}}{\partial r^2} + \frac{1}{r^2}\mathbf{d}_\theta^2 \Psi_{r,p_z,p_\theta} + \mathbf{d}_z^2 \Psi_{r,p_z,p_\theta} + \left(k_0^2 n^2 + \frac{1}{4r^2}\right)\Psi_{r,p_z,p_\theta} = 0, \tag{2.15}$$

with

$$\begin{aligned}\mathbf{d}_z^2\Psi_{r,p_z,p_\theta} &= \frac{1}{\Delta z^2}(\Psi_{r,p_z+1,p_\theta} - 2\Psi_{r,p_z,p_\theta} + \Psi_{r,p_z-1,p_\theta}),\\ \mathbf{d}_\theta^2\Psi_{r,p_z,p_\theta} &= \frac{1}{\Delta\theta^2}(\Psi_{r,p_z,p_\theta+1} - 2\Psi_{r,p_z,p_\theta} + \Psi_{r,p_z,p_\theta-1}).\end{aligned} \tag{2.16}$$

2.4.2 Discrete spectral representation

To render our spectral representation numerically self-consistent, we directly start from (G.24). Applying a discrete Fourier transform along p_θ and a discrete sine transform along p_z on (G.24) yields

$$r^2\frac{\partial^2\tilde{\Psi}}{\partial r^2} + \left(r^2(k_r)^2 - \kappa_{q_\theta}^2\right)\tilde{\Psi} + \frac{1}{4}\tilde{\Psi} = 0, \tag{2.17}$$

where

$$\kappa_{q_\theta} = \frac{2}{\Delta\theta}\sin\left(\frac{\pi q_\theta}{N_\theta}\right) \text{ for } q_\theta = \{0, ..., N_\theta - 1\}, \tag{2.18}$$

and $(k_r)^2 = k_0^2 n^2 - (k_z)^2$ with

$$k_z = \frac{2}{\Delta z}\sin\left(\frac{\pi q_z}{2N_z}\right) \text{ for } q_z = \{1, ..., N_z - 1\}. \tag{2.19}$$

The formulations of (G.27) and (G.28) can be demonstrated similarly as in Section 1.5.2.

In a homogeneous atmosphere, the potential can be propagated from r_{p_r} to r_{p_r+1} in the spectral domain. Indeed, the analytical solution of (G.26) is [80]

$$\tilde{\Psi}^{\mathrm{p}}_{p_r+1,q_z,q_\theta} = P^{\mathrm{d}}_{\mathrm{f,s}}[p_r, q_z, q_\theta]\tilde{\Psi}_{p_r,q_z,q_\theta} \tag{2.20}$$

where

$$P^{\mathrm{d}}_{\mathrm{f,s}}[p_r, q_z, q_\theta] = \frac{H^{(2)}_{\kappa_{q_\theta}}(k_r r_{p_r+1})}{H^{(2)}_{\kappa_{q_\theta}}(k_r r_{p_r})}\sqrt{\frac{r_{p_r+1}}{r_{p_r}}} \tag{2.21}$$

The corresponding diagonal propagation operator is denoted $\mathbf{P}^{\mathrm{d}}_{\mathrm{f,s}}$.

This equation is similar to the propagation of cylindrical harmonics except for the expressions of k_r and κ because of the discrete formulation. When $q_\theta \ll N_\theta$, *i.e.* for modes slowly varying with θ, the order of the Hankel function becomes an integer ($\kappa \approx q_\theta$) as in (2.7).

2.5 Explicit numerical scheme for a slowly varying refractive index

In this section, in order to consider a slowly varying refractive index, the phase-screens method is applied. The formulation and numerical scheme are presented.

2.5.1 Pseudo-differential operator

We aim at computing the refraction effects in a 3D configuration with the presence of a planar and perfectly conducting ground. The atmosphere is characterized by a slowly varying refractive index n. To treat an inhomogeneous atmosphere, a phase-screens method similar to the 2D case (see Section 1.3.4) is proposed.

From (2.3), we have

$$\left[\frac{1}{k_0^2}\frac{\partial^2}{\partial r^2} + (\mathcal{A}+\mathcal{B}+1)\right]\Psi = 0, \tag{2.22}$$

where

$$\begin{aligned}\mathcal{A}\Psi =& \frac{1}{k_0^2}\left(\frac{1}{r^2}\frac{\partial^2}{\partial\theta^2} + \frac{\partial^2}{\partial z^2} + \frac{1}{4r^2}\right)\Psi,\\ \mathcal{B}\Psi =& (n^2-1)\Psi.\end{aligned} \tag{2.23}$$

Here, the terms $\mathcal{A}$ and $\mathcal{B}$ are the 3D extension of (1.19).

We apply the PE approximation on (2.22). Then, it is solved by the split-step method as in Section 1.3.4.

2.5.2 Numerical scheme

As with other split-step methods [12], the computation is performed marching on in distance. Between two consecutive cylinders, we propagate the potential through a homogeneous medium using the spectral propagator. Then we apply a phase screen to account for the refraction index variations.

At each iteration p_r, the propagation, the apodization, and the local refractive index are considered using the 5 steps described below:

1. The potential Ψ on the cylinder at distance r_{p_r} is expressed in the spectral domain by means of the transform $\mathbf{T}_{\text{f,s}}$ defined by (2.10).

2. The spectrum is propagated from r_{p_r} to r_{p_r+1} by applying the spectral operator $\mathbf{P}_{\text{f,s}}$ in 3D-SSF-ST, or $\mathbf{P}^{\text{d}}_{\text{f,s}}$ in 3D-DSSF-DST.

3. The potential is expressed in the spatial domain with the transform ${\mathbf{T}_{\text{f,s}}}^{-1}$.

4. To remove reflections over the top boundary, an apodization is applied with $\mathbf{H}$.

5. A phase screen is applied which corresponds to a multiplication by

$$R_{p_r,p_\theta,p_z} = \exp\left(jk_0(n_{p_r,p_\theta,p_z}-1)\Delta r\right), \tag{2.24}$$

   where n_{p_r,p_θ,p_z} is the refractive index at the position $(r_{p_r}, p_\theta\Delta\theta, p_z\Delta z)$. The corresponding diagonal operator is $\mathbf{R}$. The refraction term can be seen as a perturbation of the propagation in homogeneous medium.

To conclude, in 3D-SSF-ST, the propagation from r_{p_r} to r_{p_r+1} is simulated step by step as

$$\Psi_{p_r+1} = \mathbf{HRT}_{\mathrm{f,s}}{}^{-1}\mathbf{P}_{\mathrm{f,s}}\mathbf{T}_{\mathrm{f,s}}\Psi_{p_r}. \tag{2.25}$$

The only difference between 3D-SSF-ST and 3D-DSSF-DST is that $\mathbf{P}_{\mathrm{f,s}}$ is replaced by $\mathbf{P}^{\mathrm{d}}_{\mathrm{f,s}}$.

The final computation complexity of this method is of order $N_r N_\theta N_z \log_2 N_\theta N_z$.

In the final step, the field is calculated from the potentials. To do so, the field spectrum is obtained from the potential spectrum by applying (G.23) in the spectral domain. Indeed, derivatives are easier to compute in the spectral domain. Finally, $\mathbf{T}_{\mathrm{f,s}}{}^{-1}$ is applied to obtain the potentials.

2.6 3D methods for the propagation over an impedance ground

In this section, the methods for simulating the propagation over an impedance ground are presented. These methods, initially developed in 2D in Chapter G.1, are here extended to 3D.

2.6.1 Extension of the 2D discrete mixed Fourier transform to 3D

The main steps of 3D methods considering an impedance ground are described as follows:

1. On p_θ, the spectral transform amounts to a DFT. The spectrum of Ψ is denoted as $\bar{\Psi}$.
2. On p_z, the DMFT is applied to $\bar{\Psi}$. The spectrum $\tilde{\Psi}$ is obtained.
3. The propagation from r_{p_r} to r_{p_r+1} is computed by multiplying by the propagators for the space and surface waves. The formulations of the propagators will be derived in Section 2.6.2.
4. On p_z, the inverse DMFT is performed. $\bar{\Psi}$ is retrieved.
5. Finally, the inverse DFT along p_θ is performed to obtain the propagated potential Ψ.
6. The refractivity and the apodization are considered in the spatial domain as in Section 2.5.

2.6.2 Spectral propagators

According to Step 2 of Section 2.6.1, DMFT is applied on $\bar{\Psi}$ to obtain $\tilde{\Psi}$. Similarly as presented in Section 1.7.3, due to a variable substitution, the discrete impedance boundary

condition on $\bar{\Psi}$ is replaced by a Dirichlet condition on $\tilde{\Psi}$. Moreover, $\tilde{\Psi}_{p_r,q_z,q_\theta}$ with $q_z \in \{1, N_z - 1\}$ corresponds to the space wave and $\tilde{\Psi}_{p_r,0,q_\theta}$, $\tilde{\Psi}_{p_r,N_z,q_\theta}$ correspond to the surface waves.

In this subsection, Step 3 of Section 2.6.1 is detailed and the propagators are derived. First, a self-consistent method in the discrete domain is presented. Then, for comparison, the 3D extension of the inconsistent method is detailed.

2.6.2.a Self-consistent method: 3D-DSSF-DMFT

In this subsection, the propagators for the self-consistent method 3D-DSSF-DMFT are presented.

The propagation from r_{p_r} to r_{p_r+1} is performed by $\tilde{\Psi}^{\mathrm{p}}_{p_r+1,\boldsymbol{\cdot},\boldsymbol{\cdot}} = \mathbf{P}^{\mathrm{d}}_{\mathrm{f,m}} \tilde{\Psi}_{p_r,\boldsymbol{\cdot},\boldsymbol{\cdot}}$, which is explicitly given by

$$\tilde{\Psi}^{\mathrm{p}}_{p_r+1,q_z,q_\theta} = P^{\mathrm{d}}_{\mathrm{f,m}}[p_r, q_z, q_\theta] \tilde{\Psi}_{p_r,q_z,q_\theta}, \tag{2.26}$$

where $P^{\mathrm{d}}_{\mathrm{f,m}}[p_r, q_z, q_\theta]$ with $q_z \in [1, N_z - 1]$ are the propagators for space wave, whereas $P^{\mathrm{d}}_{\mathrm{f,m}}[p_r, 0, q_\theta]$ and $P^{\mathrm{d}}_{\mathrm{f,m}}[p_r, N_z, q_\theta]$ are the ones for surface waves.

The propagators for these two components are described as follows:

- Space waves:

  Since Dirichlet conditions are assumed at the boundaries, the formulation of the propagator is the same as in (G.29). The propagator is given by

  $$P^{\mathrm{d}}_{\mathrm{f,m}}[p_r, q_z, q_\theta] = \frac{H^{(2)}_{\kappa_{q_\theta}}(k_r r_{p_r+1})}{H^{(2)}_{\kappa_{q_\theta}}(k_r r_{p_r})} \sqrt{\frac{r_{p_r+1}}{r_{p_r}}}, \tag{2.27}$$

  for $q_z = \{1, N_z - 1\}$, $q_\theta = \{0, \ldots, N_\theta - 1\}$.

- Surface waves:
  This formulation is derived from the discrete wave equation (G.24) with $n = 1$. After applying DFT along p_θ, we have

  $$\frac{\partial^2 \bar{\Psi}}{\partial r^2} - \frac{\kappa^2_{q_\theta}}{r^2} \bar{\Psi} + \mathbf{d}^2_z \bar{\Psi} + \left(k_0^2 + \frac{1}{4r^2}\right) \bar{\Psi} = 0. \tag{2.28}$$

  The surface wave components $\tilde{\Psi}_{p_r,0,q_\theta} \gamma^{q_z}$ and $\tilde{\Psi}_{p_r,N_z,q_\theta} (-\frac{1}{\gamma})^{q_z}$ satisfy (2.28). The details of the formulation can be found in Appendix F. This yields

  $$\begin{aligned} P^{\mathrm{d}}_{\mathrm{f,m}}[p_r, 0, q_\theta] &= \frac{H^{(2)}_{\kappa_{q_\theta}}(k_{\mathrm{sw}_1} r_{p_r+1})}{H^{(2)}_{\kappa_{q_\theta}}(k_{\mathrm{sw}_1} r_{p_r})} \sqrt{\frac{r_{p_r+1}}{r_{p_r}}}, \\ P^{\mathrm{d}}_{\mathrm{f,m}}[p_r, N_z, q_\theta] &= \frac{H^{(2)}_{\kappa_{q_\theta}}(k_{\mathrm{sw}_2} r_{p_r+1})}{H^{(2)}_{\kappa_{q_\theta}}(k_{\mathrm{sw}_2} r_{p_r})} \sqrt{\frac{r_{p_r+1}}{r_{p_r}}}, \end{aligned} \tag{2.29}$$

  where

  $$\begin{aligned} k_{\mathrm{sw}_1} &= \sqrt{k_0^2 + (\gamma + \gamma^{-1} - 2)/(\Delta z)^2}, \\ k_{\mathrm{sw}_2} &= \sqrt{k_0^2 + ((-\gamma) + (-\gamma)^{-1} - 2)/(\Delta z)^2}. \end{aligned} \tag{2.30}$$

2.6.2.b Inconsistent method: 3D-SSF-DMFT

The SSF-DMFT method is here extended to 3D. This method is called 3D-SSF-DMFT. The propagation operator $\mathbf{P}_{\mathrm{f,m}}$ corresponds to multiplying the spectral potentials by $P_{\mathrm{f,m}}[p_r, q_z, q_\theta]$, which is given as follows:

- Space waves:
  The formulation of the propagator for the space wave is the same as in (2.11). The propagator $P_{\mathrm{f,m}}[p_r, q_z, q_\theta]$ is given by

$$P_{\mathrm{f,m}}[p_r, q_z, q_\theta] = \frac{H^{(2)}_{q_\theta}(k_r r_{p_r+1})}{H^{(2)}_{q_\theta}(k_r r_{p_r})} \sqrt{\frac{r_{p_r+1}}{r_{p_r}}}, \tag{2.31}$$

  for $q_z = \{1, N_z - 1\}$, $q_\theta = \{0, \ldots, N_\theta - 1\}$.

- Surface waves:
  This formulation is derived from the continuous wave equation (2.3) with $n = 1$. After applying the continuous sine transform along θ, we have

$$\frac{\partial^2 \bar{\Psi}}{\partial r^2} - \frac{q_\theta^2}{r^2}\bar{\Psi} + \frac{\partial^2 \bar{\Psi}}{\partial z^2} + \left(k_0^2 + \frac{1}{4r^2}\right)\bar{\Psi} = 0. \tag{2.32}$$

  The surface waves are propagated by substituting $\tilde{\Psi}_{p_r,0,q_\theta}\gamma^{\frac{z}{\Delta z}}$ and $\tilde{\Psi}_{p_r,N_z,q_\theta}(-\frac{1}{\gamma})^{\frac{z}{\Delta z}}$ into (2.32) and solving. This yields

$$\begin{aligned} P_{\mathrm{f,m}}[p_r, 0, q_\theta] &= \frac{H^{(2)}_{q_\theta}(k_{\mathrm{sw}_1} r_{p_r+1})}{H^{(2)}_{q_\theta}(k_{\mathrm{sw}_1} r_{p_r})} \sqrt{\frac{r_{p_r+1}}{r_{p_r}}}, \\ P_{\mathrm{f,m}}[p_r, N_z, q_\theta] &= \frac{H^{(2)}_{q_\theta}(k_{\mathrm{sw}_2} r_{p_r+1})}{H^{(2)}_{q_\theta}(k_{\mathrm{sw}_2} r_{p_r})} \sqrt{\frac{r_{p_r+1}}{r_{p_r}}}, \end{aligned} \tag{2.33}$$

  where

$$\begin{aligned} k_{\mathrm{sw}_1} &= \sqrt{k_0^2 + (\ln\gamma)^2/(\Delta z)^2}, \\ k_{\mathrm{sw}_2} &= \sqrt{k_0^2 + (\ln(-\gamma))^2/(\Delta z)^2}. \end{aligned} \tag{2.34}$$

This method is an extension of SSF-DMFT in 3D. The spectral transform is based on the discrete impedance boundary condition, whereas the spectral propagator is obtained from continuous spectral equations.

Compared to 3D-DSSF-DMFT, the expression of the propagators is different. It is the only difference between 3D-SSF-DMFT and 3D-DSSF-DMFT.

The spectral propagators of the methods have been derived. In the next section, a sectoral propagation method is presented to alleviate the computation burden.

2.7 Sectoral propagation

2.7.1 Principle

When computing the propagation in a complex environment, two situations may occur. In the first one, we are only interested in the field within a limited angular width. In such a case, the most suitable solution in terms of computation time is to limit the computation domain to this angular sector and to impose absorbing boundary conditions [82]. In the second situation, one wants to compute the complete field, without truncating any energy. This is our aim here. Rather than simulating the propagation in the entire space with $\theta \in [0, 2\pi[$, the simulation can be limited to the sector where the power is located, denoted as the *propagation sector* thereafter. The azimuthal sector is chosen wide enough so that no energy reaches its boundaries.

Doing so, any kind of boundaries can be imposed. Periodic boundary conditions are used because they maintain the validity of the spectral Fourier representation, which renders its computation achievable by FFT.

2.7.2 Formulation

A propagation sector of width θ_s in azimuth is chosen. The calculation domain is represented in Fig. 2.2. For the split-step algorithm to remain unchanged, we impose $\theta_\mathrm{s} = \frac{2\pi}{N_\mathrm{s}}$, where N_s is an integer. Finally, the computation domain is $\theta \in [-\theta_\mathrm{s}/2, \theta_\mathrm{s}/2[$ and $z \in [0, z_\mathrm{max}]$.

If periodic boundary conditions are imposed at $\pm\frac{\theta_\mathrm{s}}{2}$, the sectoral propagation is similar to the 2π-propagation except for a decrease of the angular period by a factor of N_s. Thus, the truncation on θ amounts to a decimation of factor N_s in the spectral domain. This means a N_s times replication in the spatial domain as illustrated in Fig. 2.3. To avoid signal overlap, the sector should be chosen such that no power goes through its boundaries. A numerical criteria will be proposed during the numerical experiments.

Finally, only a slight change in the previous formulation is necessary. The expression of the propagator (G.30) is kept, except for the order of the Hankel function κ_{q_θ} that becomes $\frac{2}{\Delta\theta}\sin\left(\frac{\pi N_\mathrm{s} q_\theta}{N_\theta}\right)$ for $q_\theta = \{0, ..., N_\theta - 1\}$.

2.8 Numerical tests

In the previous sections, a method to compute the propagation in 3D in cylindrical coordinates has been proposed. The aims of the simulations are to test the sectoral propagation and to show that the proposed 3D method achieves to model vertical and azimuthal effects. On the contrary $N\times$ 2D methods cannot take the lateral effects into account. In addition, the propagation over an impedance ground with 3D-SSF-DMFT and 3D-DSSF-DMFT are compared. Finally, a simulation in a realistic atmosphere is performed.

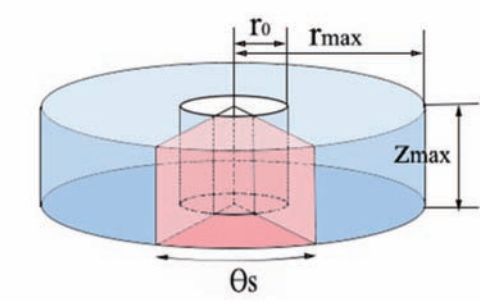

Figure 2.2: Propagation sector of azimuthal width $\theta_s = \frac{2\pi}{N_s}$ (in pink).

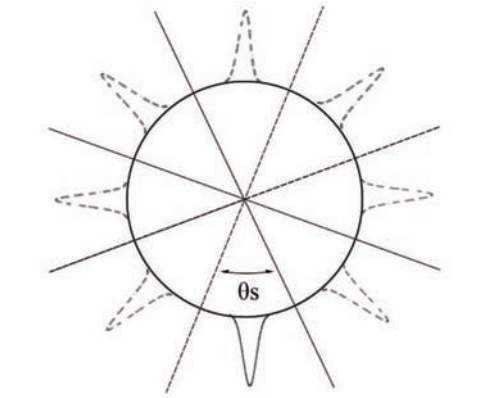

Figure 2.3: Decimation of a factor N_s in the spectral domain amounts to a N_s times duplications in the spatial domain ($N_s = 8$ in this figure).

In the simulations, the choice of the steps Δz and $\Delta\theta$ depends on the Nyquist sampling theorem. The vertical and azimuthal samplings for all the propagation methods should be as [83]

$$\Delta z \leq \frac{\lambda}{2\sin(\alpha_{\max})}, \tag{2.35}$$

and

$$\Delta\theta \leq \frac{\lambda}{2r_{\max}\sin(\alpha_{\max})}, \tag{2.36}$$

where $\alpha_{\max}$ is the maximum divergence angle of the beam with respect to its propagation direction.

In the following simulations, for the sake of simplicity, we use a fixed azimuthal grid, even if this yields a large number of points in azimuth to satisfy the Nyquist condition at the final distance r, which are not necessary for the previous distances. Several schemes could be used to adapt the number of points in azimuth with range [83] [84]. These schemes could be applied to the proposed formulation to reduce the computation time.

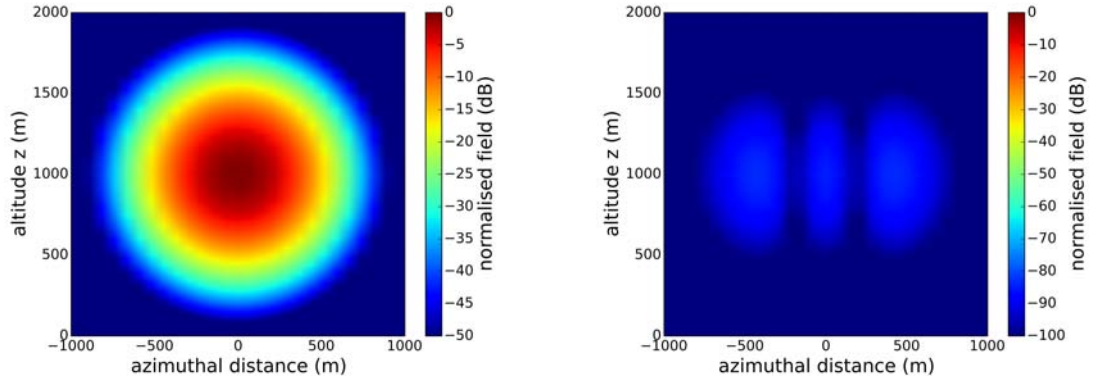

(a) Normalized electric field at the final step of the sectoral propagation

(b) Difference between DSSF and the analytic solution

Figure 2.4: Comparison between the 3D sectoral propagation and the analytic solution.

2.8.1 Validation of the sectoral propagation in free space

In order to test the sectoral propagation, a complex source point [76] is propagated and compared to its analytic expression.
The frequency is 3 GHz. The complex source is located at $x_s = \frac{jk_0W_0^2}{2}$, $y_s = 0$ m, $z_s = 1000$ m, with $W_0 = 1$ m. The simulation parameters are: $r_0 = 2$ km, $r_{\max} = 12$ km, $\Delta r = 200$ m, $z_{\max} = 2000$ m, $\Delta z = 0.2$ m, and $N_\theta = 1000$. The propagation is in free space.

Because a complex source corresponds to a Gaussian beam upon assuming the paraxial approximation, an angular sector of width 2 arctan $\left(\frac{2}{k_0W_0}\right)$ contains 88.47 % of the beam power in the far field zone [24]. To guarantee that no power reaches the boundaries, the sector is chosen 5 times larger. This yields $\theta_s = \frac{\pi}{10}$ and $N_s = 20$.

The electric field at distance $r_{\max}$ computed with the sectoral propagation is shown in Fig. 2.4(a). The difference between the sectoral propagation and the analytic solution is shown in Fig. 2.4(b). The maximum difference is of order -73 dB. This difference is negligible. Therefore, the 3D sectoral propagation method is considered as successfully tested.

The computation time of the sectoral propagation method is about 80 s, whereas the total 2π propagation spends about 28 min. The computation time is thus significantly reduced.

2.8.2 Test of a 45°-slanted linear refractivity index model

The method is now applied on a 3D scenario with an inhomogeneous atmosphere characterized by a 45°-slanted linear refractivity index.

The atmosphere effects are considered through the refractive index n and the modified

refractivity M given by [85]

$$M = (n-1) \times 10^6 + \frac{z}{R_\mathrm{E}}, \tag{2.37}$$

where z is the height above the Earth's surface and R_E is the Earth's radius.

The configuration parameters are as follows: the frequency is 3 GHz. The complex source is at an altitude of 500 m with $W_0 = 3$ m. The modified refractivity M varies linearly along the direction $\hat{\boldsymbol{v}} = \frac{1}{\sqrt{2}}(\hat{\boldsymbol{y}} + \hat{\boldsymbol{z}})$. The modified refractivity gradient along $\hat{\boldsymbol{v}}$ is $c_1 = dM/d\boldsymbol{v} = 1$ M-unit/m. This value is chosen strong in order to obtain significant refraction effects, even at few kilometers.

The parameters of the simulation are as follows: $r_0 = 2$ km, $r_\mathrm{max} = 12$ km, $\Delta r = 500$ m, $z_\mathrm{max} = 1000$ m, $\Delta z = 0.2$ m, and $N_\theta = 30000$.

The initial and final fields are plotted in Fig. 2.5. The beam center of the final field is shifted in both altitude and azimuth due to refraction. The shifts of the beam center in z and θ are 35.81 m and 34.80 m, respectively. This corresponds to angular deviations of the beam axis of 0.205° and 0.199°, respectively.

According to ray theory [86], this shift is given by

$$l_\mathrm{shift} = \frac{(r_\mathrm{max} - r_0)^2 c \times 10^{-6}}{2}. \tag{2.38}$$

The numerical application yields $l_\mathrm{shift} = 35.36$ m. The beam center deviation using ray theory is 0.203°. Thus, the difference with our results is of order of 0.004°, which is very small.

The ray approximation and the simulated values in the 2 directions are the same within an acceptable error. Therefore, the effects of the inhomogeneous atmosphere on vertical and horizontal directions are properly simulated. Note that the displacement along θ can not be simulated by a $N\times$2D method.

2.8.3 Tests on a 2D atmospheric duct

A more complex scenario with 3D effects along both vertical and azimuthal directions is presented. We consider a refractive index model identical in both directions with 2 ducts along the vertical and azimuthal directions. Therefore, similar effects are expected along both directions.

The refraction index in the $z - \theta$ plane is obtained by $M = \sqrt{M_z M_\theta}$, where M_z and M_θ are functions associated with the modified refractivity index along z and θ.

In the vertical direction, we consider a surface-based duct, which is modeled by a trilinear function M_z, as illustrated in Fig. G.6a.

The parameters are: $M_0 = 330$ M-units, $z_b = 950$ m, $z_t = 100$ m, $z_\mathrm{max} = 2000$ m, gradients $c_0 = 0.118$ M-units/m, $c_2 = -1.0$ M-units/m. To remove the discontinuities of the gradient that are not realistic, we smoothen the duct by using the moving-averages method on 200 points. The resulting modified refractivity M_z is shown in Fig. G.6a(a).

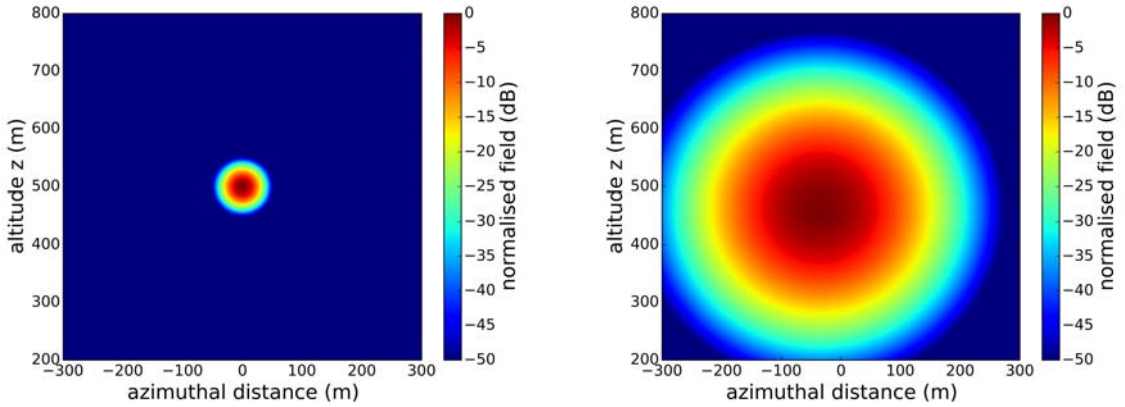

(a) Initial field (b) Final field

Figure 2.5: Initial and final normalized electric fields (dB) about the direction of propagation.

In the azimuthal direction, we use the same model mapped into cylindrical coordinates, as shown in Fig. G.6a(b). Such large index variations in azimuth are not realistic in the troposphere, but are used to compare the 3D effect in θ and z.

Finally, the modified refractivity index on the $z-\theta$ plane is obtained. The refractivity is shown in Fig. G.6b(a) on one cylinder and the gradient is shown in Fig. G.6b(b).

For the simulation, the frequency is 3 GHz. The complex source is at an altitude of 1000 m with $W_0 = 1$ m. The simulation parameters are: $r_0 = 2$ km, $r_{\max} = 12$ km, $\Delta r = 500$ m, $z_{\max} = 2000$ m, $\Delta z = 0.2$ m, and $N_\theta = 30000$.

Similar results along the 2 directions are expected since the ducts are the same along the 2 axes.

The normalized electric field obtained at distance $r_{\max} = 12$ km is shown in Fig. G.7. We can see the 3D effects due to the 2 ducts along the azimuthal and vertical directions. The maximum value of the final field is located at 63.0 m away from the center on the vertical direction and at 62.8 m away on the azimuthal direction. The 2 values are the same within an acceptable error.

In Fig. 2.10, we plot the electric fields at ± 50 m away from the source beam center. The cuts correspond to the white dotted lines and solid lines in Fig. G.7. As illustrated in Fig. 2.9, along θ, the field is along a horizontal circle of the cylinder, while the field along z is along a vertical straight line. Nevertheless, since in our test a narrow beam is considered, the curvature of the circle is negligible where the field is located. The plots match within 0.05 dB. Therefore, the differences of the fields along the 2 directions are negligible. The effects due to the ducts are the same in both directions. The method is successfully tested since 3D complex effects are simulated.

For a comparison, the result of a $N\times$ 2D method is shown in Fig. 2.11. As in the previous test, we plot the electric fields at ± 50 m away from the source beam center in Fig. 2.12.

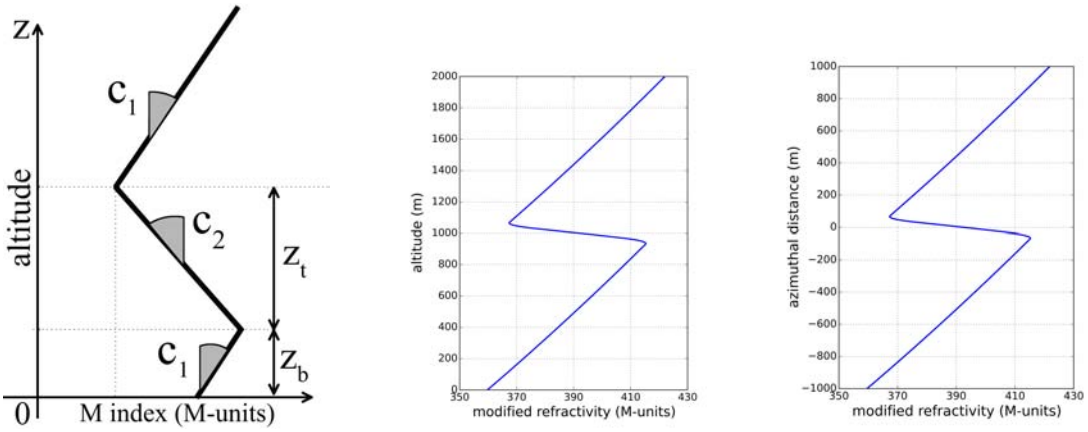

(a) Surface based duct trilinear model (b) Along z (c) Along θ

Figure 2.6: Trilinear refractivity models.

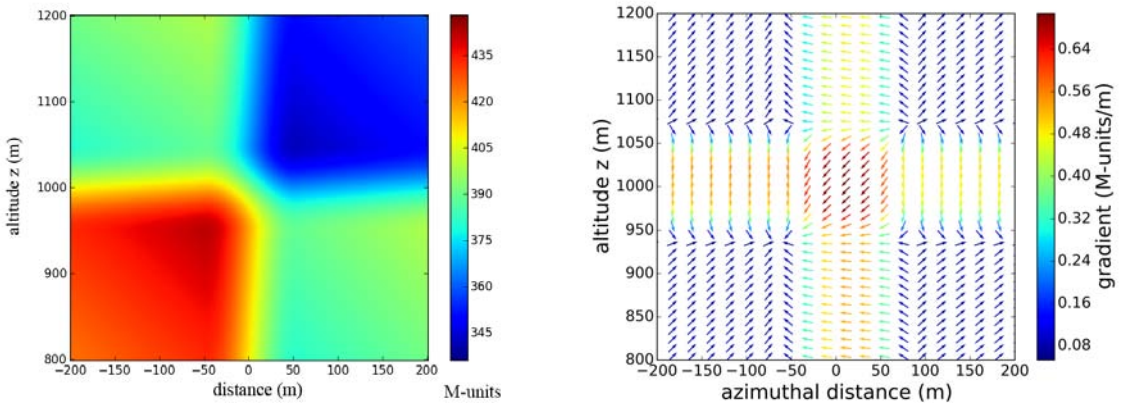

(a) M index (b) Gradient vectors

Figure 2.7: Refractivity (M-units/m) on the $z - \theta$ plane.

The cuts correspond to the white dotted lines and solid lines in Fig. 2.11. Only the vertical effects are accounted in this case. The lateral effects can not be simulated. This yields to a poor accuracy.

2.8.4 3D propagation over an impedance ground

The propagation over an impedance ground is now considered with a relative permittivity $\epsilon_r = 20$ and a conductivity $\sigma = 0.02$ S/m.

A complex source point is considered with $z_s = 15$ m. The other parameters are the same as in the previous test.

The final fields of SSF with both the continuous and discrete propagators and the differences to geometrical optics (GO) are plotted in Fig. 2.13. The maximum difference with

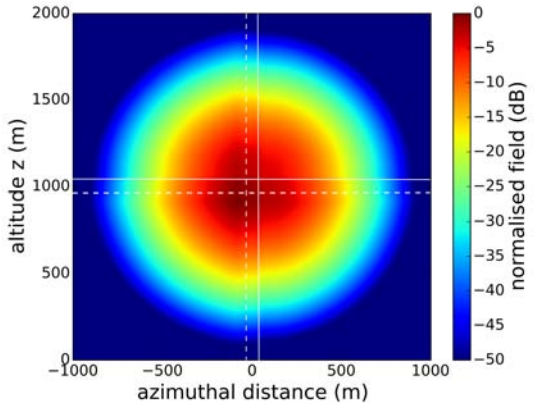

Figure 2.8: Final field of the simulation using the proposed 3D method.

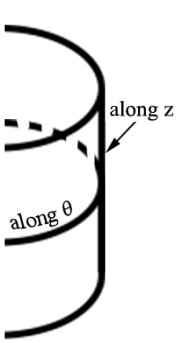

(a) Cylinder on which the field is computed

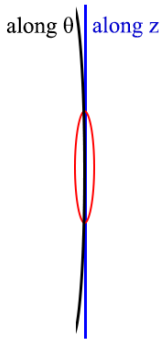

(b) Circle along θ and straight line along z

Figure 2.9: Geometry along z and θ directions.

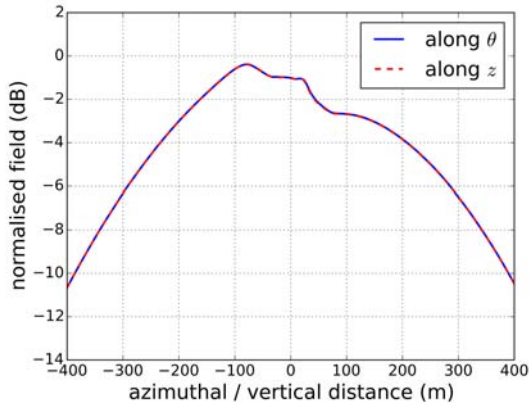

(a) Final fields along the azimuth at altitude 950 m (blue line) and along the vertical at −50 m from the azimuthal center (red dotted line)

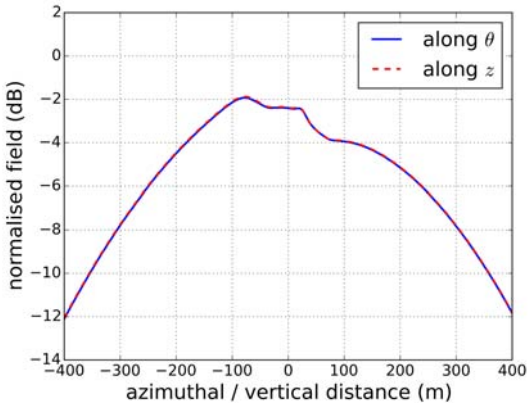

(b) Final fields along the azimuth at altitude 1050 m (blue line) and along the vertical at 50 m from the azimuthal center (red dotted line)

Figure 2.10: Comparison of the fields along z and θ directions with the 3D method.

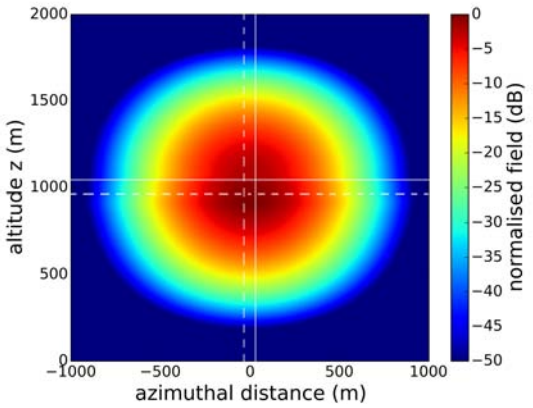

Figure 2.11: Final field of the simulation using the $N\times$ 2D method.

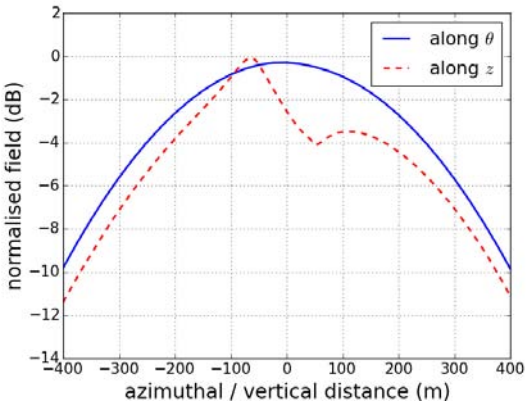

(a) Final fields along the azimuth at altitude 950 m (blue line) and along the vertical at −50 m from the azimuthal center (red dotted line)

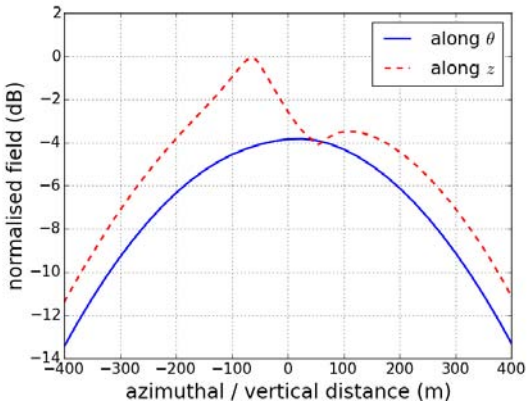

(b) Final fields along the azimuth at altitude 1050 m (blue line) and along the vertical at 50 m from the azimuthal center (red dotted line)

Figure 2.12: Comparison of the fields along z and θ directions with the $N\times$ 2D method.

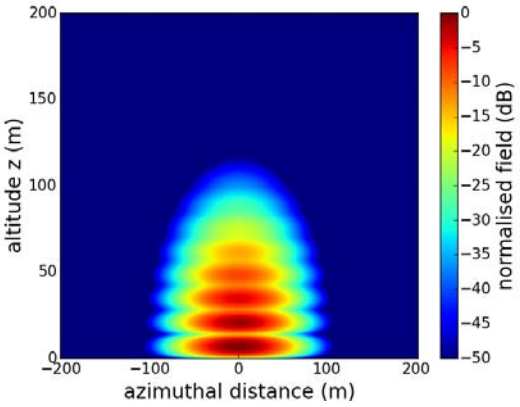

(a) Normalised final electric field of 3D-DSSF-DMFT

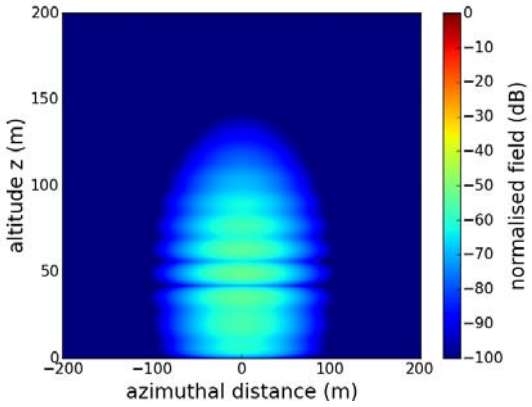

(b) Difference between 3D-SSF-DMFT and GO

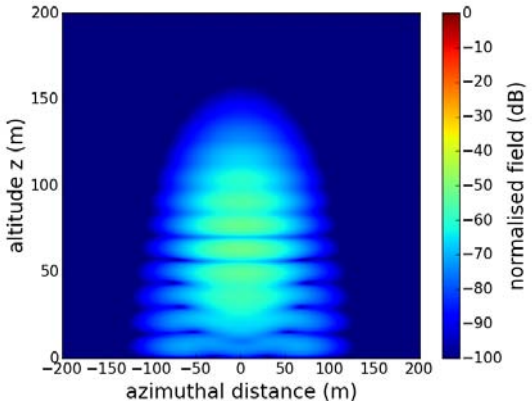

(c) Difference between 3D-DSSF-DMFT and GO

Figure 2.13: Propagation of a 3D complex source point over an impedance ground.

the continuous case is −52.4 dB, whereas the one with the discrete case is −51.9 dB. The 3D-DMFT method with both formulations are accurate.

2.8.5 3D propagation in realistic 3D ducting conditions

To highlight the 3D effects of the atmosphere, a refractive index model in the presence of a duct with azimuthal variations is required. Since we have no measured data of the refractive index with strong azimuthal variations, we choose the ducts retrieved after clutter data inversion by Douvenot *et al.* [87]. In their work, measured clutter data with the Spandar radar [88] of frequency 2.84 GHz are inversed to infer the refractive index along a 90° azimuthal aperture. The retrieved ducts are plotted in Fig. 2.14. We focus on the 24° azimuthal sector where the duct has the stronger azimuthal variation. The maximum gradients are 0.91 M-units/m in vertical and 0.98 M-units/deg in azimuth.

In the simulation, a 2D complex source point at height 30.78 m is used with the same

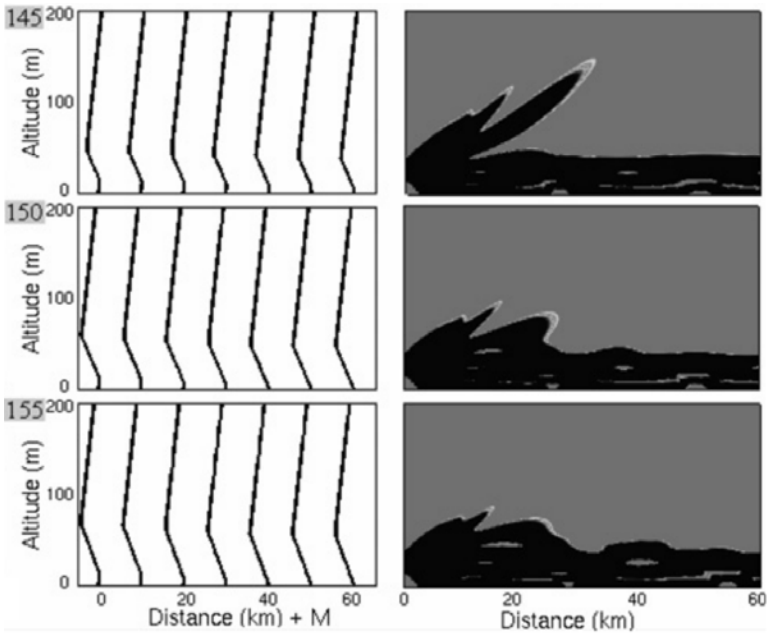

Figure 2.14: Inverted refractive structures and corresponding coverage diagrams for one clutter to noise ratio map from 1998 Wallops Island measurement campaign [87].

frequency as the Spandar radar. The waist width $W_0 = 0.5$ m. The center of the source is at azimuth 150°. The simulation parameters are $r_0 = 2$ km, $r_{\max} = 60$ km, $\Delta r = 0.2$ m, $z_{\max} = 204.8$ m, $\Delta z = 0.2$ m. The sectoral propagation method is applied in a sector from 138° to 162°, discretized on $N_\theta = 10000$ points. The sea surface is modeled as a perfect electric conductor in the test.

The normalized electric field obtained at distance $r_{\max} = 60$ km is shown in Fig. 2.15. (a). Due to the atmospheric ducts over the sea, we can see a modification in the final field. The differences between the normalized final fields obtained with the 3D and the $N\times$ 2D models are shown in Fig. 2.15. (b). The difference is at least -60 dB below the maximum of the field. The difference of the electric field normalized at each range on the horizontal plane at the height of the source between the 3D and $N\times$ 2D methods is shown in Fig. 2.15. (c). The difference is shown to be smaller than -50 dB below the maximum of the field. Therefore, the difference is weak.

The proposed 3D model is theoretically more accurate than the $N\times$ 2D model. However, the difference is here not significant because the azimuthal gradient of refractivity is minor. $N\times$ 2D methods should be preferred, since the 3D method is resource intensive. The computation time of the 3D model is about 1 hour, and the one of $N\times$ 2D model is about 10 mins ($N_\theta = 10000$).

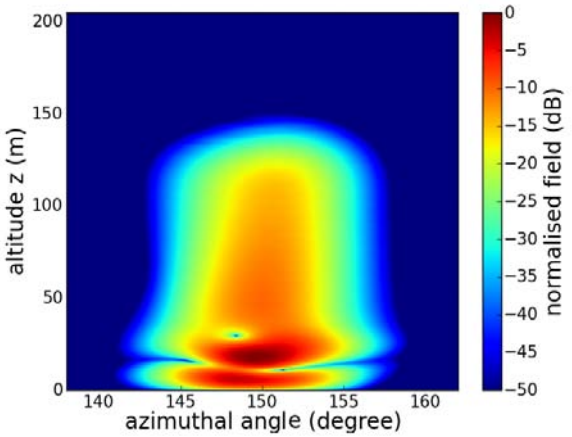

(a) Normalized final electric field (dB) using the proposed 3D method

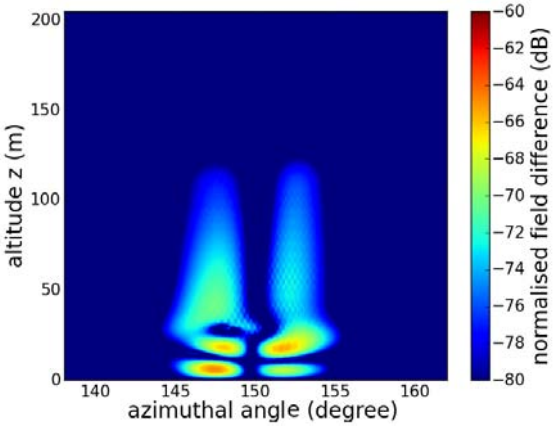

(b) Difference of normalized final electric fields (dB) between 3D and $N\times$ 2D methods

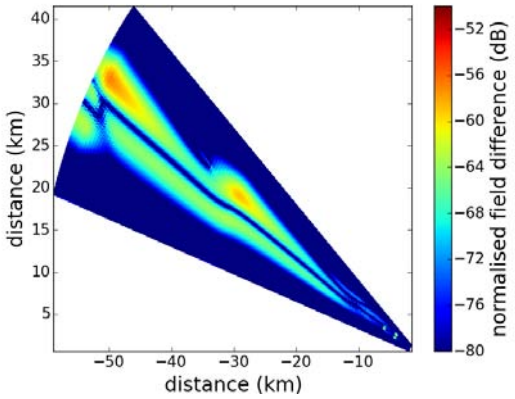

(c) Difference of normalized electric fields (dB) on the horizontal plane at the height of the source between 3D and $N\times$ 2D methods

Figure 2.15: 3D propagation in realistic 3D ducting conditions.

2.9 Conclusion

The 3D propagation method in cylindrical coordinates based on the split-step Fourier method has been introduced.

Firstly, a homogeneous atmosphere has been considered to express the problem by means of Hertz potentials. The continuous 3D formulation using the split-step method with a PEC ground has been presented. The spectral transforms along azimuthal and vertical directions have been detailed. The continuous propagator has been derived for the propagation in the spectral domain. Then, for numerical applications, the domain is of limited vertical height and discretized. The discretization form of the continuous formulation has been developed.

Secondly, a self-consistent discrete formulation of the 3D propagation over a PEC ground has been presented. Rather than applying the discretization *a posteriori* on the continuous formulation, this formulation is developed from the discrete equation. A discrete spectral propagator has been derived.

Thirdly, an explicit numerical scheme for considering a slowly varying refractivity has been introduced. The phase-screens method valid at wide angles is applied in the spatial domain.

Considering an impedance planar ground, the 3D propagation method has been presented. A self-consistent discrete method has been proposed. Another method corresponds to the 3D extension of the 2D SSF-DMFT method. As in 2D, the inconsistency of this method has been highlighted. The propagators in both methods have different expressions. The self-consistent method 3D-DSSF-DMFT has been preferred to achieve self-consistency in the discrete domain.

In many cases, the source is directional. Therefore, a sectoral propagation method has been introduced. The propagation is modified to fit with the reduced computation domain. Depending on the angular size of the propagation sector, the computation time can be drastically reduced.

Numerical tests have been presented. Firstly, the sectoral propagation and the 3D formulation have been validated by a comparison with an analytical solution.

Secondly, the method has been applied in a 3D scenario with an inhomogeneous atmosphere characterized by a 45°-slanted linear refractivity index. The effects of the inhomogeneous atmosphere along vertical and horizontal directions are properly simulated.

Thirdly, a scenario with complex 3D effects along both vertical and azimuthal directions has been introduced. We have considered refractivity conditions with 2 atmospheric ducts along the vertical and azimuthal directions. The refractive effects have been successfully modeled along both directions. This method takes into account the azimuthal effects which is an advantage over $N \times 2D$ models.

Fourthly, the simulation accuracy of 3D SSF methods with both continuous and discrete propagators have been compared to geometrical optics for a propagation over an impedance ground. The results of the methods with both propagators are accurate.

These methods have been successfully tested. However, only the discrete formulation 3D-DSSF-DMFT achieves a self-consistency. Therefore, the latter should be preferred for numerical simulations.

Finally, the method in realistic atmospheric ducting conditions has been tested. Ducts over a sea retrieved after clutter data inversion have been used. Both simulations using 3D and $N\times$ 2D methods have been performed. The 3D model has a better accuracy since lateral effects are considered. However, in these ducting conditions, the azimuthal gradient is not sufficient to have a significant impact on the field.

Chapter 3

Wavelet Transforms and Data Compression

3.1 Introduction

In chapter 2, the split-step Fourier method in 3D has been introduced. This method has a high accuracy and the capacity to model lateral effects. However, if the propagation is simulated in a large computation domain, the computational burden becomes important. Time and memory occupations become the main concerns. Therefore, a method with an improved computation efficiency is sought. For the sake of simplicity, this method is developed for the 2D case. Its 3D extension is not presented in this work.

The wavelet transform is a very efficient tool for data compression and analysis. We intend to use this transform to improve the time and memory requirements in the propagation method. With the wavelet transform, a signal is expanded on elementary wavelike functions. Their waveforms are obtained by scaling and translating a single function called *a wavelet*, which is a short length oscillating function. These elementary functions are localized in space. These properties make them good candidates to improve the flexibility and efficiency of split-step propagation methods.

The Fourier transform decomposes a signal on periodic functions with different frequencies. However, if we are interested in a localized phenomenon, its use is less suitable. The periodicity and non localized energy prevent from analyzing any local property of the signal in the spectral domain.

To overcome these disadvantages, the Gabor [48] and wavelet transforms [61] have been developed. Gabor defines elementary space-frequency wavelike atoms to achieve localization properties. In addition, Gabor uses simple basic functions that are classically used in signal processing and wave propagation [45][48][54].

The wavelet transform has similarities with the Gabor transform. The signal is also expanded on elementary wavelike functions. It is a very efficient tool for data compression and analysis. Moreover, it has a higher computation efficiency than the Gabor decomposition and the Fourier transform.

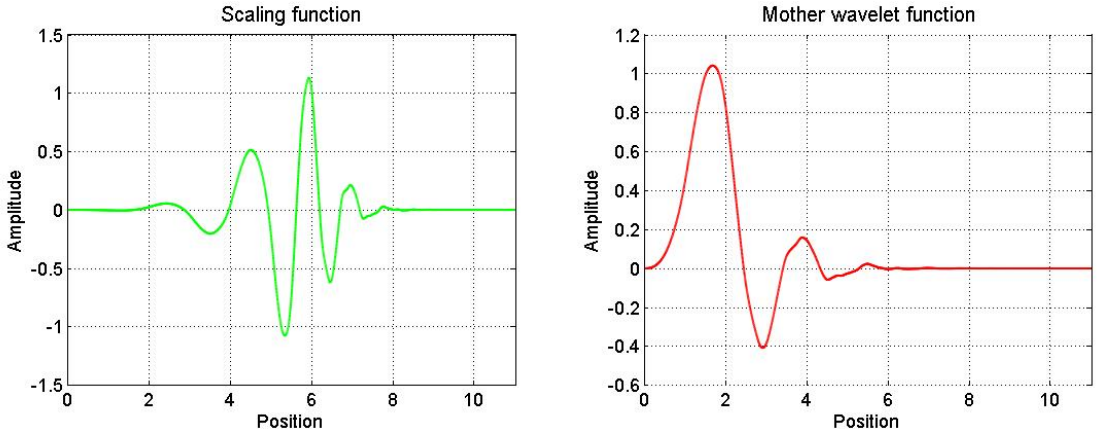

(a) Scaling function ϕ (b) Mother wavelet ψ

Figure 3.1: Scaling function ϕ and mother wavelet ψ of *Daubechies* of order 6.

As a result, in this chapter, we focus on the wavelet transforms to improve the time and memory requirements in our propagation method.

In section 3.2, the discrete wavelet transform is introduced. The multilevel analysis and fast computation method of the wavelet transform are also presented. In section 3.3, data compression applied on the wavelet coefficients is described. In section 3.4, the choice of the wavelet parameters is discussed. In section 3.5, numerical tests are performed to compare the compression results with different parameters.

3.2 Wavelet transforms

The objective is to expand a field on elementary functions localized both in the spatial and spectral domains. The discrete wavelet transform, the fast wavelet transform, and data compression are introduced in this section.

3.2.1 Discrete wavelet transform

The discrete wavelet transform (DWT) leads to a representation of a discrete function as a linear combination of elementary functions. These elementary functions form an orthonormal basis. They are obtained by dilations and translations of a scaling function ϕ and a mother wavelet function ψ [89]. An example of scaling function ϕ and mother wavelet function ψ for *Daubechies* wavelets of order 6 is plotted in Fig. 3.1. They provide a source to generate the scaled and translated scaling functions $\phi_{l,p}$ and wavelets $\psi_{l,p}$ which are scaled by 2^l with $l \in \mathbb{Z}$ and translated by p with $p \in \mathbb{Z}$. Thus, the scaling functions are

$$\phi_{l,p}[\cdot] = 2^{-l/2}\phi[2^{-l} \cdot -p], \tag{3.1}$$

and the wavelets are

$$\psi_{l,p}[\cdot] = 2^{-l/2}\psi[2^{-l}\cdot - p]. \tag{3.2}$$

As proven by Mallat [89], for any $L \in \mathbb{Z}$, $(\phi_{L,p})_{p\in\mathbb{Z}}$ and $(\psi_{l,p})_{p\in\mathbb{Z},l\in[1,L]}$ form an orthonormal basis of $\mathbf{I}^2(\mathbb{Z})$, which is the space of the finite energy discrete functions. A discrete function u can thus be represented as a sum of an approximation component u_a associated with the scaling function and a multiresolution detail component u_d associated with the dilated wavelets functions. The L-level multiresolution representation is given by

$$\begin{aligned} u[\cdot] &= u_a[\cdot] + u_d[\cdot] \\ &= \sum_{p\in\mathbb{Z}} a_{L,p}\phi_{L,p}[\cdot] + \sum_{l=1}^{L}\sum_{p\in\mathbb{Z}} d_{l,p}\psi_{l,p}[\cdot] \\ &= \sum_{p\in\mathbb{Z}} a_{L,p}2^{-L/2}\phi[2^{-L}\cdot - p] + \sum_{l=1}^{L}\sum_{p\in\mathbb{Z}} d_{l,p}2^{-l/2}\psi[2^{-l}\cdot - p], \end{aligned} \tag{3.3}$$

where $a_{L,p}$ are called the approximation coefficients and $d_{l,p}$, with $l \in [1, L]$, are called the detail coefficients.

Note here that the previous formulations are given for an infinite domain. Due to the finite size of the domain along z, for each level l, the p-indices are here limited to $[0, N_l - 1]$ with $N_l = N_z/2^l$. The total number of coefficients is N_z. For the sake of clarity, in the following, the coefficients are represented by a vector U of dimension N_z. The double index (l, p) is used to represent the elements of U, such that

$$U_{(l,p)} = \begin{cases} a_{L,p} & \text{for} \quad l = 0, p \in [0, N_L - 1], \\ d_{l,p} & \text{for} \quad l \in [1, L], p \in [0, N_l - 1]. \end{cases} \tag{3.4}$$

Besides, for the sake of conciseness, scaling functions and wavelets are both designated as *wavelets* hereafter. Thus, the representation is expressed by

$$u[\cdot] = \sum_{l=0}^{L}\sum_{p} U_{(l,p)}\chi_{l,p}[\cdot], \tag{3.5}$$

with

$$\chi_{l,p}[\cdot] = \begin{cases} \phi_{L,p}[\cdot] & \text{for} \quad l = 0, \\ \psi_{l,p}[\cdot] & \text{for} \quad l \in [1, L]. \end{cases} \tag{3.6}$$

Because of the orthogonality of the basis, these coefficients can be calculated as the inner products of u and the basis elements.

In practice, the inner products are not computed. The coefficients are obtained with the FWT algorithm introduced in next subsection that has a better computation efficiency.

3.2.2 Fast wavelet transform

Mallat [62] has proven that any pair of scaling and wavelet functions ϕ and ψ are specified by 2 conjugate mirror filters. Their corresponding impulse response sequences h and g are such that

$$\begin{aligned}\phi[\cdot] &= \sqrt{2}\sum_{p\in\mathbb{Z}} h_p \phi[2\cdot - p],\\ \psi[\cdot] &= \sqrt{2}\sum_{p\in\mathbb{Z}} g_p \psi[2\cdot - p],\end{aligned} \tag{3.7}$$

where h_p and g_p are the elements of the sequences h and p.

For the wavelet decomposition, this leads to an iterative relation between 2 levels of approximation-detail coefficients, given by

$$\begin{aligned}a_{l+1,p} &= \sum_{n\in\mathbb{Z}} h_{n-2p} a_{l,n} = \left(a_l * \bar{h}\right)_{2p},\\ d_{l+1,p} &= \sum_{n\in\mathbb{Z}} g_{n-2p} a_{l,n} = \left(a_l * \bar{g}\right)_{2p},\end{aligned} \tag{3.8}$$

where $a_l = \{a_{l,p}\}_{p\in\mathbb{Z}}$, $d_l = \{d_{l,p}\}_{p\in\mathbb{Z}}$, $\bar{h}_p = h_{-p}$, and $\bar{g}_p = g_{-p}$.

As an initialization, the approximation coefficient a_0 corresponds to the discrete function u. Then, for $l \in [1, L-1]$, a_{l+1} and d_{l+1} are obtained by taking the convolution of a_l with $\bar{h}$ and $\bar{g}$ followed by a factor 2 subsampling, as illustrated in Fig 3.2a.

For the wavelet reconstruction (denoted as *inverse FWT*, IFWT), we have the relation

$$\begin{aligned}a_{l,p} &= \sum_{n\in\mathbb{Z}} h_{p-2n} a_{l+1,n} + \sum_{n\in\mathbb{Z}} g_{p-2n} d_{l+1,n}\\ &= \left(\hat{a}_{l+1} * h\right)_p + \left(\hat{d}_{l+1} * g\right)_p,\end{aligned} \tag{3.9}$$

where the hat symbol denotes a factor 2 upsampling before the convolution. Therefore, for $l \in \{L-1, L-2, \cdots, 1\}$, the reconstruction is an interpolation that inserts zeros to expand a_{l+1} and d_{l+1}, then filters these signals by h and g, as illustrated in Fig 3.2b. Finally, a_0 is obtained, which is the reconstructed discrete function u.

This algorithm is more efficient than DWT because coefficients are computed level by level rather than computing the inner products. The complexity of FWT is $O(N_z)$ [62]. This is faster than FFT for which the complexity is $O(N_z \log_2 N_z)$ [90].

3.3 Data compression

One of the most important applications of the wavelet transform is data compression. For each level, thresholding can be applied to the coefficients. It is realized by forcing to 0 the coefficients that are close to zero. The element of the compressed coefficients $\tilde{U}$ is

$$\tilde{U}_{(l,p)} = \begin{cases} 0 & \text{for} \quad |U_{(l,p)}| \le V_s,\\ U_{(l,p)} & \text{for} \quad |U_{(l,p)}| > V_s,\end{cases} \tag{3.10}$$

with V_s the threshold. $\tilde{U}$ is generally a sparse vector.

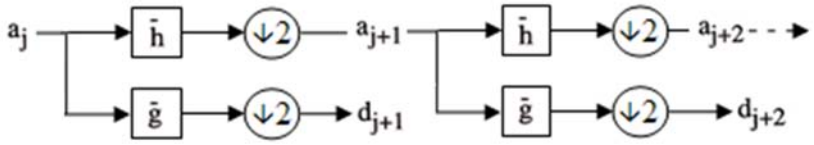

(a) FWT is computed with a cascade of filtering with $\bar{h}$ and $\bar{g}$ followed by a factor 2 subsampling.

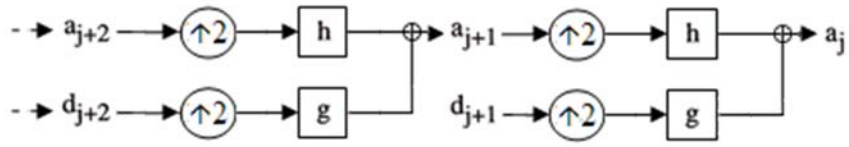

(b) Inverse FWT iteratively reconstructs progressively each a_l by inserting zeros between samples of a_{l+1} and d_{l+1}, filtering and adding the outputs.

Figure 3.2: Fast wavelet transforms [12].

After compression, the number of non-zero coefficients N_c is typically much smaller than the original size of the signal N_z. Thus, this signal is approximated by a sparse set of coefficients. As the basis is orthonormal, the energy of the signal corresponds to the wavelet coefficients by $\|u\|_2^2 = \sum_{l,p} |U_{(l,p)}|^2$. Hence, the accuracy of the approximation depends on the threshold and the error is approximately of $\mathscr{E} = 20 \log V_\mathrm{s}$. For instance, a threshold $V_\mathrm{s} = 10^{-2}$ yields a -40 dB accuracy.

3.4 Choice of the wavelet parameters

We have presented the wavelet decomposition where elementary functions are dilations and translations of a scaling function and a mother wavelet. The choice of the mother wavelet is here justified. In this section, we present the main parameters and the most common wavelets for DWT.

3.4.1 Introduction of the main wavelet parameters

3.4.1.a Vanishing moments and size of support

A wavelet ψ is characterized by the number of its vanishing moments n_v. We say the wavelet function ψ has n_v vanishing moments if

$$\int_{-\infty}^{\infty} x^s \psi(x) dx = 0, \quad \text{for} \quad 0 \leq s < n_\mathrm{v}. \tag{3.11}$$

If n_v is large, the coefficients are small at fine scales [62]. Thus, a great n_v is chosen to obtain a sparser set of coefficients.

A wavelet has a compact support if it is zero outside of a compact set. The common wavelets used in DWT are *Daubechies*, *symlets*, and *coiflets*. As an example, the scaling

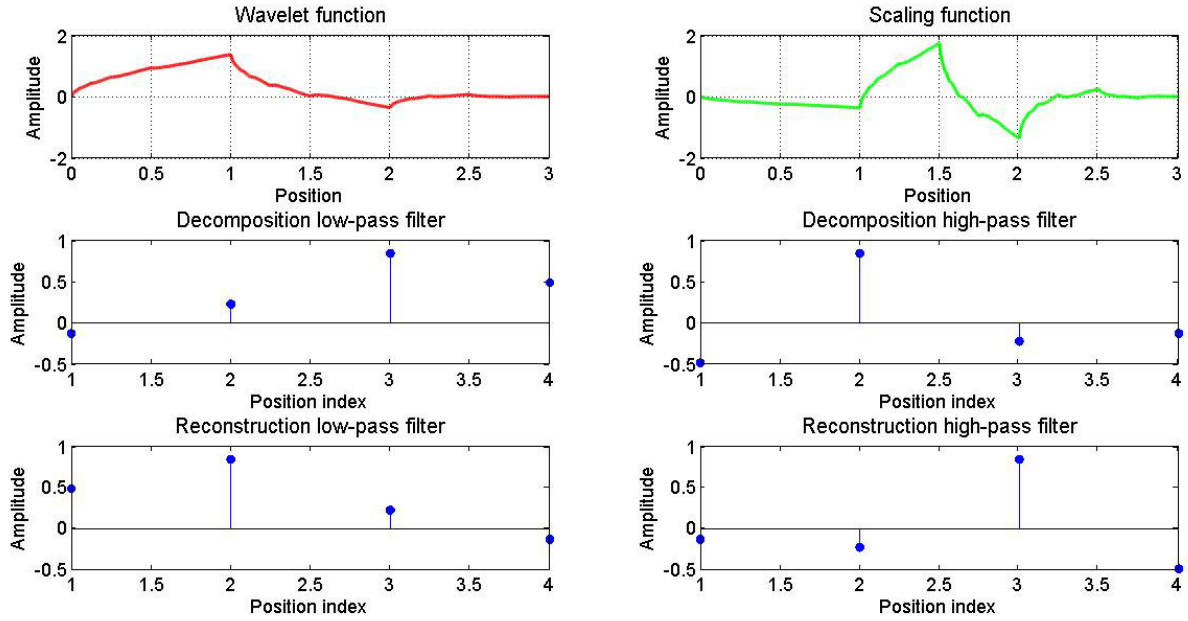

Figure 3.3: Scaling function, mother wavelet, and conjugate mirror filters for *Daubechies* wavelets of order 2.

function, mother wavelet, and the conjugate mirror filters of *Daubechies* of order $\tau = 2$ are plotted in Fig. 3.3. We can see that the scaling function, the mother wavelet, and the conjugate mirror filters all have a compact support.

There is a compromise between the support size and n_{v}. Because of the constraint on orthogonality, if a wavelet basis have n_{v} vanishing moments, its support is at least $2n_{\mathrm{v}} - 1$ [62].

3.4.1.b Regularity and symmetry

When a compression is applied on a signal, an error is added to the reconstructed signal. When the wavelet basis has a greater regularity, this error is smoother. For our applications, smoother error has less impact on the spectrum of the signal, which is used to propagate the wavelets.

Besides, for propagation, it is better to choose a more symmetric wavelet to keep the same level of accuracy on both sides of the signal.

3.4.2 Common orthogonal and compactly supported wavelet types

We choose an orthogonal and compactly supported wavelet for DWT. The common wavelet families are *Daubechies*, *symlets*, and *coiflets* [62].

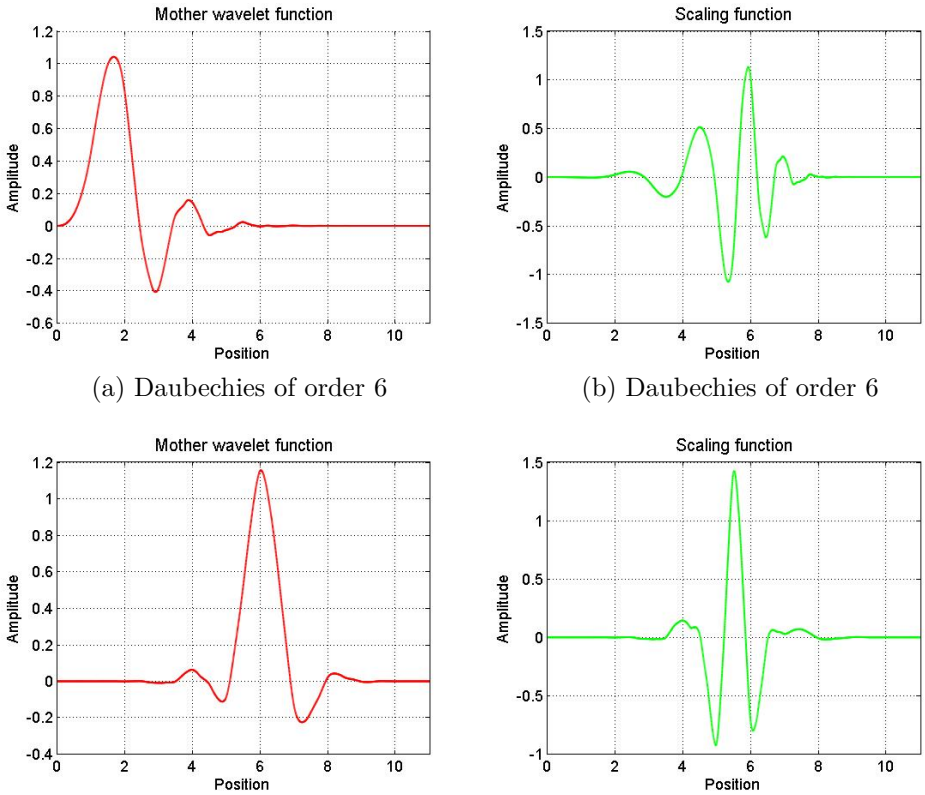

(a) Daubechies of order 6

(b) Daubechies of order 6

(c) Symlets of order 6

(d) Symlets of order 6

Figure 3.4: Daubechies and symlets wavelets ψ and scaling functions ϕ of order 6.

3.4.2.a Daubechies wavelets

For Daubechies wavelets of order τ, the number of vanishing moments is $n_{\mathrm{v}} = \tau$, as indicated in Table 3.1. Daubechies wavelets have a support of minimum size $2n_{\mathrm{v}} - 1$ for any given number n_{v} of vanishing moments [62]. The support of the wavelet is $[-n_{\mathrm{v}}+1, n_{\mathrm{v}}]$ and the support of the scaling function is $[0, 2n_{\mathrm{v}}]$.

The mother wavelet and the scaling function of the Daubechies wavelet of order $\tau = 6$ are illustrated in Fig. 3.4a and Fig. 3.4b. We can see that they are not symmetric. Indeed, the Daubechies wavelets are known to be very asymmetric by construction [62].

3.4.2.b Symlets wavelets

The symlets wavelets are a modified version of Daubechies wavelets with increased symmetry. The Daubechies and symlets wavelets of the same order have the same vanishing moment and support width.

The mother wavelet and the scaling function of the symlets wavelet of order 6 are illustrated in Fig. 3.4c and Fig. 3.4d. We can see that the symlets wavelets are more symmetric than the Daubechies wavelet.

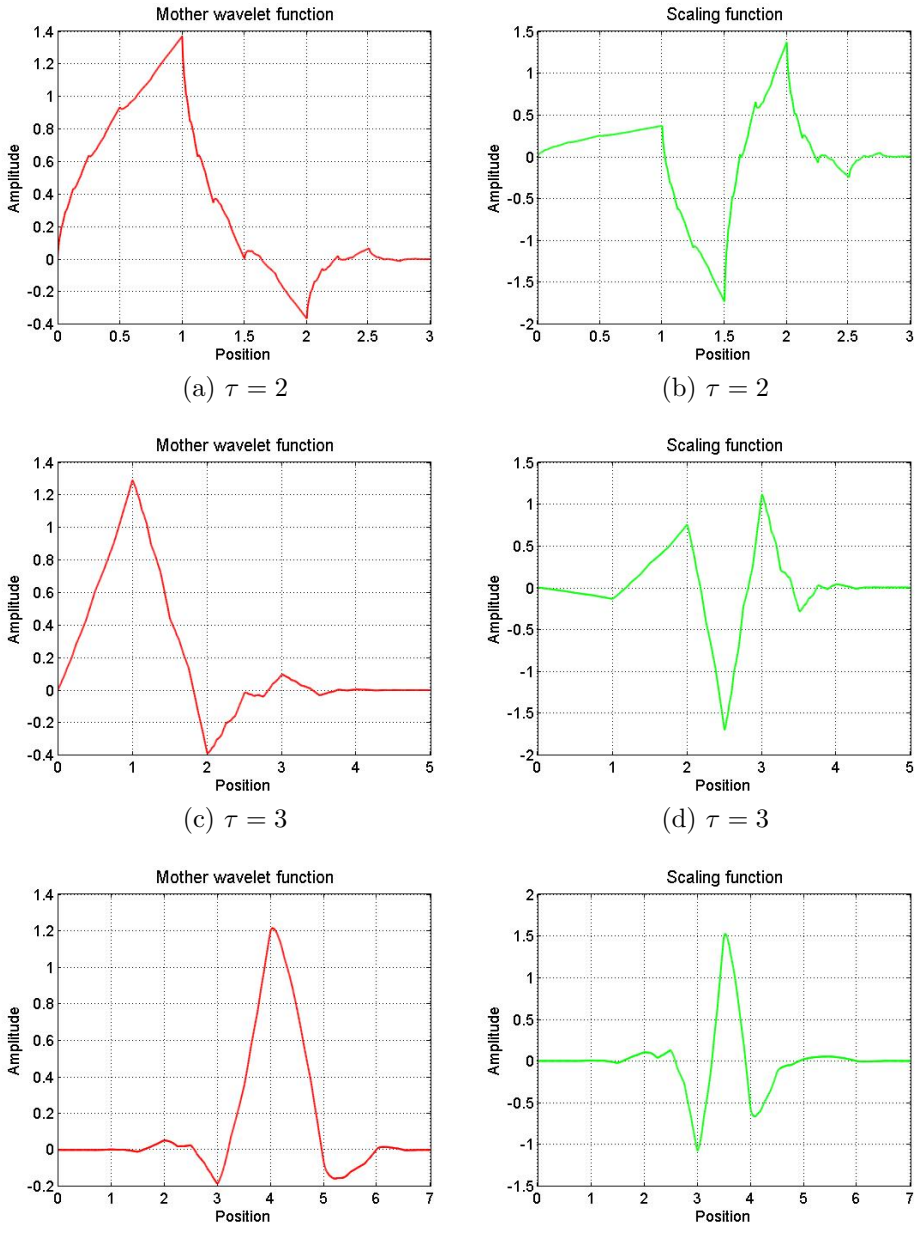

(a) $\tau = 2$ (b) $\tau = 2$

(c) $\tau = 3$ (d) $\tau = 3$

(e) $\tau = 4$ (f) $\tau = 4$

Figure 3.5: Symlets mother wavelet ψ and scaling function ϕ of order τ.

wavelet basis (order τ)	Daubechies	symlets	coiflets
support width	$2\tau - 1$	$2\tau - 1$	$6\tau - 1$
number of vanishing moments n_v for ψ	τ	τ	2τ
symmetric	far from	nearly	nearly

Table 3.1: Properties of common orthogonal compact-support wavelet families of order τ.

Symlets wavelet ψ and scaling function ϕ with n_v vanishing moments are plotted in Fig. 3.5. With a higher order, ψ and ϕ become more symmetric and smooth.

3.4.2.c Coiflets wavelets

Coiflets wavelets are compactly supported wavelets with the highest number of vanishing moments for both ϕ and ψ for a given support width. The drawback is that it has a larger support compared to the two previous wavelets.

3.4.2.d Summarize of the properties

The properties of the three wavelet families are summarized in Table 3.1. *Daubechies* and *symlets* wavelets have a minimum support size of mother wavelet or scaling function for a given number of vanishing moments. In general, the wavelet regularity increases with the number of vanishing moments [62]. Moreover, *symlets* and *coiflets* are more symmetric than *Daubechies*.

3.5 Tests of wavelet decomposition and compression of an electromagnetic field

We have presented the main parameters and the most common wavelets for FWT. In this section, numerical tests are performed. FWT and compression are applied and parametric studies on the wavelet type, the order τ, the maximum decomposition level L, and the compression threshold V_s are performed. The compression rate and accuracy are compared. Finally, the compression rate (CR) is defined by

$$\mathrm{CR} = \frac{\text{Number of zeros}}{\text{Total number of coefficients}}. \tag{3.12}$$

The computation time of FWT is compared to FFT to show its advantage.

3.5.1 Tests on the wavelet types

Tests with different wavelet families are performed for compressing the fields radiated from a complex source point or a uniform aperture.

wavelet families	Daubechies	symlets	coiflets
number of non-zero coefficients	36	37	34
CR (%)	98.2	98.2	98.3
RMSE (dB)	−63.0	−64.2	−65.8

Table 3.2: Compression of the field radiated from a CSP with $V_s = 10^{-3}$ and $L = 3$ for three wavelet families.

3.5.1.a Complex source point

A 2D complex source point (see section 1.8.2.a) is considered with a frequency $f_0 =$ 300 MHz, $r_{w0} = -50$ m, $y_s = 0$ m, $z_s = 1000$ m, and $W_0 = 5$ m. This field is sampled on $N_z = 2048$ points with $\Delta z = 1$ m.

In the first test, we fix $L = 3$ and the vanishing moment $n_{\mathrm{v}} = 5$. We test and compare three types of wavelet families *Daubechies*, *symlets*, and *coiflets*. The compression threshold on the signal is $V_s = 10^{-3}$.

After FWT and signal compression, the number of non-zero coefficients, compression rate (CR), and RMSE (dB) between initial and compressed fields are summarized in Table 3.2. The CR and RMSE are almost the same with the three types of wavelets. Moreover, the RMSE meets with the threshold V_s, which is −60 dB.

The compressed coefficients and fields with different wavelet families are plotted in Fig. 3.6. The compressed coefficients with symlets 5 are more symmetric. The position of the maximum coefficient is the same as the maximum field. This is due to the symmetry property of the symlets wavelets. In the other cases, a bias between the positions of the maximum coefficient and the maximum field is obvious. Thus, symlets seem to be the best choice.

3.5.1.b Uniform aperture

A uniform aperture (see section 1.8.2.b) is considered with $a = 5$ m, $r_s = 0$ m and $z_s = 1000$ m. The field discontinues occur at the limits of the aperture. Comparisons of the results using different wavelet families are performed. The other parameters are the same in the previous test.

After compression, the number of non-zero coefficients, CR, and RMSE (dB) between the initial and compressed fields are summarized in Table 3.3. These results are almost the same in the 3 cases.

The coefficients and fields after compression with different wavelet families are plotted in Fig. 3.7. The error is negligible in all the tests. The compression is successfully tested for the signal with strong variations.

In these tests, we have compared the results with three common wavelets families. The field can be represented by a few coefficients with a very high compression rate. The

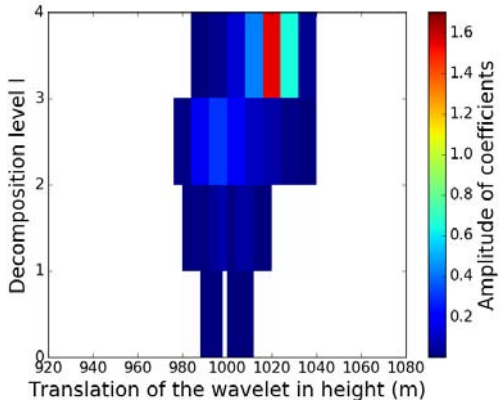

(a) Daubechies of order 5, compressed coefficients

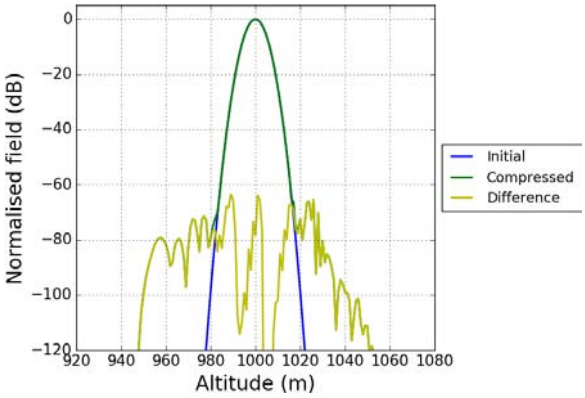

(b) Daubechies of order 5, compressed field

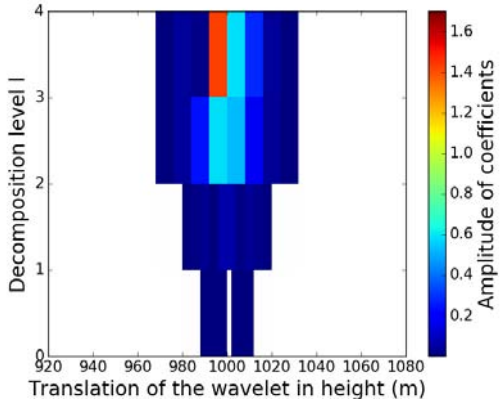

(c) Symlets of order 5, compressed coefficients

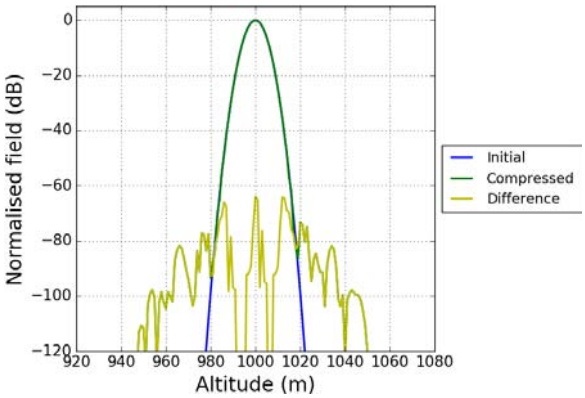

(d) Symlets of order 5, compressed field

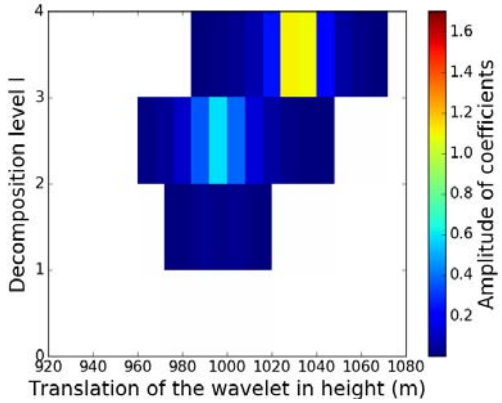

(e) Coiflets of order 5, compressed coefficients

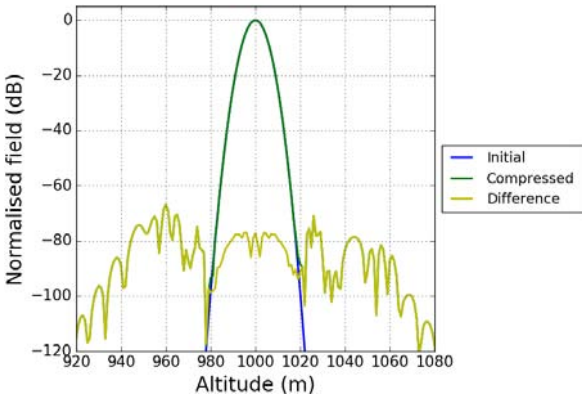

(f) Coiflets of order 5, compressed field

Figure 3.6: Wavelet decomposition and compression of the field radiated from a CSP with different wavelet families.

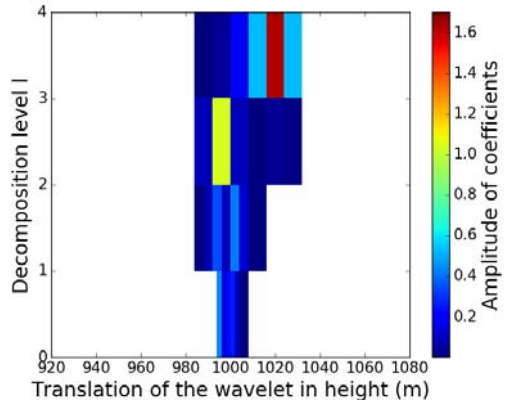

(a) Daubechies of order 5, compressed coefficients

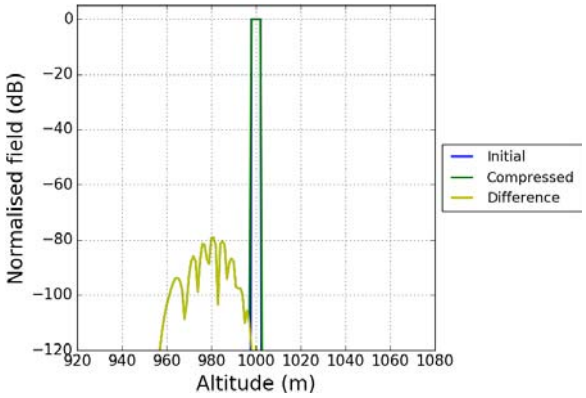

(b) Daubechies of order 5, compressed field

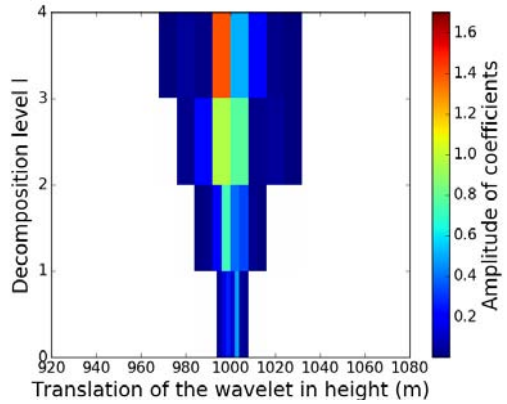

(c) Symlets of order 5, compressed coefficients

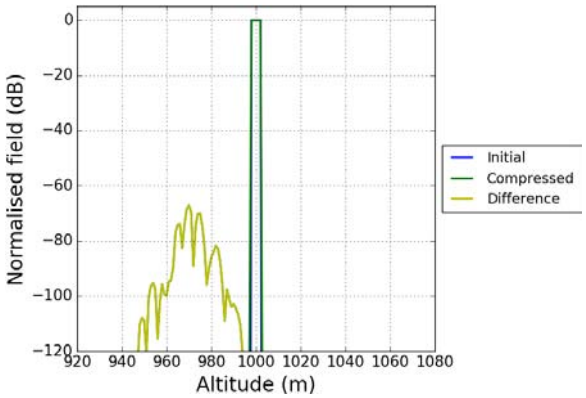

(d) Symlets of order 5, compressed field

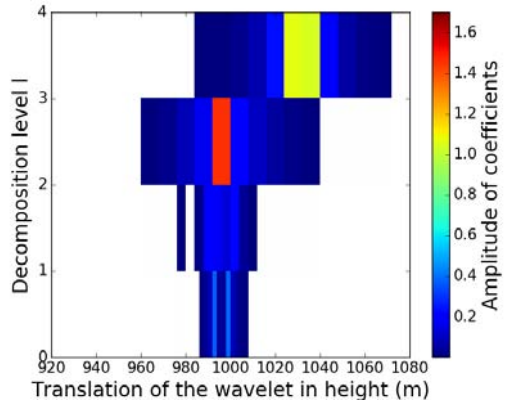

(e) Coiflets of order 5, compressed coefficients

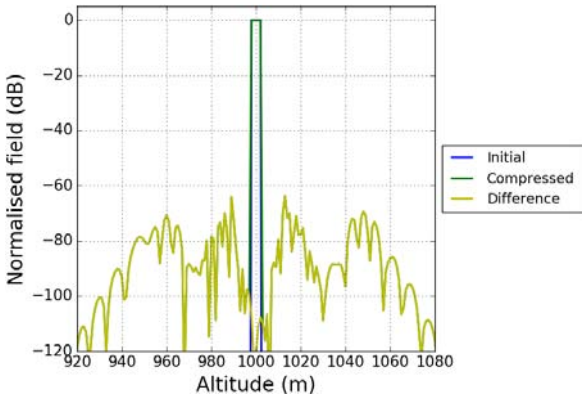

(f) Coiflets of order 5, compressed field

Figure 3.7: Wavelet decomposition and compression of the field radiated from a uniform aperture with different wavelet families.

wavelet families	Daubechies	symlets	coiflets
number of non-zero coefficients	27	30	40
CR (%)	98.7	98.5	98.0
RMSE (dB)	−77.7	−67.5	−62.6

Table 3.3: Compression of the field radiated from a uniform aperture with $V_s = 10^{-3}$ and $L = 3$ for three wavelet families.

difference of results for the three wavelet families is not obvious. In the following tests, all the simulations are realized using *symlets*.

3.5.2 Tests on the order for symlets

In this section, tests of compression are performed using *symlets* wavelets with different orders τ.

3.5.2.a Complex source point

The source and parameters of the simulation are the same as in section 3.5.1.a.

We fix $r_{w0} = -50$ m. The widths $W_0 = 3$ m and $W_0 = 10$ m are tested. The fields at $r_0 = 0$ m are shown in Fig. 3.8a and Fig. 3.8b.

A compression with $V_s = 10^{-3}$ is performed. The compression results are summarized in Tables 3.4 and 3.5. In the case $W_0 = 3$ m, the CR and RMSE with small τ are slightly better. On the contrary, with $W_0 = 10$ m, a greater order τ corresponds to a better CR. No clear tendency is observed on the RMSE.

Then, a test with a CSP of width $W_0 = 3$ m and $r_{w0} = -500$ m is performed. The field is illustrated in Fig. 3.8c. The aim is to compare the result for the same source but translated. The compression results are summarized in Table 3.6. A greater τ corresponds to a better CR, however the difference is not obvious. The RMSE are almost the same with different τ.

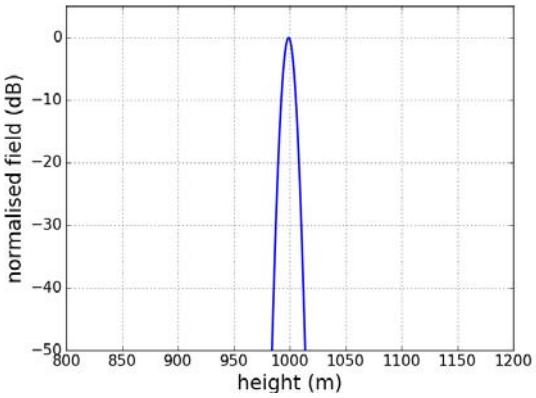

(a) $W_0 = 3$ m, $r_{w0} = -50$ m

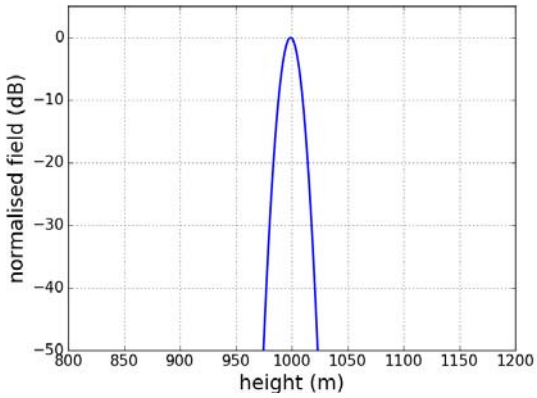

(b) $W_0 = 10$ m, $r_{w0} = -50$ m

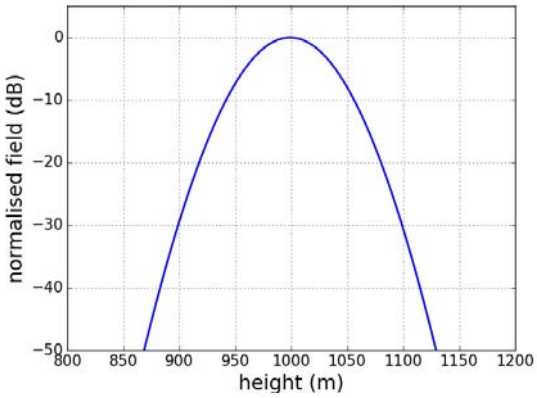

(c) $W_0 = 3$ m, $r_{w0} = -500$ m

Figure 3.8: Fields radiated from CSP with different W_0 and r_{w0}.

order τ	2	3	4	5	6	7	8
number of non-zero coefficients	38	38	42	43	46	45	48
CR (%)	98.1	98.1	97.9	97.9	97.8	97.8	97.6
RMSE (dB)	−73.3	−66.1	−68.5	−67.0	−68.4	−64.6	−67.8

Table 3.4: Compression of the field radiated from a CSP of width $W_0 = 3$ m and $r_{w0} = -50$ m with respect to the order τ.

order τ	2	3	4	5	6	7	8
number of non-zero coefficients	51	38	30	27	25	23	20
CR (%)	97.5	98.1	98.5	98.7	98.8	98.9	99
RMSE (dB)	−67.6	−63.7	−66.1	−67.3	−65.6	−64.1	−64.7

Table 3.5: Compression of the field radiated from a CSP of width $W_0 = 10$ and $r_{w0} = -50$ m with respect to the order τ.

order τ	2	3	4	5	6	7	8
number of non-zero coefficients	276	272	261	250	245	236	228
CR (%)	86.5	86.7	87.3	87.8	88.0	88.5	88.9
RMSE (dB)	−68.3	−68.4	−67.4	−66.8	−67.2	−67.0	−66.9

Table 3.6: Compression of the field radiated from a CSP of width $W_0 = 3$ and $r_{w0} = -500$ m with respect to the order τ.

3.5.2.b Uniform aperture

The propagation of the field with a smooth variation radiated by a CSP has been successfully tested. Tests of compression on the fields with larger variations is now considered from the radiation of a uniform aperture.

First, the fields for apertures of widths $a = 5$ m and $a = 20$ m at distance $r = 0$ m are considered, as illustrated in Fig. 3.9a and in Fig. 3.9b. Compression is applied on the fields. The other parameters are the same as in the previous tests.

The compression results are summarized in Tables 3.7 and 3.8. In both cases, the results of CR and accuracy with small τ are slightly better. This is due to the strong variations of the field amplitude on the limits of the apertures, wavelets with smaller support (*i.e.* smaller τ) treat well this case. In addition, for the wavelets with $\tau = 2$ and $\tau = 3$, the RMSE is far below the others.

Then, the fields for apertures of widths $a = 5$ m and $a = 20$ m at distance $r = 500$ m are considered, as illustrated in Fig. 3.9c and 3.9d. Their amplitudes have the form of a cardinal sine function (see (1.83)).

The compression results are summarized in Tables 3.9 and 3.10. Contrary to the cases $r = 0$ m, after propagation on 500 m, compression with higher τ leads to better CR and RMSE.

In these tests, we have compared the results with different orders τ. Comparisons of the

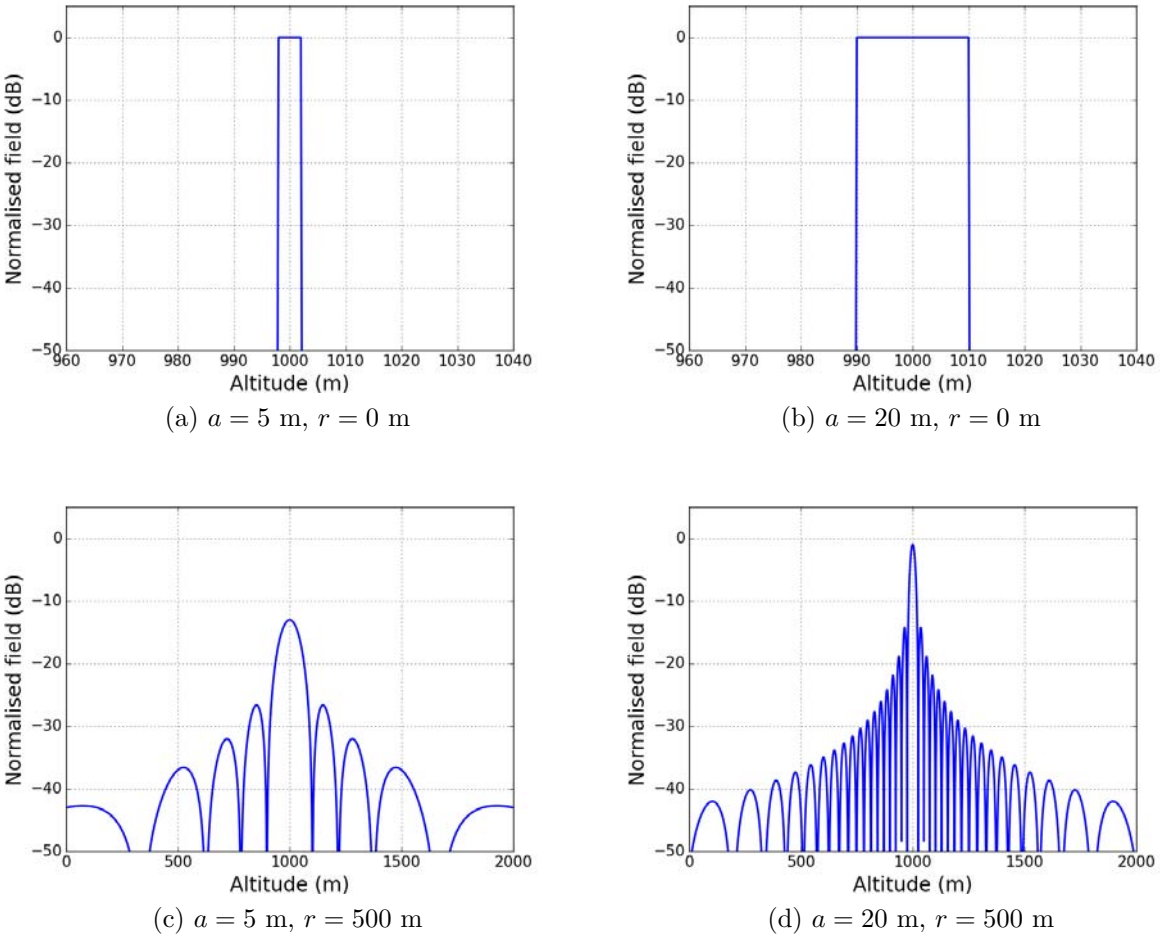

(a) $a = 5$ m, $r = 0$ m

(b) $a = 20$ m, $r = 0$ m

(c) $a = 5$ m, $r = 500$ m

(d) $a = 20$ m, $r = 500$ m

Figure 3.9: Fields at distance r, radiated from a uniform aperture of different width a.

order τ	2	3	4	5	6	7	8
number of non-zero coefficients	15	20	22	30	30	33	34
CR (%)	99.3	99.0	98.9	98.5	98.5	98.4	98.3
RMSE (dB)	−237.6	−216.8	−67.9	−67.5	−71.8	−67.4	−67.6

Table 3.7: Compression of the fields radiated from a uniform aperture of width $a = 5$ m at $r = 0$ m with respect to order τ.

order τ	2	3	4	5	6	7	8
number of non-zero coefficients	20	26	30	40	41	45	47
CR (%)	99.0	98.7	98.5	98.0	98.0	97.8	97.7
RMSE (dB)	−244.3	−220.5	−72.8	−73.6	−82.0	−73.3	−77.1

Table 3.8: Compression of the fields radiated from a uniform aperture of width $a = 20$ m at $r = 0$ m with respect to order τ.

order τ	2	3	4	5	6	7	8
number of non-zero coefficients	261	253	253	254	252	250	250
CR (%)	87.3	87.6	87.6	87.6	87.7	87.8	87.8
RMSE (dB)	−53.6	−65.3	−69.6	−73.4	−66.1	−63.8	−63.3

Table 3.9: Compression of the fields radiated from a uniform aperture of width $a = 5$ m at $r = 500$ m with respect to order τ.

order τ	2	3	4	5	6	7	8
number of non-zero coefficients	463	337	293	276	261	254	253
CR (%)	77.4	83.5	85.7	86.5	87.3	87.6	87.6
RMSE (dB)	−54.4	−58.3	−61.6	−63.0	−62.4	−64.8	−67.4

Table 3.10: Compression of the fields radiated from a uniform aperture of width $a = 20$ m at $r = 500$ m with respect to order τ.

compressed fields of the field radiated from a CSP and a uniform aperture at different distances have been performed. The result of CR and the RMSE depends on the shape of the field. For well-localized fields, a wavelet with a smaller τ is better. On the contrary, for the propagated fields, which are in general spread in space, a wavelet with a larger τ is better.

In the following tests, all the simulations are realized using *symlets* wavelets with $\tau = 6$ to test different values of maximum decomposition level L and thresholds.

maximum level of decomposition L	2	3	4	5
CR (%)	97.9	97.8	97.2	96.9
RMSE (dB) between initial and compressed fields	-86.7	-86.5	-87.0	-85.6

Table 3.11: Compression of the CSP with respect to L with symlets 6 and $V_s = 10^{-4}$.

value of threshold V_s	10^{-2}	10^{-3}	10^{-4}	10^{-5}
CR (%)	98.9	98.3	97.6	97.2
RMSE (dB) between initial and compressed fields	-49.6	-61.6	-86.5	-109.5

Table 3.12: Compression of the CSP with respect to V_s with symlets 6 and $L = 3$.

3.5.3 Tests on the maximum decomposition level and threshold for symlets wavelets

In this section, the tests are performed with symlets wavelets with different L and thresholds. A CSP is considered with $r_{w0} = -50$ m and $W_0 = 3$ m. The simulation parameters are the same as in the previous tests.

First, a test with different maximum decomposition levels L is performed. The threshold is $V_s = 10^{-4}$. The root mean square error (RMSE) of the compressed field to the original field and the compression rate (CR) are shown in Table 3.11. We can see that L does not have a significant influence on the accuracy of the compressed signal.

In a second step, the influence of V_s is studied for a fixed value $L = 3$. The results are shown in Table 3.12. The RMSE between the initial and compressed fields meets with the expected error $20 \log V_s$. The choice of V_s results from a compromise between accuracy and CR.

For $L = 3$, $V_s = 10^{-2}$, the coefficients after compression are shown in Fig 3.10. The number of non-zero compressed coefficients is $N_c = 22$. This confirms that the signal is represented by N_c coefficients ($N_c \ll N_z = 2048$) with a RMSE of -49.6 dB.

Furthermore, we see that the detail coefficients at level 1 are all set to zero. The signal is only represented by the coefficients of level 2 and 3. The signal is automatically described by the wavelets at appropriate dilations.

In these tests, we can see that the maximum decomposition level L does not have a significant influence on the accuracy of the compressed signal. In this thesis, all the following simulations are realized with $L = 3$. Moreover, the accuracy of the compressed fields depends on the compression threshold. The error between the initial and compressed fields meets with $20 \log V_s$.

3.5.4 Computation times of FFT and FWT

The computation times for applying FFT and FWT on a signal are compared. For this test, the sample number N_z is chosen as powers of small prime numbers so that FFT has a high efficiency. The computation time for one decomposition is shown in Fig 3.11 with

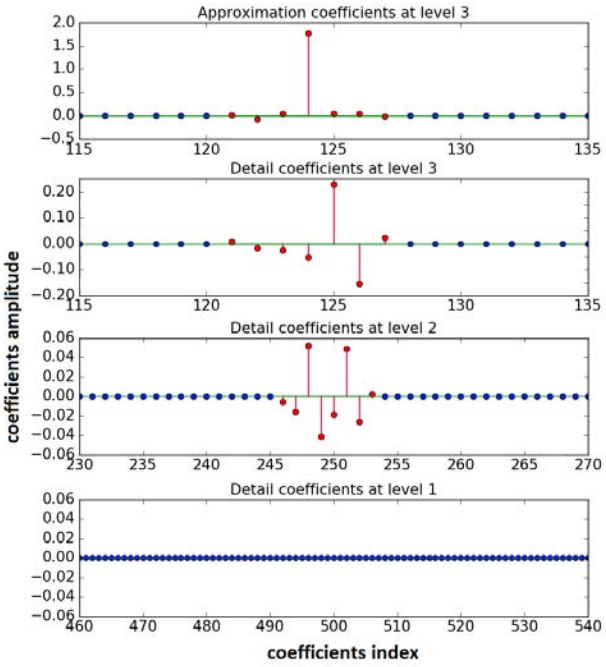

Figure 3.10: Coefficients of the wavelet decomposition. Red and blue markers correspond to the non-zero and zero coefficients, respectively.

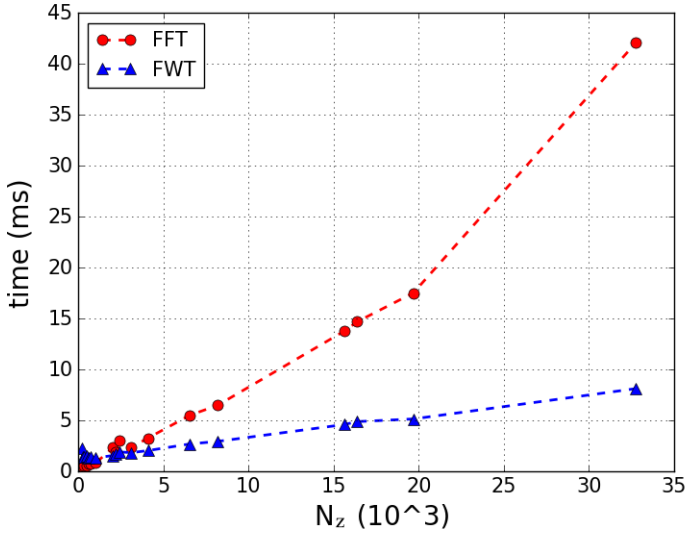

Figure 3.11: Comparison of the computation times for applying FFT and FWT on a signal sampled by N_z points.

respect to the vector length N_z. As expected, FWT is faster and the difference increases with N_z.

3.6 Conclusion

In this chapter, the discrete wavelet transform and the compression method have been introduced.

First, the discrete wavelet transform has been presented. A field is decomposed on the *wavelets* localized in the frequency domain. The wavelets are constructed by dilations and translations of a mother wavelet. The fast wavelet transform (FWT) has also been presented. The transform is realized in practice by applying conjugate filters.

Second, the data compression method has been described. It is realized by thresholding the wavelet coefficients. In this way, the field can be represented by much less coefficients.

Then, the main parameters of the wavelets have been discussed. The common wavelets used for the discrete wavelet transform have been introduced. The symlets wavelet of order 6 with the maximum decomposition level $L = 3$ is chosen for the simulations in the following chapter.

Finally, numerical tests have been performed with different parameters. The fields radiated from a complex source point (CSP) and a uniform aperture at different distances have been considered. Different parameters lead to different compression rates. The error due to compression meets with the expected value $20 \log V_s$, no matter which parameters are chosen. A comparison of the computation times of FWT with FFT has finally been performed, conforming the better efficiency of FWT.

Chapter 4

2D Split-Step Wavelet Method

4.1 Introduction

The wavelet transform and compression has been introduced in Chapter 3. Now, the objective of this chapter is to propose the use of the wavelets in split-step methods for propagation modeling.

4.1.1 State of the art

Gabor bases/frames [50][91], which are widely used in the context of modeling with Gaussian beams, are founded on a space-frequency analysis. They have been used to derive analytic formulations for electromagnetic propagation. Gabor-based beam algorithms and frame-based beam summations methods are utilized in various applications involving radiation and scattering in complex environments [91][92][52]. Atmosphere propagation methods based on the Gabor bases/frames have also been developed [93][60][94][95].

Besides, a wavelet-based algorithm has already been introduced to solve PE [63][64]. This latter, based on the scaling function expansion, has the ability to model the propagation as accurately as SSF. However, the computation complexity is the same as SSF since Fourier transforms are used at each propagation step.

4.1.2 Proposed wavelet-based method

In this chapter, we introduce an alternative method to SSF in 2D. It is also based on the split-step method. The difference is that the fast wavelet transform (FWT) [96] is used in place of FFT. It is denoted thereafter as the *split-step wavelet* (SSW) method.

In the proposed method, only wavelet transforms are used, the main purpose being to reduce the computation time. The proposed SSW method is based on the multiresolution FWT along the vertical. This results in a lower complexity than with FFT. Moreover, the wavelet decomposition efficiently yields a sparse representation of the signal. The

propagation is performed by a linear combination of the wavelets individually propagated. These individual propagations are stored as pre-computed data. The aim is to achieve a reduced computation time compared to SSF while keeping a good accuracy.

The method is here exposed in cylindrical coordinates in 2D. The formulation in Cartesian coordinates would be similar.

This chapter corresponds to the content of Zhou *et al.* [6].

4.1.3 Outline

In Section 4.2.1, the configuration and discretization are presented. In Section G.3.2, the SSW method is introduced. Domain truncation, ground condition, irregular atmosphere, and relief are also considered. Then, the computational complexities of SSW and SSF are compared. In Section G.3.7, numerical tests are performed to show the accuracy and computational efficiency of SSW.

4.2 Theoretical description of the split-step wavelet method

4.2.1 Configuration and discretization

The problem is treated with the cylindrical coordinates in 2D by assuming an invariance along θ. The aim is to simulate the propagation in a vertical plane (r, z). The source is located at $r < r_0$ and the fields $u(r, z)$ are known at $r = r_0$. The propagation is computed in the region $r \geq r_0$, $z \geq 0$. In this chapter, the TM component is considered. The TE component could be similarly propagated.

The computation domain is discretized and of finite size. The vertical domain is limited to $z \in [0, z_{\max}]$ and the range is limited to $r \in [r_0, r_{\max}]$. The following uniform grid is used:

$$\begin{aligned} r &= r_0 + p_r \Delta r \quad \text{for} \quad p_r = \{0, \ldots, N_r - 1\}, \\ z &= p_z \Delta z \quad \text{for} \quad p_z = \{0, \ldots, N_z - 1\}, \end{aligned} \tag{4.1}$$

with $N_z = z_{\max}/\Delta z$ and $N_r = (r_{\max} - r_0)/\Delta r$.

In the following parts, studies are performed in the discrete domain.

4.2.2 Introduction to the split-step wavelet method

The SSW method is based on the wavelet transform and compression introduced in chapter 3. SSW is performed going back and forth from a spatial to a wavelet representation of the wave so as to evaluate the propagation iteratively at increasing distances. The propagation from r_{p_r} to r_{p_r+1}, with $r_{p_r} = r_0 + p_r \Delta r$, is simulated step by step as follows:

1. The field $u_{p_r} = [u_{p_r,p_z}]_{p_z \in [0,N_z]}$ is represented by a sparse wavelet vector U_{p_r} after applying FWT (denoted as $\mathbf{W}$) and a compression (denoted as $\mathbf{C}$) as introduced in Chapter 3, such that
$$U_{p_r} = \mathbf{CW} u_{p_r}. \tag{4.2}$$

2. The propagation step is considered in the wavelet domain. The coefficient vector U^{p} after free-space propagation on a distance Δr is given by
$$U^{\mathrm{p}}_{p_r+1} = \mathbf{M} U_{p_r}, \tag{4.3}$$
where $\mathbf{M}$ is the pre-computed free-space propagation matrix that models the wavelet-to-wavelet propagations.

   The elements of $\mathbf{M}$, *i.e.* $M_{(l,p),(l',p')}$, satisfy
$$U^{\mathrm{p}}_{p_r+1,(l,p)} = \sum_{l',p'} M_{(l,p),(l',p')} U_{p_r,(l',p')}, \tag{4.4}$$
where (l',p') and (l,p) are the indices of the translation-dilation of the wavelets located at r_{p_r} and r_{p_r+1}, respectively.

   Details on the matrix $\mathbf{M}$ are given in Section 4.2.3.

3. The propagated field $u^{\mathrm{p}}_{p_r+1}$ is recomposed by IFWT (denoted as $\mathbf{W}^{-1}$) from the propagated wavelets
$$u^{\mathrm{p}}_{p_r+1} = \mathbf{W}^{-1} U^{\mathrm{p}}_{p_r+1}. \tag{4.5}$$

4. Apodization, atmosphere, and relief are applied in the spatial domain as in eq. (1.39), represented by the operator $\mathbf{H}$, $\mathbf{R}$, and $\mathbf{L}$, respectively.

As to conclude, the propagation from r_{p_r} to r_{p_r+1} is simulated step by step as
$$u_{p_r+1} = \mathbf{HRLW}^{-1}\mathbf{MCW} u_{p_r}. \tag{4.6}$$

4.2.3 Pre-computation of the propagation matrix M

4.2.3.a Matrix properties

In this section, we present the computation of the wavelet-to-wavelet propagation matrix $\mathbf{M}$. We take into account the translation/dilation properties of the wavelet basis so as to reduce the computation cost.

To compute $\mathbf{M}$, two steps are required. Firstly, the field corresponding to each wavelet $\chi_{l',p'}(0,\cdot)$ is propagated using SSF on one step Δr. (Any other propagation technique can be used at this step.) Secondly, the propagated wavelet $\chi_{l',p'}(\Delta r,\cdot)$ is decomposed on the wavelet basis which coefficient indices are noted (l,p). These 2 steps are as follows:

- Wavelet propagation on a distance Δr: For the first step, only one wavelet on each level l' has to be considered. Indeed, as illustrated in Fig. 4.1, the propagated wavelet $\chi_{l',p'}(\Delta r,\cdot)$ can be deduced from $\chi_{l',0}(\Delta r,\cdot)$ by means of a translation of p'.

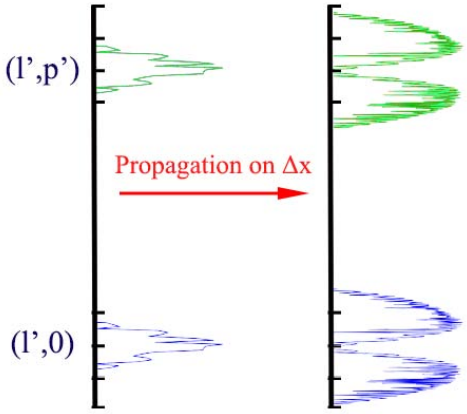

Figure 4.1: Illustration of wavelet propagations on Δr at level l'.

- Decomposition of the propagated wavelets: We now present the translation properties of $\mathbf{M}$. On that purpose, we consider a propagated wavelet $\chi_{l',p'}(\Delta r, \cdot)$ that must be decomposed on the wavelet basis.
  - For $l = l'$, the number of wavelets on the levels l and l' are the same, so a translation of 1 on p' results in a translation of 1 on p. Thus, $\mathbf{M}$ satisfies
  $$M_{(l,p+1)(l',p'+1)} = M_{(l,p)(l',p')} \quad \text{for} \quad l = l'. \tag{4.7}$$
  - For $l = l' + 1$, they are twice as many wavelets on level l' than on level l. Thus, a translation of 2 on p' results in a translation of 1 on p. Thus, we have
  $$M_{(l,p+1)(l',p'+2)} = M_{(l,p)(l',p')} \quad \text{for} \quad l = l' + 1. \tag{4.8}$$
  - For $l = l' - 1$, they are half as many wavelets on level l' than on level l. Thus, a translation of 1 on p' results in a translation of 2 on p, such that
  $$M_{(l,p+2)(l',p'+1)} = M_{(l,p)(l',p')} \quad \text{for} \quad l = l' - 1. \tag{4.9}$$
  - Finally, the rule can be generalized for any l and l' by
  $$\text{if } l \leq l', M_{(l,p+2^{l'-l})(l',p'+1)} = M_{(l,p)(l',p')}, \tag{4.10a}$$
  $$\text{if } l > l', M_{(l,p+1)(l',p'+2^{l-l'})} = M_{(l,p)(l',p')}. \tag{4.10b}$$

4.2.3.b Matrix filling

Following Section 4.2.3.a, the matrix $\mathbf{M}$ is filled. The elements $M_{(l,p)(l',0)}$ are obtained as follows:

- For each level l', the wavelet $\chi_{l',0}(0, \cdot)$ is propagated, which yields $\chi_{l',0}(\Delta r, \cdot)$.
- The FWT is applied to $\chi_{l',0}(\Delta r, \cdot)$, which leads to $M_{(l,p)(l',0)}$ for each value of l, l', and p.

Secondly, the other elements of the matrix $\mathbf{M}$ are obtained based on the previous properties. Two cases occur, as follows:

- Case $l \leq l'$:

  Using (4.10a), for all p', $M_{(l,p)(l',p')}$ can be deduced from $M_{(l,p)(l',0)}$.

- Case $l > l'$:

  For $s \in [0, 2^{l-l'}]$ and for all integer q, the propagated wavelets $\chi_{l',s}(\Delta r, \cdot)$ are deduced from $\chi_{l',0}(\Delta r, \cdot)$ by translations of s. Then $M_{(l,p)(l',s)}$ is obtained after applying a FWT to $\chi_{l',s}(\Delta r, \cdot)$. Finally, using (4.10b), $M_{(l,p+1)(l',s+2^{l-l'}q)}$ is deduced from $M_{(l,p)(l',s)}$.

Therefore, $M_{(l,p)(l',p')}$ for all (l', p') are deduced. In total, for the computation of $\mathbf{M}$, 2^L FWTs are required. The other elements in $\mathbf{M}$ are their replicas by translations.

Finally, a threshold V_{M} is applied on the coefficients of $\mathbf{M}$ to ensure its sparsity.

The pseudo code for the filling of the propagation matrix M is presented in Fig. 4.2. In the pseudo code, the cases $l = 0$ and $l' = 0$ corresponding to the scaling function are not included. Their computations are the same for the wavelet of level L. For the sake of simplicity, we have not repeated it in the pseudo code.

The method for filling the propagation matrix has been introduced. Due to the matrix properties, the operations of filling are not time consuming. In total, only $L + 1$ propagations and 2^L wavelet decompositions are needed.

4.2.4 Top boundary condition and domain truncation

In order to remove spurious reflections over the top boundary, an apodization layer with a Hanning window is applied to the field at the upper half part as presented in Section G.1.4.

4.2.5 Ground boundary condition: the local image method

In this section, we present a method peculiar to SSW to consider the ground with few additional computational effort.

4.2.5.a PEC ground condition

In SSF, if a PEC condition is applied at the ground boundary, a sine transform must be used in place of Fourier transform [12]. In SSW, a similar substitution is not possible. The classic image theory [97] could be applied. This method doubles the computation domain, an image domain being added. Furthermore, an absorbing layer should be added at the bottom of the domain. As a result, the computation burden would be significantly increased.

procedure FILLING OF THE PROPAGATION MATRIX **M**
Input:
Maximum level of decomposition L, wavelet type
for $l' \in [1, L]$ **do**
(I) Compute the wavelets $\chi_{l',0}(0,\cdot)$ using mirror filters.
(II) Propagate $\chi_{l',0}(0,\cdot)$ on Δr to obtain $\chi_{l',0}(\Delta r,\cdot)$.
(III) Obtain $M_{(l,p)(l',0)}$ by applying the FWT to $\chi_{l',0}(\Delta r,\cdot)$.
for $l \in [1, L]$ **do**
if $l \leq l'$ **then**
for $p' \in [0, N_p(l)]$ **do**
Translate $M_{(\cdot,\cdot)(l',p')}$ to obtain $M_{(\cdot,\cdot)(l',0)}$.
if $l > l'$ **then**
for $q \in [0, 2^{l-l'}[$ **do**
(i) Translate $\chi_{l',0}(\Delta r,\cdot)$ to obtain $\chi_{l',q}(\Delta r,\cdot)$.
(ii) Obtain $M_{(\cdot,\cdot)(l',q)}$ by applying the FWT on $\chi_{l',q}(\Delta r,\cdot)$.
(iii) Fill **M** by translations.
return M

Figure 4.2: Filling of the propagation matrix **M**.

To overcome this, we introduce a local image algorithm. It has a thinner image layer than with the classic image theory. The key idea is that the field in a thin image layer is updated by symmetry at each propagation step.

A PEC boundary condition is applied by following these steps:

1. At range r_{p_r}, we know the field u described on N_z points. Then it is extended to u_{t} by adding a local image layer under u on N_{im} points. The choice of N_{im} is discussed later. In this layer, the field is an image of the upper part. The whole field u^{t} is defined by

$$u^{\mathrm{t}}_{p_r,p_z} = \begin{cases} u_{p_r,p_z} & \text{for } p_z \in [1, N_z - 1], \\ 0 & \text{for } p_z = 0, \\ -u_{p_r,-p_z} & \text{for } p_z \in [-N_{\mathrm{im}}, -1]. \end{cases} \tag{4.11}$$

2. u^{t} is propagated from r_{p_r} to r_{p_r+1} by using the SSW method.

3. The field $u^{\mathrm{p}}_{p_r+1}$ is obtained as

$$u^{\mathrm{p}}_{p_r+1,p_z} = u^{\mathrm{t}}_{p_r+1,p_z}, \tag{4.12}$$

for $p_z \in [1, N_z - 1]$.

The previous algorithm is repeated at each step. As only the image of the field in the close vicinity of the ground is used, we call this algorithm *the local image method*.

At the bottom of the image layer, no apodization is applied. Therefore, an error appears at the bottom of the domain due to the boundary. However, N_{im} is chosen so that this

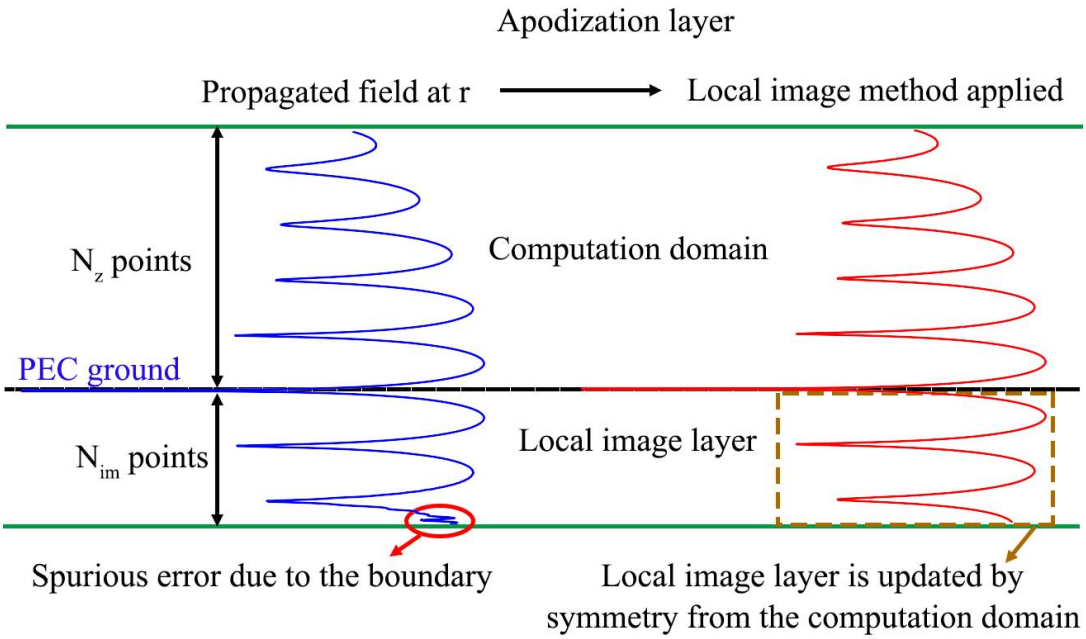

Figure 4.3: Local image method in SSW.

error does not reach the domain of interest (*i.e.*, $p_z > 0$). Indeed, at each step, the field in the image layer is updated using (G.38). Thus, the error in the image layer is cleared up at each step and never reaches $p_z > 0$, as illustrated in Fig. 4.3.

N_{im} is chosen greater than the maximum width of the wavelets after propagation on Δr. This width is known beforehand when creating the matrix $\mathbf{M}$. As the widening of one wavelet on one step Δr is much smaller than the total computation domain, $N_{\text{im}} \ll N_z$. This makes the local image method computationally efficient.

4.2.5.b Impedance ground condition

The method can be extended to simulate the propagation over a dielectric ground. It is approximated by the Leontovich impedance ground condition, as presented in Section 1.7.1.a.

Following (1.68), a variable substitution is used. The scheme is as follows:

1. Start with the solution $u_{p_r} = [u_{p_r,0}, \ldots, u_{p_r,N_z}]$ at range r_{p_r}.
2. Compute $w_{p_r} = [w_{p_r,1}, \ldots, w_{p_r,N_z-1}]$, such that

$$w_{p_r,p_z} = \frac{u_{p_r,p_z+1} - u_{p_r,p_z-1}}{2\Delta z} + \alpha u_{p_r,p_z}, \tag{4.13}$$

for $p_z = \{1, \ldots, N_z - 1\}$. w_{p_r} fulfills the Dirichlet boundary condition.

3. Propagate w_{p_r} from r_{p_r} to r_{p_r+1} using the SSW method as introduced before. A local image layer is added here. As a result, w_{p_r+1} is obtained. The ground wave is propagated as in Section 1.7.3.c.

4. Retrieve u_{p_r+1} from w_{p_r+1} as described for the DMFT algorithm (see Appendix D).

With this scheme, we can simulate the propagation over an impedance ground using the local image theory.

4.2.6 Atmosphere and relief

To consider a slowly varying atmosphere, the phase screen method (see Section 1.3.4) is applied to the field.

Irregular relief is considered by using a staircase model exactly as for SSF (see Section G.1.7).

4.2.7 Complexity comparison

Compared to the classical SSF method, the Fourier transform is replaced by the wavelet decomposition and recomposition. At each range step, the complexity of FFT is $O(N_z \log N_z)$, and the complexity of FWT is $O(N_z + N_{\text{im}}) \approx O(N_z)$ because $N_{\text{im}} \ll N_z$.

The computation complexity of the propagation step in SSF is $O(N_z)$. The propagation in SSW follows (G.34). Since $\mathbf{M}$ and U are sparse. The effective multiplication cost N_{e} is

$$\begin{aligned} N_{\text{e}} &= \sum_{(l,p)\in\mathcal{I}_{\text{nz}}(U)} \mathcal{N}_{\text{nz}}\left(M_{(l,p),(\cdot,\cdot)}\right) \\ &\leq \underbrace{\max_{(l,p)}\left(\mathcal{N}_{\text{nz}}\left(M_{(l,p),(\cdot,\cdot)}\right)\right)}_{N_M} \underbrace{\mathcal{N}_{\text{nz}}(U)}_{N_{\text{s}}}, \end{aligned} \tag{4.14}$$

where $\mathcal{I}_{\text{nz}}$ and $\mathcal{N}_{\text{nz}}$ give the indices and the number of non-zero coefficients in a vector, respectively. N_M is the maximum number of nonzero coefficients in each column of the matrix $\mathbf{M}$.

The complexity of this step in SSW is $O(N_{\text{e}})$ with $N_{\text{e}} \leq N_M N_{\text{s}}$. Note that, N_M and N_s are much smaller than N_z due to the high compression rate of the wavelet decomposition. Thus, $N_{\text{e}} \ll N_z^2$ and N_{e} largely depends on the compression rates on the propagation matrix and the signal. Simulations will show that N_{e} can even be of order N_z.

The comparison of the computation complexities of SSW and SSF for one step is shown in Table G.1. With a high compression rate (CR), SSW is faster than SSF. As the complexities of the algorithms are linear with N_r, the total complexities are obtained by multiplying by N_r.

	SSW	SSF
wavelet dec. / DFT	$O(N_z)$	$O(N_z \log N_z)$
propagation	$O(N_\mathrm{e})$	$O(N_z)$
wavelet rec. / IDFT	$O(N_z)$	$O(N_z \log N_z)$

Table 4.1: Computational complexities of SSW and SSF on one step Δr.

For the filling of the propagation matrix $\mathbf{M}$, the complexity of the propagations in SSW via SSF is $O(LN_z \log N_z)$, and the complexity of the wavelet decompositions is $O(2^L N_z)$. They are also negligible compared to the total complexity of SSW, which is $O(N_r N_z + N_r N_\mathrm{e})$ for $N_r \gg 1$.

4.3 Numerical tests

In this section, several numerical tests are performed to validate the SSW method:

1. To illustrate the computation of $\mathbf{M}$, an example of the propagation on Δr of one wavelet is presented.
2. Propagations without reflection over the ground using different thresholds are tested and compared.
3. Tests over a planar ground with both matrix and signal compressions are performed.
4. A long-range propagation over an irregular relief in an inhomogeneous atmosphere is performed.

4.3.1 Example of propagation for one wavelet

In this test, an example of propagation on Δr for one wavelet is illustrated.

The simulation parameters are $\Delta r = 50$ m, $z_\mathrm{max} = 2048$ m, and $\Delta z = 1$ m. The chosen wavelet family is *symlets*, with the order 6 and the maximum level $L = 3$. The compression threshold is $V_\mathrm{M} = 10^{-3}$.

Assuming one coefficient $U_{l'_0,p'_0} = 1$ with $l'_0 = 2$, $p'_0 = 0$ and all other coefficients are zeros, after applying IFWT, the field of the wavelet $\chi_{2,0}(0,\cdot)$ is obtained. It is plotted in Fig. 4.4a and Fig. 4.4b. We can see that only one coefficient at (l', p') is set to 1. The wavelet is localized at the corresponding position. Then, this wavelet is propagated on Δr by means of SSF. The propagated wavelet $\chi_{2,0}(\Delta r,\cdot)$ is obtained and its electric field is plotted in Fig. 4.4c. It is dilated and deformed compared to the initial wavelet $\chi_{2,0}(0,\cdot)$ due to the propagation. Finally, $\chi_{2,0}(\Delta r,\cdot)$ is decomposed and compressed by V_M. The sparse coefficients $U_{l,p}$ are plotted in Fig. 4.4d. The total number of non-zero coefficients is 147 and the compression rate is 92.8%.

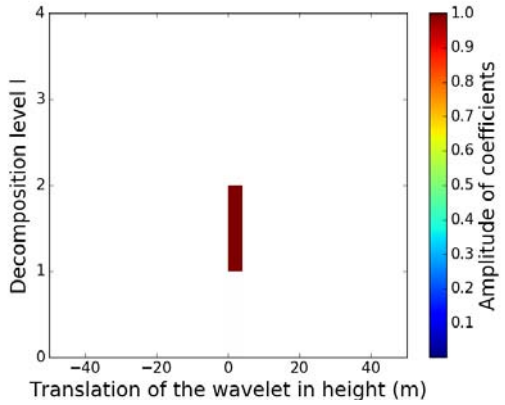

(a) Wavelet coefficient of $\chi_{2,0}(0,\cdot)$

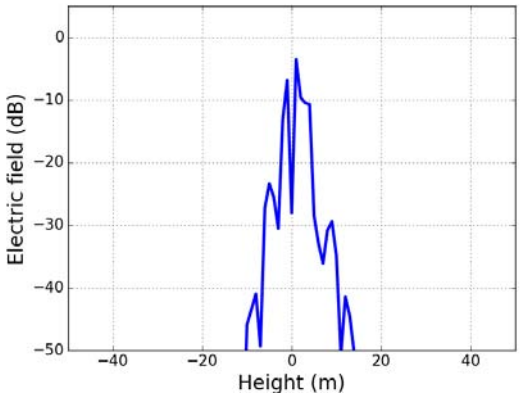

(b) Amplitude of the electric field of $\chi_{2,0}(0,\cdot)$

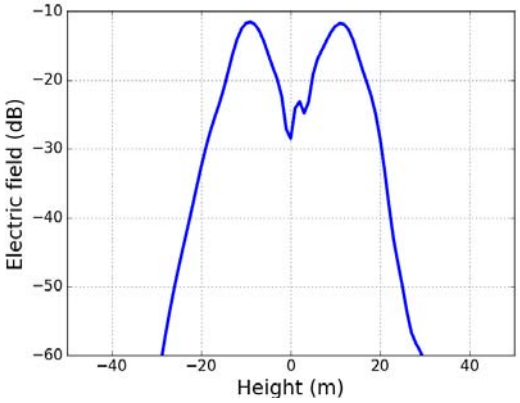

(c) Amplitude of the electric field of $\chi_{2,0}(\Delta r,\cdot)$

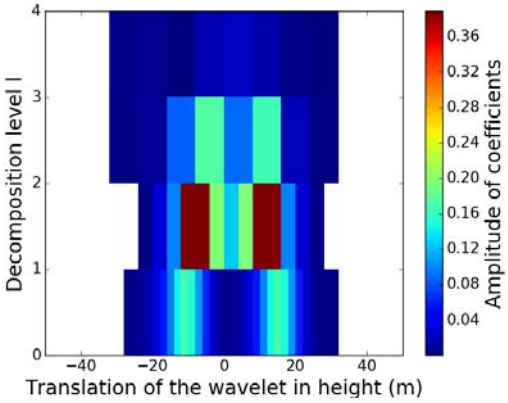

(d) Wavelet coefficient of $\chi_{2,0}(\Delta r,\cdot)$

Figure 4.4: Propagation of the *symlets 6* wavelet $\chi_{2,0}(0,\cdot)$.

Doing so, for a wavelet generated by one single non-zero coefficient $U_{l',p'}$, we know the coefficients $U_{l,p}$ corresponding to this propagated wavelet. The wavelets at other levels l' can be obtained in the same way. Then, the propagation matrix $\mathbf{M}$ is filled by the method introduced in Section 4.2.3.b. In this test, the compression rate of $\mathbf{M}$ is 88.9%. Thus, the propagation matrix is highly compressed, despite a very low error (less than -60 dB) on one propagation step.

4.3.2 Propagation without ground of a complex source point

The propagation of a CSP without ground is tested. The aim is to test the accuracy of SSW with different threshold values. The accuracy of SSW is compared to SSF.

The parameters of the CSP are: frequency $f = 300$ MHz, $r_{\mathrm{w}0} = -50$ m, $y_{\mathrm{s}} = 0$ m, $z_{\mathrm{s}} = 1000$ m, and $W_0 = 5$ m. The height of the source is chosen high enough so that the beam does not reach the ground.

The simulation parameters are $r_{\max} = 1$ km, $\Delta r = 20$ m, $z_{\max} = 2048$ m, and $\Delta z = 1$ m. Thus, $N_r = 50$ and $N_z = 2048$.

The chosen wavelets are *symlets 6* with a maximum level of $L = 3$.

4.3.2.a Effects of the signal and matrix compressions

In order to test the compression thresholds on the matrix $\mathbf{M}$ and on the signal, 3 cases are considered:

- Only matrix compression, $V_{\mathrm{M}} = 2 \times 10^{-3}$ and $V_{\mathrm{s}} = 0$.
- Only signal compression, $V_{\mathrm{s}} = 2 \times 10^{-3}$ and $V_{\mathrm{M}} = 0$.
- No compression, $V_{\mathrm{M}} = V_{\mathrm{s}} = 0$.

The propagation of the normalized electric field in the vertical plane of SSW without compression is shown in Fig. 4.5a. The propagation of the beam is well simulated.

For all cases, the final fields are plotted in Fig. 4.5c. The differences of SSW to SSF, normalized by the final field, are plotted in Fig. 4.5d and 4.5e. The differences are small. The final fields show a very good agreement. Without compression, SSW is of the same accuracy as SSF, as expected.

The evaluation of the RMS difference normalized at each step in range is plotted in Fig. 4.5b. For $V_{\mathrm{M}} \neq 0$ and $V_{\mathrm{s}} = 0$ (green line), the error accumulates in range. The error yielded by the compression on $\mathbf{M}$ is of order of $V_{\mathrm{M}} p_r$ (red dashed line). In the test with $V_{\mathrm{M}} = 0$ and $V_{\mathrm{s}} \neq 0$ (black line), the error increases in range. However, the increase rate is much lower than $V_{\mathrm{s}} p_r$ (about -25 dB below at the final field). A least squares fit yields to an error in $V_{\mathrm{s}} p_r^{\alpha}$, with $\alpha = 0.3$. Therefore, V_{s} can be chosen much larger than V_{M} in practice.

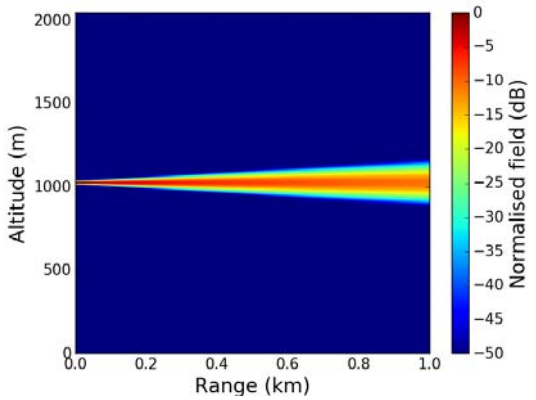

(a) Normalized electric field (dB) in the vertical plane of SSW with no compression

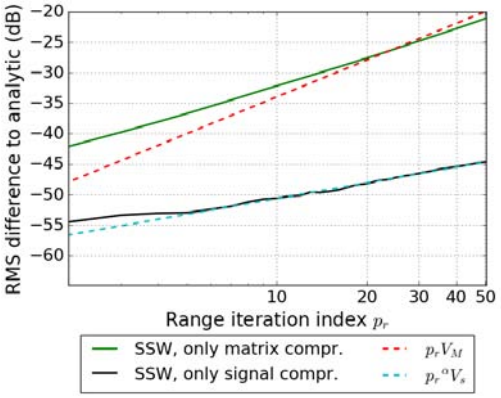

(b) RMS difference of SSW to SSF (dB) on range iterations

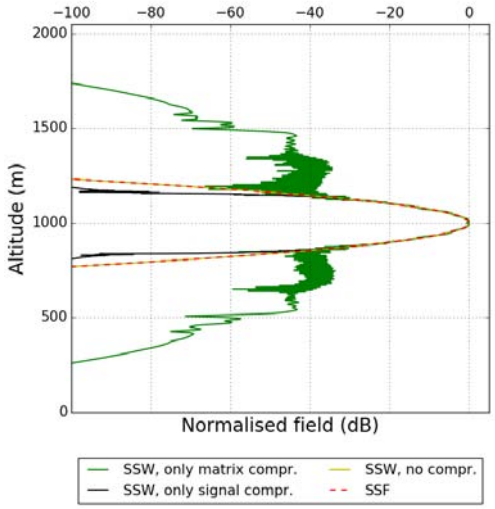

(c) Normalized electric fields (dB) at the final step obtained by SSF and SSW

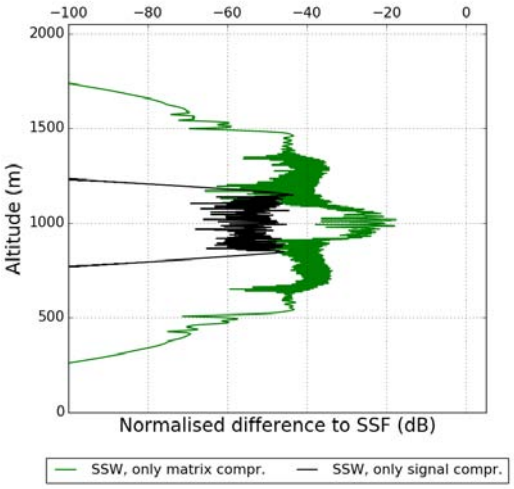

(d) Normalized differences (dB) at the final step of SSW with compression to SSF

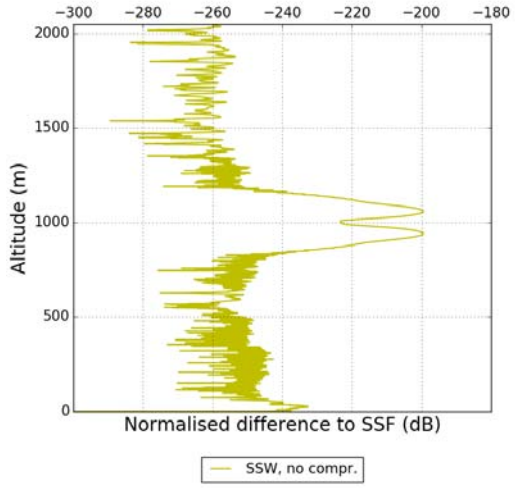

(e) Normalized differences (dB) at the final step of SSW without compression to SSF

Figure 4.5: Propagation of a CSP in free-space.

SSW	test 1	test 2	SSF
V_{M}	2×10^{-4}	2×10^{-5}	
V_{s}	2×10^{-2}	2×10^{-3}	
CR of $\mathbf{M}$ (%)	93.7	86.1	
Average CR of signal (%)	99.1	96.8	
RMS difference with SSF (dB)	-23.0	-44.6	
Time (s)	0.14	0.15	0.37

Table 4.2: Thresholds values, CR, RMS difference, and computation time for free-space propagation of a CSP with compression on $\mathbf{M}$ and the signal.

4.3.2.b SSW with compression on both M and the signal

In this section, compressions on both $\mathbf{M}$ and the signal are applied. Two tests are performed with different thresholds.

In *test 1*, the chosen thresholds are $V_{\mathrm{M}} = 2 \times 10^{-4}$, $V_{\mathrm{s}} = 2 \times 10^{-2}$. Thus, the expected error $\mathscr{E}$ is of order of $20 \log(N_r V_{\mathrm{M}} + N_r^{\alpha} V_{\mathrm{s}}) = -22.5$ dB. The normalized final electrical field of SSW is plotted in Fig. 4.6a. The difference of SSW with the analytic solution is plotted in Fig. 4.6b.

The simulation results including CR, RMS difference, and computation time are shown in Table 4.2. The CR on $\mathbf{M}$ and the signal are very high. In this case, $N_{\mathrm{e}} \leq N_{\mathrm{M}} N_{\mathrm{s}}$, with $N_{\mathrm{M}} = 130$ and $N_{\mathrm{s}} = 18$. Thus, $N_{\mathrm{e}} \leq 2340$. Hence, N_{e} is of order of N_z. The complexity for the propagation in SSW is close to the one for the propagation in SSF. The RMS differences meet well with the expected value. The computation time of SSW is shorter than SSF. The free-space propagation of a CSP using SSW is successfully tested with a high efficiency and a good accuracy.

In *test 2*, $V_{\mathrm{M}} = 2 \times 10^{-5}$, $V_{\mathrm{s}} = 2 \times 10^{-3}$ are chosen and the expected error is of order -42.5 dB. The RMS difference of the result meets quite well with the expected.

4.3.3 Propagation without ground of a uniform aperture

A uniform aperture (see Section 1.8.2.b) is considered with $a = 5$ m, $r_{\mathrm{s}} = 0$ m, and $z_{\mathrm{s}} = 2000$ m. The vertical height is $z_{\max} = 4096$ m. The other parameters are the same as in the previous test.

4.3.3.a Effects of the signal and matrix compressions

Three cases are considered with the same thresholds as in Section 4.3.2.a. The propagation from the aperture and the normalized final electric field are plotted in Fig. 4.7a and Fig. 4.7b. The differences of SSW to SSF are plotted in Fig. 4.7c and Fig. 4.7d. The propagation is well simulated and the error due to the compression is acceptable. The thresholds are -20.9 dB with only matrix compression, -39.6 dB with only signal

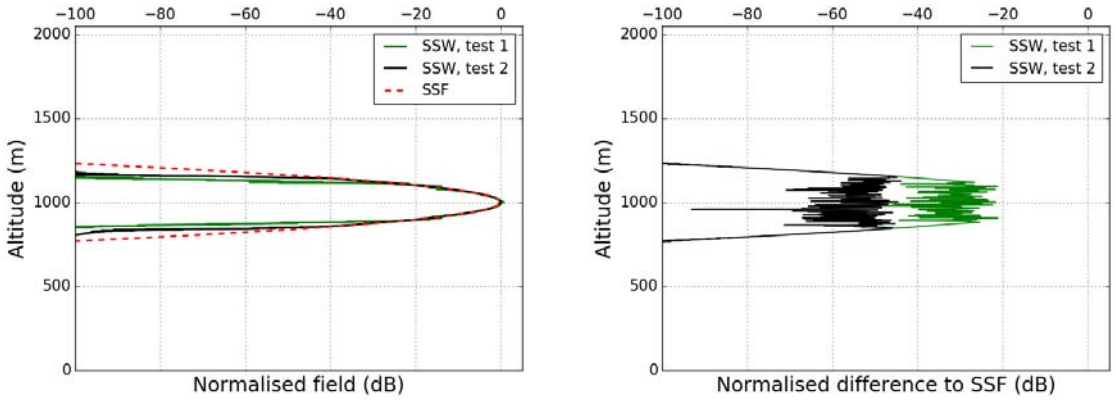

(a) Normalized electric fields at the final step obtained by SSF and SSW

(b) Differences of SSW to SSF

Figure 4.6: Free-space propagation of a CSP with compression on M and the signal.

compression, and −113.3 dB without compression. The result is similar to the test with a CSP in Section 4.3.2.a.

The evaluation of the RMS difference normalized at each step in range is plotted in Fig. 4.8a. In the test with only matrix compression, the error is of order of $V_{\mathrm{M}} p_r$ (red dashed line). In the test with only signal compression, the error increases of order of $V sp_r^{\alpha}$, with $\alpha = 0.3$. This result is the same as the test with a CSP. Thus, for a beam with stronger variations, SSW simulates well the propagation.

4.3.3.b SSW with compression on both M and the signal

SSW with compression on both **M** and the signal are tested on the propagation from the aperture. The chosen thresholds are the same as in Section 4.3.2.b.

The propagation from the aperture, the normalized final electric field, and the difference of SSW to SSF are plotted in Fig. 4.8 and the thresholds values, CR, and RMS difference are shown in Table 4.3. Similarly to the test of propagation of a CSP, SSW shows very high CR for both **M** and the signal. The differences meet well with the expected values. The computation time of SSW is shorter than SSF.

4.3.4 Propagation over a planar ground in a homogeneous atmosphere

The aim of this section is to test SSW with a planar ground using the local image method introduced in Section 4.2.5.

A CSP with the same parameters as in Section 4.3.2 is chosen at a height of $z_{\mathrm{s}} = 30$ m. The simulation parameters are $r_{\max} = 50$ km, $\Delta r = 100$ m, $z_{\max} = 4096$ m, and $\Delta z = 1$ m. Thus, $N_r = 500$ and $N_z = 4096$.

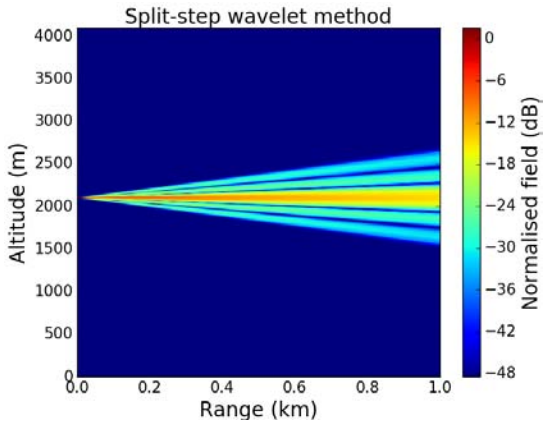

(a) Propagation from the uniform aperture of test 1

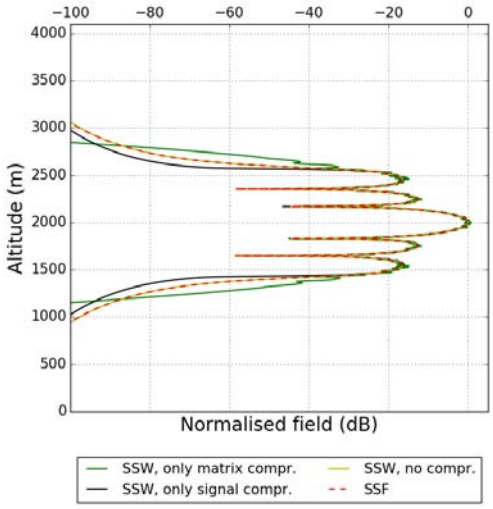

(b) Normalized electric fields (dB) at the final step obtained by SSF and SSW

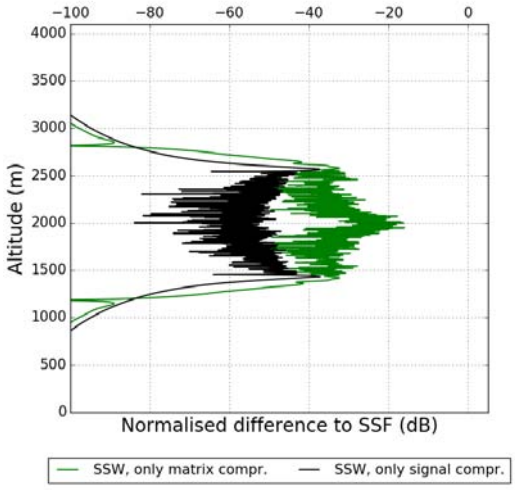

(c) Differences (dB) at the final step of SSW to SSF, matrix or signal compression

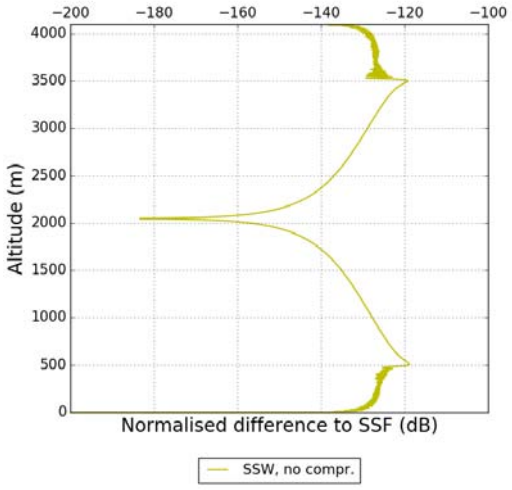

(d) Normalized differences (dB) at the final step of SSW to SSF, no compression

Figure 4.7: Propagation without ground for a uniform aperture.

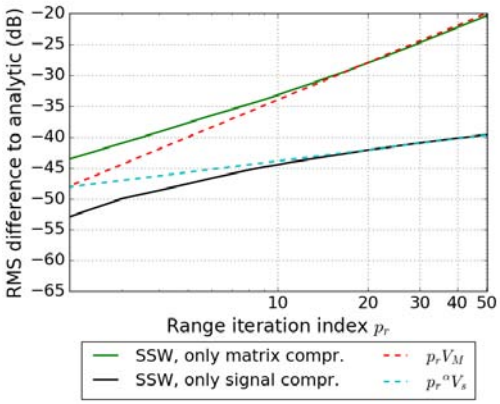

(a) RMS differences of SSW fields to SSF on range iterations

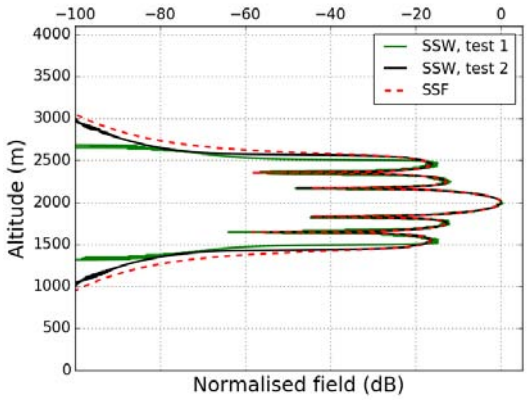

(a) Normalized electric fields at the final step obtained by SSF and SSW

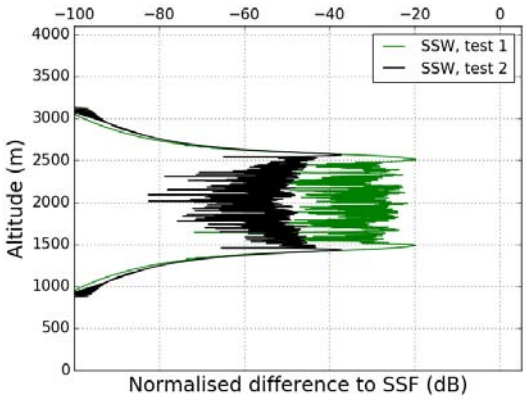

(b) Differences of SSW to SSF

Figure 4.8: Free-space propagation of a uniform aperture with compression on M and the signal.

SSW	test 1	test 2	SSF
V_{M}	2×10^{-4}	2×10^{-5}	
V_{s}	2×10^{-2}	2×10^{-3}	
CR of $\mathbf{M}$ (%)	96.7	92.1	
Average CR of signal (%)	93.7	90.0	
RMS difference with SSF (dB)	-19.5	-39.6	
Time (s)	0.24	0.27	0.70

Table 4.3: Thresholds values, CR, RMS difference, and computation time for free-space propagation of a uniform aperture with compression on $\mathbf{M}$ and the signal.

4.3.4.a Propagation over a planar PEC ground

A planar PEC ground is considered. A thin imaginary layer $N_{\mathrm{im}} = 200$ is added to the computation domain for applying the local image method.

Two tests using SSW with compression on both $\mathbf{M}$ and the signal are tested. The chosen thresholds are $V_{\mathrm{M}} = 2 \times 10^{-4}$, $V_{\mathrm{s}} = 2 \times 10^{-2}$ in test 1 and $V_{\mathrm{M}} = 2 \times 10^{-5}$, $V_{\mathrm{s}} = 2 \times 10^{-3}$ in test 2. Since $N_r = 50$, the expected errors are of order of $\mathscr{E} = 20 \log(N_r V_{\mathrm{M}} + N_r^{\alpha} V_{\mathrm{s}})$, which are -12.8 dB and -32.8 dB, respectively. The propagation along range and the final electric field of SSW compared to SSF are shown in Fig. 4.9, where the interference pattern due to the ground reflection is visible.

The simulation results including the CR, RMS difference, and computation time are given in Table 4.4. The CR on $\mathbf{M}$ and the average CR on the signal are high, which reduces the computation load in SSW. The RMS difference of the final field of SSW to SSF depends on the thresholds. They are better than the expected values. Moreover, SSW is faster than SSF by a factor of 2.4. As expected, smaller thresholds correspond to a higher accuracy and a longer simulation time. Besides, the computation time for creating $\mathbf{M}$ is

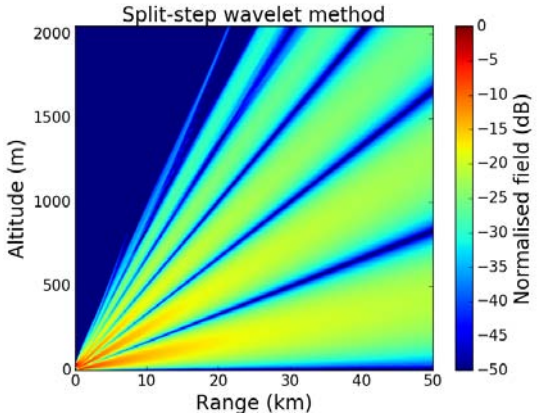

(a) Normalized electric field in the vertical plane obtained with SSW of test 1

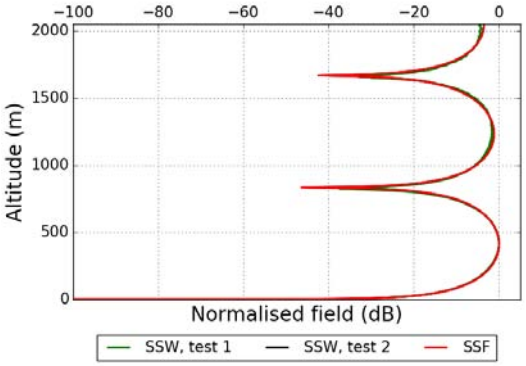

(b) Normalized electric fields at the final step obtained by SSF and SSW

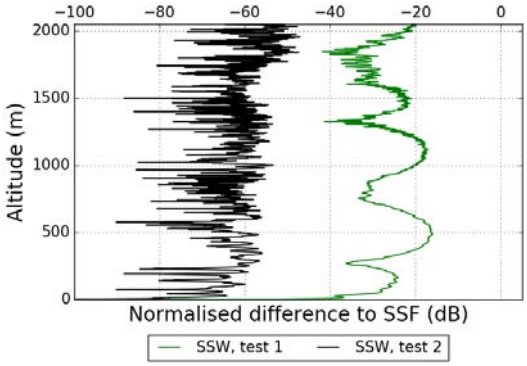

(c) Differences of SSW to SSF

Figure 4.9: Propagation over a PEC ground of a CSP with $W_0 = 5$ m centered at 30 m.

SSW	test 1	test 2	SSF
V_{M}	2×10^{-4}	2×10^{-5}	
V_{s}	2×10^{-2}	2×10^{-3}	
CR of $\mathbf{M}$ (%)	93.4	85.7	
Average CR of signal (%)	89.6	82.1	
RMS difference with SSF (dB)	-18.3	-54.8	
Time (s)	2.8	3.0	7.7

Table 4.4: Thresholds values, CR, RMSE, and computation time for propagation over a planar PEC ground.

about 1.2 s. As a conclusion, SSW with a PEC ground is successfully tested in terms of accuracy and shows its advantage in terms of computation time.

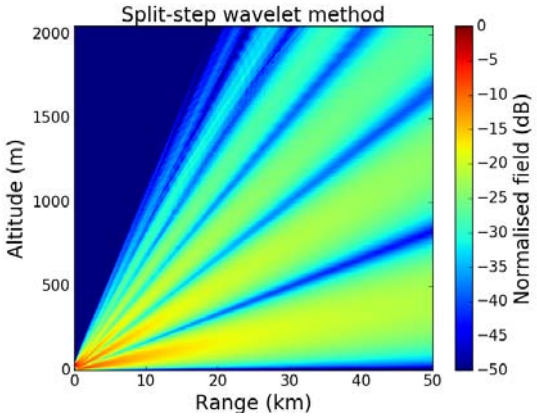

(a) Normalized electric field in the vertical plane obtained with SSW of test 1

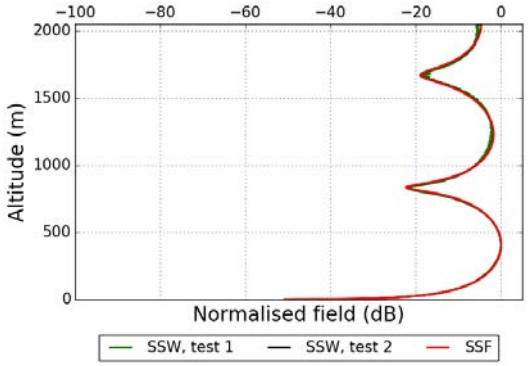

(b) Normalized electric fields at the final step obtained by SSF and SSW

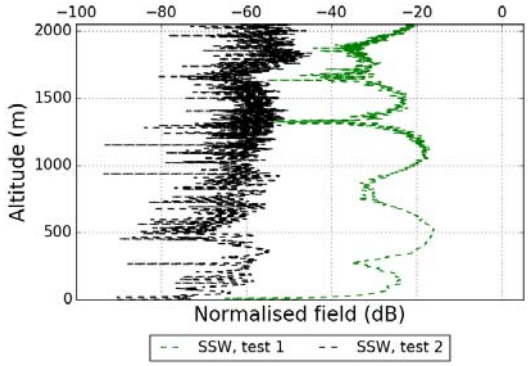

(c) Differences of SSW to SSF

Figure 4.10: Propagation over an impedance ground of a CSP with $W_0 = 5$ m centered at 30 m.

4.3.4.b Propagation over a planar impedance ground

Then, a planar impedance ground with $\epsilon_r = 20$ and $\sigma = 0.02$ S/m is considered. All other parameters are the same as in the previous test.

Two tests are performed with exactly the thresholds chosen in Section 4.3.4.a. The propagation for test 1 is shown in Fig. G.9. The interference pattern due to the ground is visible. The simulation results including the CR, RMS difference, and computation time are shown in Table G.2. The results are almost the same as for the propagation over a PEC ground. SSW with an impedance ground is also successfully tested. The gain in the computation time is here only of 1.56. This is less than in Section 4.3.4.a because of the transforms between u and w in DMFT.

SSW	test 1	test 2	SSF
V_{M}	2×10^{-4}	2×10^{-5}	
V_{s}	2×10^{-2}	2×10^{-3}	
CR of $\mathbf{M}$ (%)	93.4	85.7	
Average CR of signal (%)	88.6	81.6	
RMS difference with SSF (dB)	-18.3	-52.8	
Time (s)	9.1	9.3	14.2

Table 4.5: Thresholds values, CR, RMSE, and computation time for propagation over a planar impedance ground.

4.3.5 Long-range propagation over an impedance irregular relief in an inhomogeneous atmosphere

In this part, we test a long-range propagation over an irregular relief in an inhomogeneous atmosphere.

In the vertical direction, we consider a surface-based duct, which is modeled by a trilinear modified refractivity (see Section 1.8.5). The parameters are: $M_0 = 330$ M-units, $z_b = 100$ m, $z_t = 200$ m, $z_{\max} = 4096$ m, with gradients $c_0 = 0.118$ M-units/m, $c_2 = -0.1$ M-units/m.

The relief is chosen as 2 small triangular hills of heights 100 m and 200 m. The characteristics of the impedance ground are $\epsilon_r = 20$ and $\sigma = 0.02$ S/m.

In this test, the propagation range is $r_{\max} = 100$ km. The range step is 200 m, $N_r = 100$. We choose $V_{\mathrm{M}} = 2 \times 10^{-4}$ and $V_{\mathrm{s}} = 2 \times 10^{-2}$.

The propagation using SSW is shown in Fig. G.10a. The refractive effects of the surface-based duct and the reflection by the irregular ground are properly simulated. The final fields and the difference to SSF are plotted in Fig. G.10b. The RMSE of the final field of SSW to SSF is -21.6 dB. Therefore, SSW works well for a long range simulation over an irregular relief in an inhomogeneous atmosphere. The computation time is 9.7 s for SSW and is 15.1 s for SSF. Therefore, SSW has a better computation efficiency than SSF, even on complex scenarios.

4.4 Conclusion

Based on the fast wavelet transform (FWT) and data compression introduced in the previous chapter, the split-step wavelet method (SSW) for the simulation of long-range electromagnetic wave propagation has been defined.

First, the proposed SSW method has been introduced. The field is represented as a sparse set of coefficients after applying FWT and thresholding. It is then propagated in free-space by means of a pre-computed propagation matrix. The propagated field is recomposed by an inverse FWT from the propagated wavelets. The strategy to create the pre-computed propagation matrix has also been introduced.

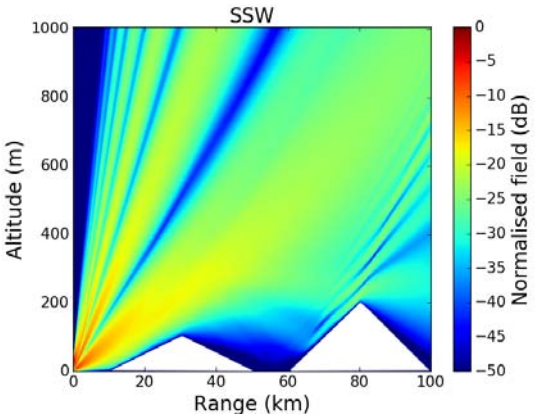

(a) Normalized electric field (dB) obtained by SSW

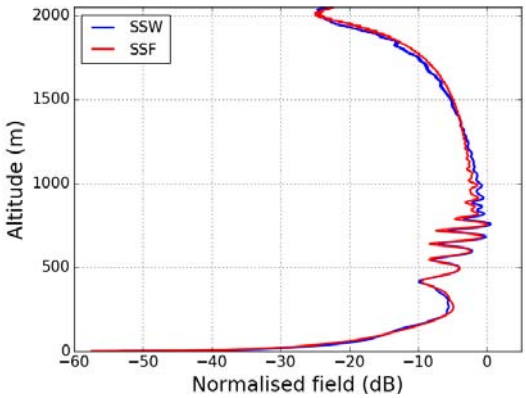

(b) Normalized electric fields at the final step obtained by SSF and SSW

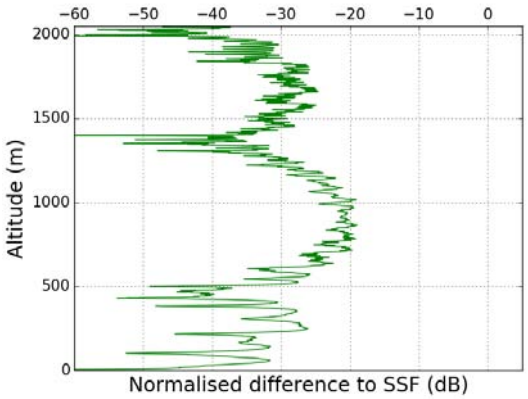

(c) Difference of SSW to SSF

Figure 4.11: Propagation over a planar impedance ground in an inhomogeneous atmosphere and over an irregular relief.

Second, considering a perfect conducting ground, a local image method has been proposed. Then this method has been extended to impedance grounds. Domain truncation, atmosphere refractivity, and an irregular relief are also accounted at each step. The total field is obtained iteratively.

Then, the computation complexity of SSW has been compared to the classic SSF method. SSW has an advantage in computation efficiency due to the high compression rate of the wavelet decomposition and the low complexity of the fast wavelet transform.

Finally, numerical tests of wave propagation have been presented to show the accuracy and efficiency of this method. First, the propagation on Δr of one wavelet has been tested. This illustrates the procedure for filling the propagation matrix. Second, propagations without ground reflection of a CSP and a uniform aperture with different thresholds have been tested and compared. The error of SSW due to matrix compression (threshold V_{M}) accumulates with range and is of order $V_{\mathrm{M}} N_r$. Experimental results show that the one due to signal compression (threshold V_{s}) accumulates with range but with a much lower rate. Moreover, SSW without compression is of the same accuracy as SSF.

Then, tests of propagation over a PEC and an impedance planar ground with both matrix and signal compressions have been performed. The error of SSW depends on the thresholds and its value is as expected. SSW has a high accuracy and better computational efficiency compared to SSF. The local image method has been successfully tested. Finally, a long-range propagation over an irregular relief in an inhomogeneous atmosphere has been performed. The result of SSW shows a very good match with SSF. SSW works well for a long range simulation with reduced computation time. The gain of the computation time is 1.5 compared to SSF. We think this value could be further improved since SSW is still at its early stages.

Conclusion

The objective of this Ph.D. thesis was to develop a fast and self-consistent method for modeling the tropospheric propagation for both 2D and 3D complex environments. Several significant milestones towards this objective have been achieved.

1. Based on parabolic equation and split-step Fourier, a self-consistent method in the discrete domain has been developed in 2D.

2. Directly derived from the wave equation, a self-consistent propagation method in the discrete domain has been developed in 3D. Moreover, a sectoral propagation method has been proposed to alleviate the computation burden.

3. A new split-step wavelet method in 2D has been proposed with a higher efficiency than SSF while keeping a good accuracy.

Summary

In the **first chapter**, the split-step Fourier method for simulating the long-range propagation in a complex environment in 2D has been presented. The propagation methods over a PEC ground have firstly been considered. The parabolic equation method has been introduced, in which the paraxial approximation is assumed and the backward propagation is neglected. The split-step scheme has been presented for modeling the propagation marching on in distance.

In a preliminary step, the method has been derived from the continuous equations, SSF-ST. To be applied in numerical applications, an *a-posteriori* discretization has been performed. Then, a self-consistent discrete method, DSSF-DST, has been proposed, where the spectral transform and the propagator are both based on the discrete equations.

The 2D methods have been extended to impedance grounds. A continuous formulation with the mixed Fourier transform, SSF-MFT, has been reminded. Then, this method has been discretized. Working directly in the discrete domain has yielded a discrete method, DSSF-DMFT, for which self-consistency is obtained. Moreover, an inconsistency in the widely used method SSF-DMFT has been highlighted. As a consequence, DSSF-DMFT is recommended.

Numerical tests have shown that the propagation using SSF-ST and DSSF-DST are both

accurate. For the propagation with an impedance ground, in certain conditions, the SSF-DMFT shows spurious oscillations, whereas DSSF-DMFT remains accurate. Moreover, a long-range propagation over an irregular relief in an inhomogeneous atmosphere has shown the usefulness of DSSF-DMFT.

In the **second chapter**, the SSF propagation method in 3D cylindrical coordinates has been introduced. Firstly, a PEC planar ground has been assumed. The continuous formulation has been presented. The continuous propagator with Hankel functions has been derived for the propagation in the spectral domain. For numerical applications, the discretization form of the continuous formulation, 3D-SSF-ST has been developed. Then, an entire discrete formulation, 3D-DSSF-DST, has been proposed. The formulation has been developed from the discrete equation. Considering an impedance planar ground, a self-consistent discrete method, 3D-DSSF-DMFT has been presented. This method has been compared to the extension of the inconsistent SSF-DMFT to 3D. The propagators in both methods have different expressions. 3D-DSSF-DMFT is preferred to achieve self-consistency in the discrete domain.

An explicit numerical scheme for considering a slowly varying refractivity has been introduced. The phase-screens method valid at wide angles has been applied in the spatial domain. A sectoral propagation method has also been introduced to propagate more efficiently directive beams.

Numerical tests have been presented. Firstly, the sectoral propagation and the 3D formulation have been validated. Secondly, different refractivity models have been considered. The effects of the inhomogeneous atmosphere along the vertical and horizontal directions have been properly simulated. The 3D method takes into account the azimuthal effects which is an advantage over $N \times 2D$ models. Thirdly, the simulation accuracy with an impedance ground of 3D-DSSF-DMFT and 3D-SSF-DMFT have been compared. The results with both propagators are accurate. The discrete formulation achieves self-consistency and should be preferred for numerical simulations. Finally, the method in realistic atmospheric ducting conditions has been tested. The 3D model has a better accuracy since lateral effects are considered. However, the computation time is too long for a regular use. This has motivated the following work.

In the **third chapter**, the discrete wavelet transform (DWT) has been introduced. The wavelets are wave-like functions that are localized in both the space and the frequency domains. They are constructed by dilations and translations of a mother wavelet. The fast wavelet transform (FWT) that allows a fast DWT computation has been described. The main parameters of the wavelets have been discussed. Finally, the common wavelets used for FWT have been introduced.

Numerical tests have been performed with different wavelet parameters. The fields radiated from a complex source point (CSP) and a uniform aperture at different distances have been considered. The wavelet parameters have been chosen from a parametric study. The computation times of FWT have been compared to FFT, showing the good efficiency of FWT, since the computation complexity of FWT is $O(N)$ and the one of

FFT is $O(N \log N)$.

In the **fourth chapter**, the new split-step wavelet method (SSW) for the simulation of long-range electromagnetic wave propagation has been defined. It is based on FWT and data compression.

The steps of the method are as follows: The field is represented as a sparse set of coefficients after applying FWT and thresholding. It is then propagated in free-space by means of a pre-computed propagation matrix. The propagated field is recomposed by an inverse FWT from the propagated wavelets. Atmosphere and relief are accounted in the spatial domain.

The strategy to create the pre-computed propagation matrix has been introduced. Due to the properties of the wavelets, only few decompositions are required. Moreover, considering a perfect conducting ground, a dedicated and efficient local image method has been proposed. Then this method has been extended to impedance grounds.

The computation complexity of SSW has been compared to SSF. SSW has an advantage in computation efficiency due to the high compression rate of the wavelet decomposition and the low complexity of the FWT.

Numerical tests have been presented to show the accuracy and efficiency of this method. We have shown that the error of SSW due to matrix and signal compressions can be controlled. Propagation over a PEC and an impedance planar ground using SSW have been successfully tested. SSW has a high accuracy and better computational efficiency compared to SSF. A long-range propagation over an irregular relief in an inhomogeneous atmosphere has been performed. The result of SSW shows a very good match with SSF. SSW works well for a long range simulation with a computation time reduction of about 40% to 60%.

Perspectives and applications

In this Ph.D. thesis, we have introduced fast and self-consistent methods for long-range atmospheric propagation in 2D and 3D. The tests have shown that the results using these methods are satisfactory. To continue these researches, several future works could be considered. They concern the models, the tests, and the applications to realistic systems.

Methods

In 2D-SSW, the method of apodization could be optimized using the localization property of wavelets to reduce the size of the apodization layer. In this thesis, Hanning window is used to remove the reflection over top boundary. However, the vertical size of the absorbing layer is the same as the computation domain. This costs computation resources. A more efficient method could be developed, which could be based on the localization property of wavelets.

Moreover, for 2D-SSW, the propagation strategy could be further optimized. In this thesis, a matrix is created to model the propagation of wavelets. The matrix contains the propagated coefficients for all the wavelets. Since wavelets are constructed by translations, lots of redundant information are stored in this matrix. If we consider a propagation with a much larger scale, the dimension of the matrix will be enormous and the memory occupation will become a main concern. Hence, a better strategy for the wavelet-to-wavelet propagation operator could be proposed to further improve the efficiency of SSW.

In addition, the evolution of error with the iterations could be further studied. The tests in this Ph.D. thesis have shown that the error due to the matrix compression is of order of $N_r V_{\mathrm{M}}$ and the one due to the signal compression is about $N_r^{\alpha} V_{\mathrm{s}}$, with $\alpha = 0.3$. A demonstration for the envelop of these errors could be sought.

I am currently developing a new wavelet-based method without field-wavelet transforms. It works only with the wavelet representation. As in SSW, The coefficients are propagated for each step by means of multiplying the propagation matrix. In contrast to SSW, the apodization and refractivity are modeled directly on the wavelet coefficients. Since no transform is needed, this method further improves the modeling efficiency. Hybridization with SSW could be necessary for accounting the relief.

The 2D-SSW method could be extended to 3D. The wavelet decomposition on the vertical and horizontal directions would be applied. This would significantly improve the efficiency of 3D propagation methods. This work will be realized during the Ph.D. of Thomas Bonnafont started in October 2017 at ENAC.

In 3D-DSSF, the method for considering an irregular relief could be studied. Since a 3D relief is accounted, depolarization of the field occurs. Propagating the TM and TE components together is a complex matter. Moreover, the lateral reflection is challenging to model. These aspects could be further studied.

The refraction model could be developed for modeling the tropospheric and ionospheric scintillations both in 2D and 3D. Scintillation is the rapid modification of radio waves caused by small scale structures in atmosphere. This could be realized by means of modifications of the phase-screens formulations [98].

Tests and validations

In addition, more validations and tests could be performed as follows. Firstly, our method could be compared to the Gaussian beam-based method developed by L'Hour [60], which models the propagation in troposphere. As SSW, this method has been proven to be more efficient than SSF in 2D. Moreover, our method could be compared to other methods, as ray tracing, for further validation purpose.

Secondly, our method could be compared to measurements. As a preliminary test, in Section 2.8.5, we have already modeled the propagation through a duct retrieved after clutter data inversion [87]. With this model, we have simulated the propagation in a

realistic environment. However, the 3D effects are not obvious. Other extreme weather conditions could be considered to clearly show the 3D effects.

Thirdly, more tests could be performed with the refractivity models of the international telecommunication union (ITU) [15] or with weather research and forecasting models (WRF) [16]. Doing so, the propagations in realistic atmospheres could be modeled.

Applications

The possible applications of these methods are various. Firstly, these methods could be used for the prediction of the radar coverage and for the definition, design, implementation of the ground facilities and systems.

Secondly, the methods could be applied for modeling radio-occultation (RO) configurations. A RO configuration corresponds to a situation where a GNSS satellite and a low-altitude (LEO) satellite are between light-of-sight and non-light-of-sight situations because of the Earth shadowing. The propagation of radio signals transmitted by the satellites should be modeled over the Earth on several thousands kilometers at grazing angle, which is difficult with SSF methods. Our method could be used for modeling this configuration. The preliminary step of this work has been studied by Romain Bertrand during his internship at ENAC [99].

Finally, the methods could be applied to model the propagation in ionosphere. The ionosphere is the atmospheric layer, from 75 km to 1000 km above the Earth, which is ionized by solar and cosmic radiation. Due to the high energy from the Sun and cosmic rays, the atoms in this area have been positively charged. This layer has influences on the radio propagation for long-distance, or on the propagation between satellites and Earth. Our method is believed to be an efficient tool to treat this kind of problem.

Appendix A

Refractive index models and Earth flattening transform

The refraction is characterized by the refractive index, which has a strong influence on the radio waves propagation in the troposphere. In this section, different common refractivity models are presented. These models are simple approximations of the realistic atmosphere. Then, an Earth-flattening transform is presented to account for the Earth's curvature.

A.1 Different refractivity models

In this section, exponential, linear, and atmospheric duct models are introduced.

A.1.1 Exponential model

In an ideal atmosphere, the refractivity N decreases exponentially with height z. This results in an exponential model

$$N(z) = N_0 \exp(-z/h_0) \tag{A.1}$$

with N_0 the sea-level refractivity and h_0 the scale height. The standard atmosphere model defined by the International Telecommunications Union [100] is

$$N(z) = 315 \exp(-0.136z) \tag{A.2}$$

with z given in km.

A.1.2 Linear model

At low heights, less than several kilometers, the exponential model can be approximated by a linear model.

$$N(z) = N_0 + c_1 z. \tag{A.3}$$

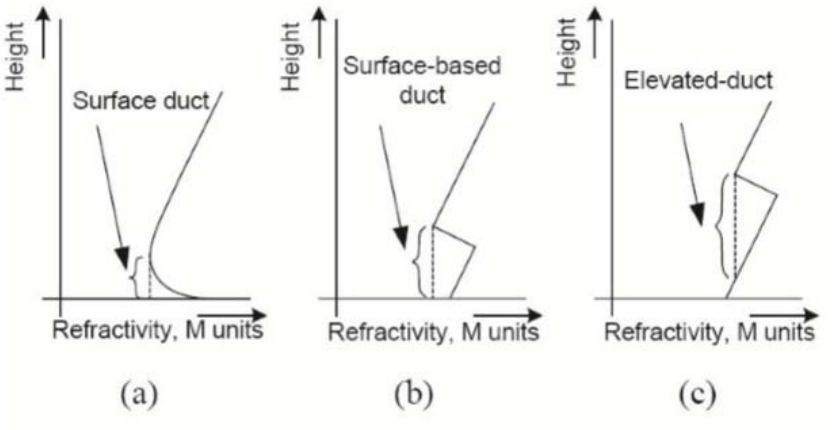

Figure A.1: Types of atmospheric duct [101].

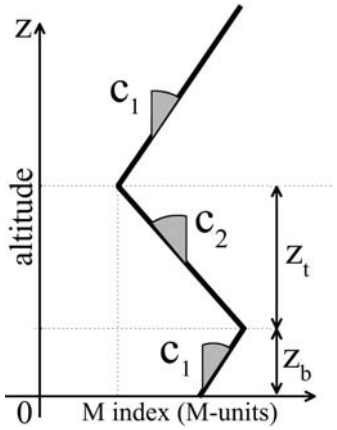

Figure A.2: Surface based duct trilinear model.

with c_1 the mean atmospheric gradient of the low-height atmosphere.

For the standard atmosphere, in the first kilometer, $c_1 = -40$ N-units/km in the mid-latitude climates [12]. This value could vary widely depending on the local climate.

A.1.3 Atmosphere duct model (trilinear model)

In more complex weather conditions, a ducting layer may appear in troposphere. Common ducts are surface duct (ground-based duct), surface-based duct and elevated duct. The major causes for formation of ducts are evaporation, nocturnal radiation, subsidence inversion and advection.

To consider a surface-based duct, a trilinear refractivity model can be applied. As illustrated in Fig. A.2. In the area $z \in [z_\mathrm{b}, z_\mathrm{b} + z_\mathrm{t}]$, the refractivity gradient is c_2. In the other areas, the gradient is c_1.

A.2 Earth flattening transform

Earth-flattening transforms provides a means for including the Earth's curvature for wave propagation. The wave equation is approximately valid when the refractivity n is replaced by the modified refractivity m, given by

$$m(x, z) = n(x, z) + \frac{h}{r_E}, \tag{A.4}$$

with r_E is the radius of the Earth and z is height above the Earth's surface. It is convenient to consider the modified refractivity m by M-units, such that

$$M = 10^6 \times (m - 1). \tag{A.5}$$

This formulation loses accuracy at larger heights. To model fields at higher altitudes, an algorithm with the logarithmic height transformation has been introduced in [12].

Appendix B

Irregular terrain modeling

Accurate modeling for the wave propagation over an irregular ground is important. The accuracy of the irregular terrain modeling depends on the choice of the terrain representation. The simplest solution is a sequence of horizontal steps, as shown in Figure B.1. The slopes are modeled approximately by the staircases.

In this model, on each segment Δr, the height is constant and the level of the staircases are quantified to $p_z \Delta z$. When the terrain height changes, corner diffraction is not well modeled and the field is simply set to zero on the vertical terrain facets. In each segment, we apply the appropriate boundary condition at the ground.

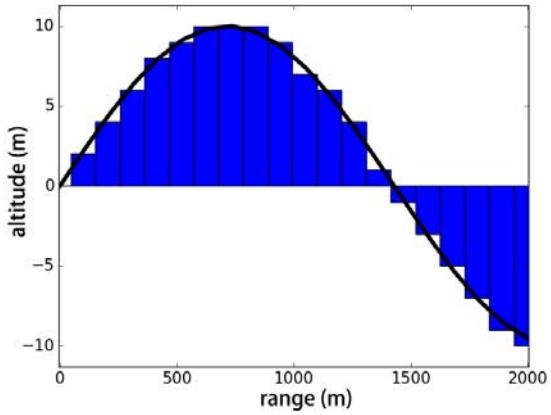

Figure B.1: Staircase modeling.

Two cases may occur:

- For the ascending step case:
  As shown in Figure B.2a, the field u_{p_r} is propagated on Δr. The propagated field is denoted as u_{p_r+1}. At distance r_{p_r}, the ground is situated at $z = h_{p_r}$. Then, a staircase ascending step follows, the ground is at the altitude index $h_{p_r+1} = h_{p_r} + h_d$ with $h_d > 0$. Assuming that the backscattering propagation is neglected and the ground does not

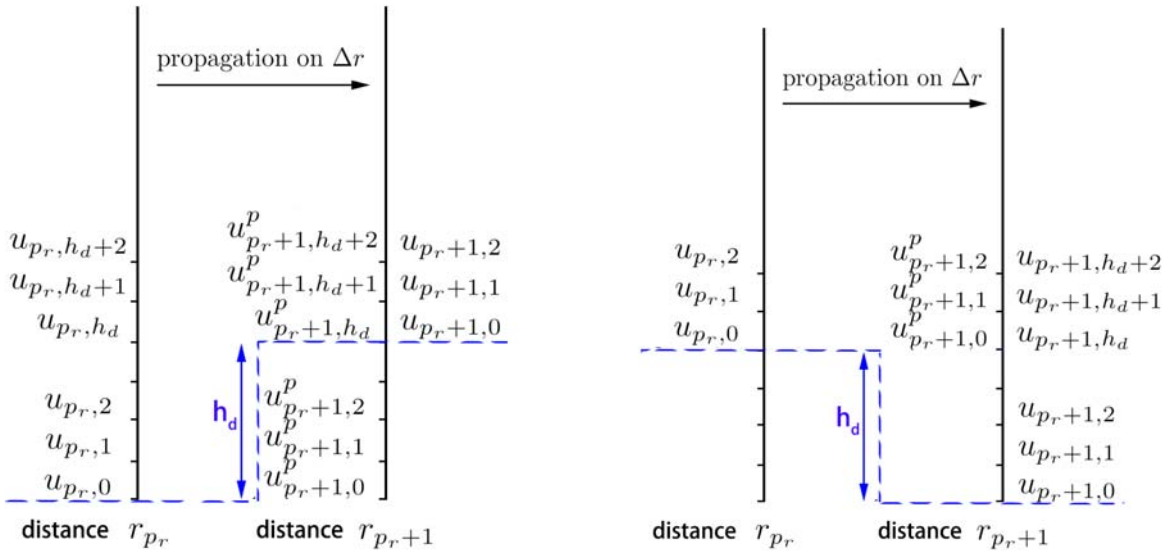

(a) Ascending steps (b) Descending steps

Figure B.2: Advancing the PE solution on steps terrain.

support propagation at the wavelength of interest, we set

$$u_{p_r+1,p_z} = u^{\mathrm{p}}_{p_r+1,p_z+h_d}, \tag{B.1}$$

for $p_z = \{0, \ldots, N_z - 1 - h_d\}$. Thus, the ground is considered to be situated at $z = 0$ for u_{p_r+1}.

- For the descending steps case: As shown in Figure B.2b, similar as in the ascending case, the field u_{p_r} is propagated on Δr. A staircase ascending step follows, the ground is at $h_d < 0$. Because we neglects backscattering due to corner diffraction, we set

$$u_{p_r+1,p_z} = \begin{cases} u^{\mathrm{p}}_{p_r+1,p_z+h_d} & \text{for } p_z \geq -h_d \\ 0 & \text{for } p_z < -h_d \end{cases} \tag{B.2}$$

  Then, the SSF is applied to consider the ground.

In the case that the variation of the relief is smooth, this model is good approximation. Otherwise, other more accurate models can be implemented in [12]. Moreover, the relief can be considered by other different algorithms [31][67][68]. As the relief is not the main purpose of the present work, we only use the staircase model.

Appendix C

Impedance boundary condition

In this section, the impedance boundary condition in 2D is detailed.

Two dielectric mediums besides the interface are assumed, as illustrated in Fig. C.1. The conductivity and permittivity are σ_1, $\epsilon_{\text{eff},1}$ and σ_2, $\epsilon_{\text{eff},2}$, respectively in 2 mediums. The effective permittivities are defined by $\epsilon_{\text{eff},1} = \sqrt{(\sigma_1 + j\omega\epsilon_{\text{eff},1})/j\omega}$ and $\epsilon_{\text{eff},2} = \sqrt{(\sigma_2 + j\omega\epsilon_{\text{eff},2})/j\omega}$.

The incident wave number could be represented as $\boldsymbol{k}_{\text{in}} = k_{\text{in}}\boldsymbol{k}_{\text{in}} = k_{\text{in,r}}\boldsymbol{r} + k_{\text{in},\theta}\boldsymbol{\theta} + k_{\text{in,z}}\boldsymbol{z}$. The reflected and transmitted wave numbers are $\boldsymbol{k}_{\text{re}}$ and $\boldsymbol{k}_{\text{tr}}$. The decomposition on coordinates yields $\boldsymbol{k}_{\text{tr}} = k_{\text{tr,r}}\boldsymbol{r} + k_{\text{tr},\theta}\boldsymbol{\theta} + k_{\text{tr,z}}\boldsymbol{z}$.

The Fresnel coefficient, for TE component, is given by

$$\Gamma = \frac{k_{\text{in,z}} - k_{\text{tr,z}}}{k_{\text{in,z}} + k_{\text{tr,z}}}. \tag{C.1}$$

For TM component, it is given by

$$\Gamma = \frac{\epsilon_{\text{eff},2}k_{\text{in,z}} - \epsilon_{\text{eff},1}k_{\text{tr,z}}}{\epsilon_{\text{eff},2}k_{\text{in,z}} + \epsilon_{\text{eff},1}k_{\text{tr,z}}}, \tag{C.2}$$

with $k_{\text{tr,z}} = \sqrt{k_2^2 - k_1^2 \sin^2\theta_{\text{in}}}$.

The impedance for TE component is

$$Z = \frac{\zeta_1}{\cos\theta_{\text{in}}}\frac{1+\Gamma}{1-\Gamma}, \tag{C.3}$$

the impedance for TM component is

$$Z = \zeta_1 \cos\theta_{\text{in}}\frac{1-\Gamma}{1+\Gamma}, \tag{C.4}$$

with $\zeta_1 = \sqrt{\frac{\mu_0}{\epsilon_{\text{eff},1}}}$ the impedance of the medium 1, θ_{in} the angle of incidence, Γ the coefficient of Fresnel.

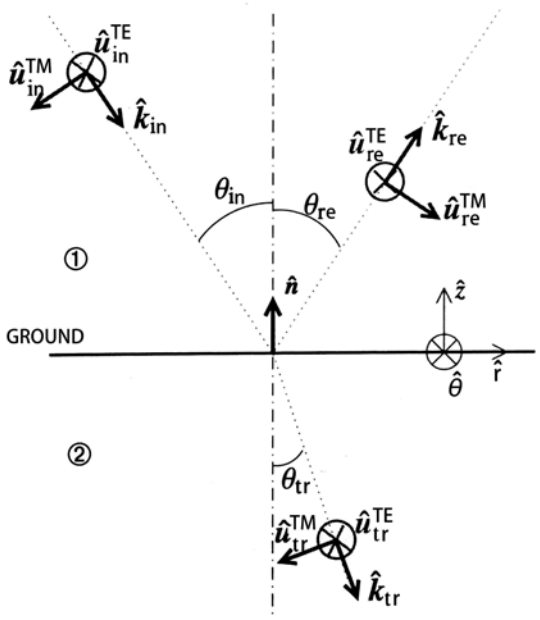

Figure C.1: Plane of incidence.

By replacing the reflection coefficient in (C.3) and (C.4) by (C.1) and (C.2), for TE component

$$Z = \frac{\zeta_1}{\cos\theta_{\text{in}}}\frac{k_{\text{in,z}}}{k_{\text{tr,z}}} = \frac{-\zeta_1 k_1}{k_{\text{tr,z}}} = \frac{-\sqrt{\frac{\mu_0}{\epsilon_{\text{eff},1}}}\omega\sqrt{\epsilon_{\text{eff},1}\mu_0}}{k_{\text{tr,z}}} = \frac{-\omega\mu_0}{k_{\text{tr,z}}}, \tag{C.5}$$

and for TM component

$$Z = \zeta_1\cos\theta_{\text{in}}\frac{\epsilon_{\text{eff},1}}{\epsilon_{\text{eff},2}}\frac{k_{\text{tr,z}}}{k_{\text{in,z}}} = -\zeta_1\frac{\epsilon_{\text{eff},1}}{\epsilon_{\text{eff},2}}\frac{k_{\text{tr,z}}}{k_1} = -\sqrt{\frac{\mu_0}{\epsilon_{\text{eff},1}}}\frac{\epsilon_{\text{eff},1}}{\epsilon_{\text{eff},2}}\frac{k_{\text{tr,z}}}{\omega\sqrt{\epsilon_{\text{eff},1}\mu_0}} = -\frac{k_{\text{tr,z}}}{\epsilon_{\text{eff},2}\omega}. \tag{C.6}$$

We know that $k_2 = \omega\sqrt{\epsilon_{\text{eff},2}\mu_0}$ and $k_1 = \omega\sqrt{\epsilon_{\text{eff},1}\mu_0}$. Thus end up with

$$k_{\text{tr,z}} = \omega\sqrt{\mu_0}\sqrt{\epsilon_{\text{eff},2} - \epsilon_{\text{eff},1}\sin^2\theta_{\text{in}}}, \tag{C.7}$$

Thus, for TE component

$$Z = \frac{-\omega\mu_0}{\omega\sqrt{\mu_0}\sqrt{\epsilon_{\text{eff},2} - \epsilon_{\text{eff},1}\sin^2\theta_{\text{in}}}} = -\sqrt{\frac{\mu_0}{\epsilon_{\text{eff},2} - \epsilon_{\text{eff},1}\sin^2\theta_{\text{in}}}}, \tag{C.8}$$

and for TM component

$$Z = -\frac{\omega\sqrt{\mu_0}\sqrt{\epsilon_{\text{eff},2} - \epsilon_{\text{eff},1}\sin^2\theta_{\text{in}}}}{\epsilon_{\text{eff},2}\omega} = \frac{\sqrt{\mu_0(\epsilon_{\text{eff},2} - \epsilon_{\text{eff},1}\sin^2\theta_{\text{in}})}}{\epsilon_{\text{eff},2}}. \tag{C.9}$$

Appendix D

2D discrete mixed Fourier transforms and propagators

In this section, the discrete mixed Fourier transform and propagators in 2D split-step Fourier method with an impedance ground is detailed. Both the direct, inverse spectral transforms, and the propagators are introduced. The configuration and discretization is the same as in section 1.7.3.

D.1 Spectral transform

A variable substitution from the field u to w is performed. For $p_z = \{1, \dots, N_z - 1\}$,

$$w_{p_r,p_z} = \frac{u_{p_r,p_z+1} - u_{p_r,p_z-1}}{2\Delta z} + \alpha u_{p_r,p_z}, \tag{D.1}$$

with $w_{p_r,p_z} = w(r_0 + p_r\Delta r, p_z\Delta z)$.

Doing so, the impedance boundary condition on u can be replaced by a Dirichlet condition on w.

The spectral transform DMFT is defined by [32]

$$\begin{aligned} W_{p_r,0} &= Q \sum_{p_z=0}^{N_z}{}' \gamma^{p_z} u_{p_r,p_z}, \\ W_{p_r,q_z} &= \sum_{p_z=1}^{N_z-1}{}' \sin\left(\tfrac{\pi q_z p_z}{N_z}\right) w_{p_r,p_z}, \text{ for } q_z = \{1, \dots, N_z - 1\}, \\ W_{p_r,N_z} &= Q \sum_{p_z=0}^{N_z}{}' (-1/\gamma)^{p_z} u_{p_r,p_z}, \end{aligned} \tag{D.2}$$

with the prime superscript on the sum indicates that the first and last terms are weighted with a coefficient 1/2.

Furthermore, for TM polarization, γ is defined as

$$\gamma = \sqrt{1 + (\alpha\Delta z)^2} - \alpha\Delta z, \tag{D.3}$$

where α has a positive real part. For TE polarization

$$\gamma = -\sqrt{1 + (\alpha\Delta z)^2} - \alpha\Delta z, \tag{D.4}$$

where α has a negative real part. Note that γ and $-1/\gamma$ are the roots of the quadratic equation

$$\gamma^2 + 2\alpha\Delta z\gamma - 1 = 0. \tag{D.5}$$

This choice of γ guaranties that $|\gamma|$ is less than 1. This avoids the singularities on the expression of Q, defined by

$$Q = \frac{2(1-\gamma^2)}{(1+\gamma^2)(1-\gamma^{2N_z})}. \tag{D.6}$$

Notice here that W_{p_r,q_z} for $q_z = \{1, \ldots, N_z - 1\}$ corresponds to the space wave. The terms $W_{p_r,0}$ and W_{p_r,N_z} correspond to the surface waves propagating on the top and ground boundaries. Both the space and surface waves are propagated by multiplying the spectral propagators derived in section 1.7.3.c.

D.2 Spectral propagators

The propagators for the space and surface waves of DSSF-DMFT and SSF-DMFT in 2D are derived in this subsection.

D.2.1 Spectral propagator of DSSF-DMFT

In DSSF-DMFT, the spectral propagators are based on the discrete propagation equation with $n = 1$, given by

$$\frac{\partial^2 u_{r,p_z}}{\partial r^2} - 2jk_0\frac{\partial u_{r,p_z}}{\partial r} + \mathbf{d}_z^2 u_{r,p_z} = 0, \tag{D.7}$$

with $u_{r,p_z} = u(r, p_z\Delta z)$ and $\mathbf{d}_z^2$ defined in (G.12).

The corresponding propagation operator is $\mathbf{P}_{\mathrm{m}}^{\mathrm{d}}$, satisfying

$$W_{p_r+1,\bullet}^{\mathrm{p}} = \mathbf{P}_{\mathrm{m}}^{\mathrm{d}} W_{p_r,\bullet}, \tag{D.8}$$

which is explicitly given by

$$W_{p_r+1,q_z}^{\mathrm{p}} = P_{\mathrm{m}}^{\mathrm{d}}[q_z] W_{p_r,q_z}. \tag{D.9}$$

The propagator $P_{\mathrm{m}}^{\mathrm{d}}[q_z]$, with $q_z = \{1, \ldots, N_z - 1\}$, represents the propagators of the space waves. In addition, $P_{\mathrm{m}}^{\mathrm{d}}[0]$ and $P_{\mathrm{m}}^{\mathrm{d}}[N_z]$ represent the propagators of the surface waves. They are developed as follows.

- Space waves:

For the space wave, since w satisfies the Dirichlet ground condition at the boundaries, the propagator $P_{\mathrm{m}}^{\mathrm{d}}[q_z]$ for w with $q_z = \{1, \ldots, N_z - 1\}$ is the same as the one for u of DSSF-DST given in Section 1.5.2. It is given by

$$P_{\mathrm{m}}^{\mathrm{d}}[q_z] = \exp\left(-j\Delta r\left(\sqrt{k_0^2 - (k_z^{\mathrm{d}})^2} - k_0\right)\right), \tag{D.10}$$

with $\mathrm{Im}\left(\sqrt{k_0^2 - (k_z^{\mathrm{d}})^2}\right) \leq 0$ and

$$k_z^{\mathrm{d}} = \frac{2}{\Delta z}\sin\left(\frac{\pi q_z}{2N_z}\right). \tag{D.11}$$

- Surface waves:

  The surface wave terms $W_{p_r,0}\gamma^{p_z}$ and $W_{p_r,N_z}(-1/\gamma)^{p_z}$ satisfy the discrete propagation equation. After inserting them in (D.7) and solving, the surface wave propagators are given by

$$\begin{aligned} P_{\mathrm{m}}^{\mathrm{d}}[0] &= \exp\left\{-j\Delta x\left(\sqrt{k_0^2 + \tfrac{\gamma+\gamma^{-1}-2}{\Delta z^2}} - k_0\right)\right\}, \\ P_{\mathrm{m}}^{\mathrm{d}}[N_z] &= \exp\left\{-j\Delta x\left(\sqrt{k_0^2 + \tfrac{(-\gamma)+(-\gamma)^{-1}-2}{\Delta z^2}} - k_0\right)\right\}. \end{aligned} \tag{D.12}$$

D.2.2 Spectral propagators of SSF-DMFT

In SSF-DMFT, the spectral propagators are based on the continuous propagation equation with $n = 1$, given by

$$\frac{\partial^2 u(r,z)}{\partial r^2} - 2jk_0\frac{\partial u(r,z)}{\partial r} + \frac{\partial^2 u(r,z)}{\partial z^2} = 0. \tag{D.13}$$

.

The corresponding propagation operator is $\mathbf{P}_{\mathrm{m}}$, satisfying

$$W_{p_r+1,\bullet}^{\mathrm{p}} = \mathbf{P}_{\mathrm{m}} W_{p_r,\bullet}, \tag{D.14}$$

The propagated spectrum $W_{p_r+1,q_z}^{\mathrm{p}}$ with $q_z = \{0, \ldots, N_z\}$ for Δr is given by

$$W_{p_r+1,q_z}^{\mathrm{p}} = P_{\mathrm{m}}[q_z] W_{p_r,q_z}. \tag{D.15}$$

Indeed, their values are as follows:

- Space waves:

  For the space wave, since w satisfies the Dirichlet ground condition at the boundaries, the propagator $P_{\mathrm{m}}[q_z]$ for w with $q_z = \{1, \ldots, N_z - 1\}$ is given by

$$P_{\mathrm{m}}[q_z] = \exp\left(-j\Delta r\left(\sqrt{k_0^2 - k_z^2} - k_0\right)\right), \tag{D.16}$$

  with $\mathrm{Im}\left(\sqrt{k_0^2 - k_z^2}\right) \leq 0$ and

$$k_z = \frac{\pi q_z}{z_{\max}}. \tag{D.17}$$

- Surface waves:

  According to DMFT-SSF [32], $W_{p_r,0}\gamma^{z/\Delta z}$ and $W_{p_r,N_z}(-1/\gamma)^{z/\Delta z}$ satisfy the continuous propagation equation (D.13). Thus, we have

$$\begin{aligned} P_{\mathrm{m}}[0] &= \exp\left\{-\tfrac{j\Delta x}{2k_0\Delta z^2}\left(\ln\gamma\right)^2\right\}, \\ P_{\mathrm{m}}[N_z] &= \exp\left\{-\tfrac{j\Delta x}{2k_0\Delta z^2}\left(\ln(-\gamma)\right)^2\right\}. \end{aligned} \tag{D.18}$$

D.3 Inverse spectral transform

After the propagation, $w^{\mathrm{p}}_{p_r+1,p_z}$ with $p_z = \{1,\ldots,N_z-1\}$ is obtained by applying the inverse sine transform to $W^{\mathrm{p}}_{p_r+1,q_z}$.

We retrieve $u^{\mathrm{p}}_{p_r+1,p_z}$ from $w^{\mathrm{p}}_{p_r+1,p_z}$, $W^{\mathrm{p}}_{p_r+1,0}$ and $W^{\mathrm{p}}_{p_r+1,N_z}$ by the method introduced as follows.

As an ordinary differential equations, the solution of (D.1) is a combination of a particular solution $\hat{u}_{p_r+1,p_z}$ of the inhomogeneous equation and an appropriate linear combination of the general solutions to the homogeneous equation.

$$u^{\mathrm{p}}_{p_r+1,p_z} = \hat{u}_{p_r+1,p_z} + B_1\gamma^{p_z} + B_2(-1/\gamma)^{p_z}, \tag{D.19}$$

with $p_z = \{0,\ldots,N_z\}$ and $\hat{u}_{p_r+1,p_z}$ is the particular solution of (1.68). Besides,

$$\begin{aligned} B_1 &= W^{\mathrm{p}}_{p_r+1,0} - Q\sum_{p_z=0}^{N}{}'\hat{u}_{p_r+1,p_z}\gamma^{p_z} \\ B_2 &= W^{\mathrm{p}}_{p_r+1,N_z} - Q\sum_{p_z=0}^{N}{}'\hat{u}_{p_r+1,p_z}(-1/\gamma)^{p_z} \end{aligned}. \tag{D.20}$$

A simple way to obtain $\hat{u}_{p_r+1,p_z}$ is to set $\hat{u}_{p_r+1,0} = \hat{u}_{p_r+1,N_z} = 0$ and to solve the resulting system of equations with a double pass method, decomposing the corresponding matrix (which is deduced by the Equation (1.68)) into the product of upper and lower triangular factors. The first pass is given by

$$\eta_{p_z} - \gamma\eta_{p_z-1} = 2w^{\mathrm{p}}_{p_r+1,p_z}\Delta z \quad \text{for} \quad p_z = \{1,\ldots,N-1\}, \tag{D.21}$$

with $\eta_0 = 0$.
The second pass is given by the backward recursion

$$\hat{u}_{p_r+1,p_z+1} + \frac{1}{r}\hat{u}_{p_r+1,p_z} = \eta_{p_z} \quad \text{for} \quad p_z = \{N_z-1,\ldots,0\}, \tag{D.22}$$

with $\hat{u}_{p_r+1,N_z} = 0$.

Using this transform, the propagated field $u^{\mathrm{p}}_{p_r+1,p_z}$ is obtained.

Appendix E

Approximation for the Hankel functions with large arguments

In this section, the objective is to simplify (2.7) and replace the Hankel function by the exponential function. In this way, the computation time is significantly reduced while keeping a good accuracy.

For κ is fixed and $|k_r r| \to \infty$, the Hankel function can be simplified to reduce the computation load, as

$$H_\kappa^{(2)}(z) \approx \sqrt{\frac{2}{\pi z}} \exp\left(-j(z - \frac{1}{2}\kappa\pi - \frac{1}{2}\pi)\right). \tag{E.1}$$

Doing so, the spectral propagation from r_0 to r becomes

$$\tilde{\Psi}(r) \approx \exp(-jk_r(r - r_0))\tilde{\Psi}(r_0). \tag{E.2}$$

A more accurate approximation can also be used [102]. When κ is fixed and $|z| \to \infty$, we have

$$H_\kappa^{(2)}(z) \approx \sqrt{\frac{2}{\pi z'}} \exp\left(-j\left(z' - \frac{1}{2}\kappa\pi - \frac{1}{2}\pi + \kappa \arctan\left(\frac{\kappa}{z'}\right)\right)\right), \tag{E.3}$$

with $z' = \sqrt{z^2 - \kappa^2}$ and $-2\pi < \arg z < \pi$. This method is valid for the case where $z > \kappa$ and has less error.

Thus, the spectral propagation from r_0 to r becomes

$$\begin{aligned}\tilde{\Psi}(r) \approx \exp\Bigg(- j\Bigg(\sqrt{k_r^2 r^2 - \kappa^2} - k_r\sqrt{k_r^2 r_0^2 - \kappa^2} + \kappa \arctan\left(\frac{\kappa}{\sqrt{k_r^2 r^2 - \kappa^2}}\right) \\ -\kappa \arctan\left(\frac{\kappa}{\sqrt{k_r^2 r_0^2 - \kappa^2}}\right)\Bigg)\Bigg)\tilde{\Psi}(r_0).\end{aligned} \tag{E.4}$$

The propagator with Hankel functions is approximated by the exponential functions when the arguments are larger. Since the computation load of the Hankel function is heavy, this approximation alleviate the burden.

Notice here, when the order and argument of the Hankel function are both large, the previous approximations are no longer valid. In this case, other approximations, notably using Airy functions, could be developed. This is left as future work.

Appendix F

3D DMFT in cylindrical coordinates

The methods for considering the propagation in 3D cylindrical coordinates are presented. The first method 3D-SSF-DMFT is widely used by the community. However, it has an inconsistency between the spectral transform and the propagator. The second one is a self-consistent discrete method, 3D-DSSF-DMFT.

F.1 Numerical scheme

The numerical scheme for the propagation over an impedance ground from r_{p_r} to r_{p_r+1} is as follows:

1. Apply a discrete Fourier transform on θ on the potential $\Psi_{r_{p_r}}$. The spectrum of the potential along θ is achieved, denoted as $\bar{\Psi}_{r_{p_r}}$, where $\bar{\Psi}_{r_{p_r}} = \{\bar{\Psi}_{r_{p_r},p_z,q_\theta}\}$ with $p_z \in \{0,\dots,N_z\}$ and $q_\theta \in \{0,\dots,N_\theta-1\}$. In addition, $\bar{\Psi}_{p_r,p_z,q_\theta} = \bar{\Psi}(r_{p_r}, p_z\Delta z, q_\theta)$
2. Apply DMFT along z on $\bar{\Psi}$ by the following steps:
   (a) Compute $w_{p_r} = \{w_{p_r,1,q_\theta},\dots,w_{p_r,N_z-1,q_\theta}\}$, such that

$$w_{p_r,p_z,q_\theta} = \frac{\bar{\Psi}_{p_r,p_z+1,q_\theta} - \bar{\Psi}_{p_r,p_z-1,q_\theta}}{2\Delta z} + \alpha\bar{\Psi}_{p_r,p_z,q_\theta} \tag{F.1}$$

   for $q_z \in \{1,\dots,N_z-1\}$.
   (b) Compute the spectrum $\tilde{\Psi}_{p_r}$ of w_{p_r}, which includes the space wave component $\tilde{\Psi}_{p_r,q_z,q_\theta}$ with $q_z = \{1,\dots,N_z-1\}$ and the surface waves $\tilde{\Psi}_{p_r,0,q_\theta}$, $\tilde{\Psi}_{p_r,N_z,q_\theta}$.

$$\begin{aligned}
\tilde{\Psi}_{p_r,0,q_\theta} &= Q\sum_{p_z=0}^{N_z}{}' r^{p_z}\bar{\Psi}_{p_r,p_z,q_\theta},\\
\tilde{\Psi}_{p_r,q_z,q_\theta} &= \sum_{p_z=1}^{N_z-1} w_{p_r,p_z,q_\theta}\sin\left(\tfrac{\pi q_z p_z}{N}\right), q_z = \{1,\dots,N_z-1\},\\
\tilde{\Psi}_{p_r,N_z,q_\theta} &= Q\sum_{p_z=0}^{N_z}{}' (-r)^{N-p_z}\,\bar{\Psi}_{p_r,p_z,q_\theta}.
\end{aligned} \tag{F.2}$$

3. Propagation in the spectral domain:
   (a) For $q_z = \{1, \ldots, N_z - 1\}$, $\tilde{\Psi}_{p_r,q_z,q_\theta}$ are propagated by means of multiplying the spectral propagator as derived in sections G.2.3 and 2.3.3.
   (b) The surface wave terms $\tilde{\Psi}_{p_r,0,q_\theta}$, $\tilde{\Psi}_{p_r,N_z,q_\theta}$ are propagated by multiplying the propagator as derived in (F.8) (3D-DSSF-DMFT) or (F.13) (3D-SSF-DMFT).
4. Retrieve $\bar{\Psi}^{\mathrm{p}}_{p_r+1}$ from $\tilde{\Psi}^{\mathrm{p}}_{p_r+1}$ as described for the DMFT algorithm as in Appendix D.
5. Apply an inverse discrete Fourier transform along θ on $\bar{\Psi}^{\mathrm{p}}_{p_r+1}$. Hence, the propagated potential $\Psi^{\mathrm{p}}_{p_r+1}$ is obtained.
6. Refractivity is considered in the spatial domain by the phase screens method.
7. Apodization and irregular relief are considered in the spatial domain.

With this scheme, we can simulate the 3D propagation over an impedance ground in the cylindrical coordinates.

F.2 Formulation of the 3D-DSSF-DMFT

F.2.1 Discrete propagation equation in vacuum

The 3D wave equation discretized on θ and z in the cylindrical coordinates are given by

$$\frac{\partial^2 \Psi}{\partial r^2} + \frac{1}{r^2}\mathbf{d}_\theta^2 \Psi + \mathbf{d}_z^2 \Psi + \left(k_0^2 + \frac{1}{4r^2}\right)\Psi = 0, \tag{F.3}$$

with

$$\begin{aligned} \mathbf{d}_z^2 \Psi_{p_r,p_z,p_\theta} &= \frac{1}{\Delta z^2}(\Psi_{p_r,p_z+1,p_\theta} - 2\Psi_{p_r,p_z,p_\theta} + \Psi_{p_r,p_z-1,p_\theta}), \\ \mathbf{d}_\theta^2 \Psi_{p_r,p_z,p_\theta} &= \frac{1}{\Delta \theta^2}(\Psi_{p_r,p_z,p_\theta+1} - 2\Psi_{p_r,p_z,p_\theta} + \Psi_{p_r,p_z,p_\theta-1}). \end{aligned} \tag{F.4}$$

F.2.2 Diagonalization on θ of the 3D wave equation

A discrete Fourier transform on θ is applied on (F.10). The spectrum of Ψ is denoted as $\bar{\Psi}$. This yields

$$\frac{\partial^2 \bar{\Psi}}{\partial r^2} - \frac{\kappa_{q_\theta}^2}{r^2}\bar{\Psi} + \mathbf{d}_z^2 \bar{\Psi} + \left(k_0^2 + \frac{1}{4r^2}\right)\bar{\Psi} = 0, \tag{F.5}$$

with

$$\kappa_{q_\theta} = \frac{2}{\Delta\theta}\sin\left(\frac{\pi q_\theta}{N_\theta}\right) \text{ for } q_\theta = \{0, ..., N_\theta - 1\}. \tag{F.6}$$

F.2.3 Propagation of surface waves

$\tilde{\Psi}_{p_r,0,q_\theta}\gamma^{q_z}$ and $\tilde{\Psi}_{p_r,N_z,q_\theta}(-\frac{1}{\gamma})^{q_z}$ satisfy (F.5). Hence, this yields

$$\begin{aligned} r^2\frac{\partial^2\tilde{\Psi}_{p_r,0,q_\theta}}{\partial r^2}+\left(r^2\left(k^2+\frac{\gamma+\gamma^{-1}-2}{(\Delta z)^2}\right)-\kappa_{q_\theta}^2\right)\tilde{\Psi}_{p_r,0,q_\theta}+\frac{1}{4}\tilde{\Psi}_{p_r,0,q_\theta}=0,\\ r^2\frac{\partial^2\tilde{\Psi}_{p_r,N_z,q_\theta}}{\partial r^2}+\left(r^2\left(k^2+\frac{\gamma+\gamma^{-1}-2}{(\Delta z)^2}\right)-\kappa_{q_\theta}^2\right)\tilde{\Psi}_{p_r,N_z,q_\theta}+\frac{1}{4}\tilde{\Psi}_{p_r,N_z,q_\theta}=0. \end{aligned} \tag{F.7}$$

Thus, the propagations of $\tilde{\Psi}_{p_r,0,q_\theta}$ and $\tilde{\Psi}_{p_r,N_z,q_\theta}$ from distance r_{p_r} to r_{p_r+1} is realized by multiplications with the propagators od the surface waves, which are given by

$$\begin{aligned} P^{\mathrm{d}}_{\mathrm{f,m}}[p_r,0,q_\theta]&=\frac{H^{(2)}_{\kappa_{q_\theta}}(k_{\mathrm{sw}_1}r_{p_r+1})}{H^{(2)}_{\kappa_{q_\theta}}(k_{\mathrm{sw}_1}r_{p_r})}\sqrt{\frac{r_{p_r+1}}{r_{p_r}}},\\ P^{\mathrm{d}}_{\mathrm{f,m}}[p_r,N_z,q_\theta]&=\frac{H^{(2)}_{\kappa_{q_\theta}}(k_{\mathrm{sw}_2}r_{p_r+1})}{H^{(2)}_{\kappa_{q_\theta}}(k_{\mathrm{sw}_2}r_{p_r})}\sqrt{\frac{r_{p_r+1}}{r_{p_r}}}, \end{aligned} \tag{F.8}$$

where

$$\begin{aligned} k_{\mathrm{sw}_1}&=\sqrt{k_0^2+(\gamma+\gamma^{-1}-2)/(\Delta z)^2},\\ k_{\mathrm{sw}_2}&=\sqrt{k_0^2+((-\gamma)+(-\gamma)^{-1}-2)/(\Delta z)^2}. \end{aligned} \tag{F.9}$$

F.3 Formulations of 3D-SSF-DMFT

F.3.1 Continuous wave equation and diagonalization on θ

The propagation of the potential Ψ in the boundary satisfies the 3D continuous wave equation in the cylindrical coordinates

$$\frac{\partial^2\Psi}{\partial r^2}+\frac{1}{r^2}\frac{\partial^2\Psi}{\partial\theta^2}+\frac{\partial^2\Psi}{\partial z^2}+\left(k_0^2+\frac{1}{4r^2}\right)\Psi=0. \tag{F.10}$$

To derive the spectral wave equation along θ, a discrete Fourier transform on θ is applied on (F.10). The spectrum of Ψ is denoted as $\bar{\Psi}$. This yields

$$\frac{\partial^2\bar{\Psi}}{\partial r^2}-\frac{q_\theta^2}{r^2}\bar{\Psi}+\frac{\partial^2\bar{\Psi}}{\partial z^2}+\left(k_0^2+\frac{1}{4r^2}\right)\bar{\Psi}=0. \tag{F.11}$$

where $q_\theta=\{0,\ldots,N_{\theta-1}\}$. Then, DMFT is applied on $\bar{\Psi}$.

F.3.2 Propagation of surface waves

$\tilde{\Psi}_{p_r,0,q_\theta}\gamma^{\frac{z}{\Delta z}}$ and $\tilde{\Psi}_{p_r,N_z,q_\theta}(-\frac{1}{\gamma})^{\frac{z}{\Delta z}}$ satisfy (F.11). Hence, this yields

$$\begin{aligned} r^2\frac{\partial^2\tilde{\Psi}_{p_r,0,q_\theta}}{\partial r^2}+\left(r^2\left(k^2+\frac{(\ln\gamma)^2}{(\Delta z)^2}\right)-q_\theta^2\right)\tilde{\Psi}_{p_r,0,q_\theta}+\frac{1}{4}\tilde{\Psi}_{p_r,0,q_\theta}=0,\\ r^2\frac{\partial^2\tilde{\Psi}_{p_r,N_z,q_\theta}}{\partial r^2}+\left(r^2\left(k^2+\frac{(\ln(-\gamma))^2}{(\Delta z)^2}\right)-q_\theta^2\right)\tilde{\Psi}_{p_r,N_z,q_\theta}+\frac{1}{4}\tilde{\Psi}_{p_r,N_z,q_\theta}=0. \end{aligned} \tag{F.12}$$

Thus, the propagators for $\tilde{\Psi}_{p_r,0,q_\theta}$ and $\tilde{\Psi}_{p_r,N_z,q_\theta}$ from distance r_{p_r} to r_{p_r+1} are given by

$$\begin{aligned} P_{\mathrm{f,m}}[p_r,0,q_\theta]&=\frac{H^{(2)}_{q_\theta}(k_{\mathrm{sw}_1}r_{p_r+1})}{H^{(2)}_{q_\theta}(k_{\mathrm{sw}_1}r_{p_r})}\sqrt{\frac{r_{p_r+1}}{r_{p_r}}},\\ P_{\mathrm{f,m}}[p_r,N_z,q_\theta]&=\frac{H^{(2)}_{q_\theta}(k_{\mathrm{sw}_2}r_{p_r+1})}{H^{(2)}_{q_\theta}(k_{\mathrm{sw}_2}r_{p_r})}\sqrt{\frac{r_{p_r+1}}{r_{p_r}}}, \end{aligned} \tag{F.13}$$

where

$$\begin{aligned} k_{\mathrm{sw}_1}&=\sqrt{k_0^2+(\ln\gamma)^2/(\Delta z)^2},\\ k_{\mathrm{sw}_2}&=\sqrt{k_0^2+(\ln(-\gamma))^2/(\Delta z)^2}. \end{aligned} \tag{F.14}$$

Appendix G

Summary in French (Résumé français)

G.1 Formulation Auto-Cohérente de la Méthode 2D Split-Step Fourier dans le Domaine Discret

G.1.1 Introduction

G.1.1.a État de l'art

Parabolic equation (PE) methods are among the most reliable numerical methods to simulate the propagation in an inhomogeneous atmosphere. They are based on an approximation of the wave equation valid along a paraxial direction and neglecting backward propagation [23].

The two most used methods for applying PE are based on the finite-difference (FD) method [29] and the split-step Fourier (SSF) method [30]. The FD method has the advantage of a straightforward implementation of complex boundaries. However, SSF is more numerically efficient because it permits larger mesh increments. Consequently, SSF is widely used for long-range wave propagation. The computation is performed marching on in distance. At each step, the wave is transformed from the spatial to the spectral domain by applying a spectral transform along the vertical.

Refractivity, ground boundary condition, and irregular relief can be considered in SSF. The phase-screens method is applied to take into account the refractivity in the spatial domain [12]. The relief can be modeled by various algorithms [12][31][67][68].

A spectral transform consistent with the boundary condition is chosen to consider the ground composition. A perfectly conducting ground is accounted by a sine or cosine transform depending on the polarization. A dielectric ground is approximated by an impedance boundary condition. Then, to model the propagation over an impedance

ground, the discrete mixed Fourier transform (DMFT) has been proposed by Dockery and Kuttler [32].

G.1.1.b Auto-cohérence: motivation pour une formulation discrète

Le concept de la théorie électromagnétique auto-cohérente sur une grille régulière a été développée par Chew [65]. Les formes discrètes de nombreux théorèmes électromagnétiques ont été dérivées. La préservation de ces théorèmes implique que l'utilisation de cette forme discrétisée des équations de Maxwell pour la simulation numérique ne donneront pas de solutions parasites.

Notre but est de modéliser la propagation dans une atmosphère inhomogène sur un sol impédant avec un relief irrégulier. SSF-DMFT est classiquement utilisée [32]. Dans SSF-DMFT, la transformée DMFT est basée sur une approximation de différence-finie pour la condition au sol. Mais le propagateur est dérivé de l'équation de propagation continue. Ceci est une incohérence dans cette méthode qui peut conduire à des solutions fausses.

Pour éviter cette incohérence, une formulation discrète de SSF-DMFT est proposée, notée DSSF-DMFT. La transformée spectrale et le propagateur sont tous dérivés à partir d'équations discrètes. Par conséquent, il est auto-cohérent.

Ce travail correspond au contenu de Zhou *et al.* [1] [2].

G.1.2 Configuration

In this chapter, we are concerned with a 2D problem. The 3D problem is reduced to 2D by assuming an invariance along y in Cartesian coordinates or an azimuthal invariance along θ in cylindrical coordinates.

The problem is firstly treated in cylindrical coordinates. The propagation is performed in a 2D vertical plane with the coordinates system (r, z). The wave propagation is along the direction $+r$. The case in Cartesian coordinates will be introduced afterwards.

We work at a given frequency $f = \omega/2\pi$. The $\exp(j\omega t)$ time-dependence of the field is omitted. The field is assumed to be known at $r = r_0$. The propagation is computed in the region $r > r_0, z \geq 0$, as illustrated in Fig. G.1.

An inhomogeneous atmosphere is considered. The atmospheric characteristic is represented by the refractive index n. Because n is close to 1, it is convenient to use N, defined by

$$N = 10^6 \times (n - 1). \tag{G.1}$$

The refractivity N can be expressed from the Smith-Weintraub equation [69]

$$N = \frac{77.6}{T}\left(P + 4810\frac{e}{T}\right), \tag{G.2}$$

with P the atmosphere pressure (hPa), e the water pressure (hPa), and T the absolute temperature (K). This expression may be used for radio frequencies up to 100 GHz with errors smaller than 0.5%.

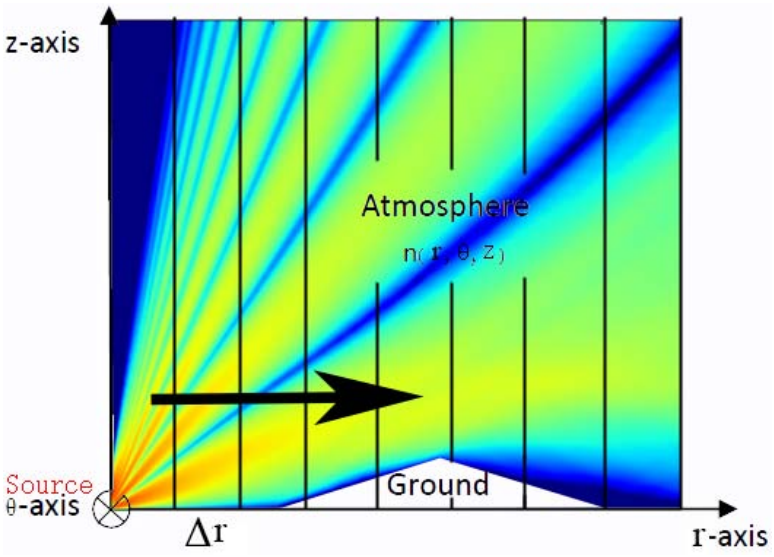

Figure G.1: Split-step Fourier method.

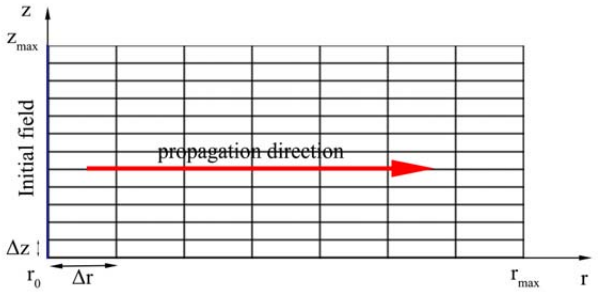

Figure G.2: Discrétisation de 2D-SSF.

To account for the Earth's curvature, an Earth flattening transform can also be applied. This can be done by replacing N by the modified refractivity M [70]. For various places on Earth, parametric descriptions of M exist [15]. They are often used as an input of the propagation model. These models and the modified refractivity are both introduced in Appendix A.

The configuration has been described. We will now introduce the continuous formulation of the split-step Fourier (SSF) method for simulating the wave propagation.

G.1.3 Discrétisation

Pour des raisons numériques, le domaine vertical est discrétisé en r et z et de taille finie. Les conséquences sont triples. D'abord, une apodisation est nécessaire pour enlever la réflexion de la limite supérieure. Deuxièmement, la transformée discrète est appliquée. Enfin, un propagateur discret est dérivé des formulations discrètes. La propagation sur un terrain PEC est ici présentée.

Le domaine vertical est limité à $z \in [0, z_{\max}]$ et la propagation est simulé de r_0 à $r_{\max}$. La grille uniforme suivante est utilisée

$$\begin{array}{lll} r = r_0 + p_r \Delta r & \text{for} & p_r = \{0, ..., N_r\}, \\ z = p_z \Delta z & \text{for} & p_z = \{0, ..., N_z\}, \end{array} \tag{G.3}$$

avec $\Delta r = (r_{\max} - r_0)/N_r$, et $\Delta z = z_{\max}/N_z$. Cette grille est illustrée à la Fig. G.2. Le champ $u(p_r \Delta r, r_0 + p_z \Delta z)$ est représenté par u_{p_r, p_z}.

Remarquons ici que $u_{p_r,0} = 0$ et $u_{p_r,N_z} = 0$ en raison de la condition PEC aux frontières.

G.1.4 Apodisation

Dans ce travail, une apodisation est appliquée avec une fenêtre Hanning sur la moitié supérieure de la zone de calcul. Cela équivaut à une multiplication terme à terme représentée par un opérateur **H**, défini par

$$\mathbf{H}: \quad u_{p_r,p_z} \longrightarrow H[p_z] u_{p_r,p_z}, \tag{G.4}$$

avec

$$H[p_z] = \begin{cases} 1 & \text{for } p_z \in [0, N_z/2], \\ \frac{1+\cos(\pi(\frac{2p_z\Delta z}{z_{\max}}-1))}{2} & \text{for } p_z \in [N_z/2, N_z]. \end{cases} \tag{G.5}$$

G.1.5 Formulation discrète de la SSF

On définit une variable appropriée représentant le champ scalaire, noté Ψ, avec laquelle, en coordonnées cylindriques, la diminution du champ dans $1/\sqrt{k_0 r}$ est supprimée. L'expression de Ψ est donnée par

- Pour le composant TE:

$$\Psi(r, z) = \sqrt{k_0 r} E_\theta(r, z). \tag{G.6}$$

- Pour le composant TM:

$$\Psi(r, z) = \sqrt{k_0 r} H_\theta(r, z). \tag{G.7}$$

Dans un milieu d'indice de réfraction $n = n(r, z)$, l'onde scalaire spatiale $\Psi(r, z)$ est décrite par l'équation de Helmholtz scalaire bidimensionnelle, telle que

$$\nabla^2 \Psi(r, z) + k_0^2 n^2 \Psi(r, z) = 0, \tag{G.8}$$

avec $\nabla^2 = \frac{\partial^2}{\partial r^2} + \frac{1}{r}\frac{\partial}{\partial r^2} + \frac{\partial^2}{\partial z}$ et $k_0 = \omega/c_0$ le nombre d'onde dans le vide.

Pour propager une onde le long de la direction $+r$, un champ réduit u est donné par

$$u(r, z) = e^{jk_0 r} \Psi(r, z). \tag{G.9}$$

Ce champ varie lentement en distance.

Substitution de (G.9) dans (G.8) donne

$$\frac{\partial^2 u(r,z)}{\partial r^2} - 2jk_0\frac{\partial u(r,z)}{\partial r} + \frac{\partial^2 u(r,z)}{\partial z^2} + k_0^2(n(r,z)^2 - 1)u(r,z) = 0. \tag{G.10}$$

Dans le domaine discret, l'opérateur différentiel le long de z (G.10) est remplacé par le opérateur à différence finie. La contrepartie discrète de l'équation de Helmholtz appliquée à le champ réduit u est

$$\frac{\partial^2 u_{p_z}}{\partial r^2} - 2jk_0\frac{\partial u_{p_z}}{\partial r} + d_z^2 u_{p_z} + k_0^2(n_{r,p_z}^2 - 1)u_{p_z} = 0, \tag{G.11}$$

avec $u_{p_z} = u(r, r_0 + p_z\Delta z)$ et $n_{r,p_z} = n(r, r_0 + p_z\Delta z)$. Le terme d_z^2 est l'approximation de la différence centrale du second ordre, donnée par

$$d_z^2 u_{p_z} = \frac{1}{\Delta z^2}(u_{p_z+1} - 2u_{p_z} + u_{p_z-1}). \tag{G.12}$$

Une condition PEC est supposée aux limites $z = 0$ et $z = z_{\max}$. La transformée spectrale correspond alors à une transformée discrète en sinus (DST), notée $\mathbf{T}_\mathrm{s}$, défini par

$$U_{p_r,q_z} = \mathbf{T}_\mathrm{s} u_{p_r,p_z} = \frac{1}{\sqrt{N_z+1}} \sum_{p_z=1}^{N_z-1} u_{p_r,p_z} \sin\left(\pi\frac{p_z q_z}{N_z}\right), \tag{G.13}$$

avec $q_z \in [1, N_z - 1]$.

L'objectif est de dériver le propagateur spectral adapté à la formulation discrète. Après avoir appliqué la transformation spectrale discrète (G.13) à (G.11) en supposant n constant, l'équation de propagation spectrale dans un milieu homogène est dérivée. L'équation de propagation spectrale dans une atmosphère homogène est

$$\frac{\partial^2 U_{r,q_z}}{\partial r^2} - 2jk_0\frac{\partial U_{r,q_z}}{\partial r} - \frac{4\sin^2\left(\frac{\pi q_z}{2N_z}\right)}{\Delta z^2} U_{r,q_z} = 0, \tag{G.14}$$

avec $U_{r,q_z} = U(r, q_z\Delta k_z)$.

En suivant la méthode pour séparer les propagations en avant et en arrière, l'équation de propagation spectrale vers l'avant est donnée par

$$\left(\frac{\partial}{\partial r} + j\left(\sqrt{k_0^2 - (k_{q_z}^z)^2} - k\right)\right) U_{r,q_z} = 0, \tag{G.15}$$

avec $q_z = \{1, \ldots, N_z - 1\}$ et

$$k_{q_z}^z = \frac{2}{\Delta z}\sin\left(\frac{\pi q_z}{2N_z}\right), \tag{G.16}$$

La propagation de $r_0 + p_r\Delta r$ à $r_0 + (p_r + 1)\Delta r$ est

$$U_{p_r+1,q_z} = P_{q_z} U_{p_r,q_z}, \tag{G.17}$$

avec $U_{p_r,q_z} = U(r_0 + p_r\Delta r, q_z\Delta k_z)$. Le propagateur P est donné par

$$P_{q_z} = \exp\left\{-j\Delta r\left(k^r_{q_z} - k_0\right)\right\}, \tag{G.18}$$

avec

$$k^r_{q_z} = \begin{cases} \sqrt{k_0^2 - (k^z_{q_z})^2} & \text{if } k_0^2 - (k^z_{q_z})^2 \geq 0, \\ -j\sqrt{(k^z_{q_z})^2 - k_0^2} & \text{if } k_0^2 - (k^z_{q_z})^2 < 0. \end{cases} \tag{G.19}$$

La formulation discrète de SSF est dénotée comme DSSF.

G.1.6 Propagation sur un sol impédant

Pour simuler une propagation sur un terrain impédant, la méthode SSF-DMFT développée par Dockery *et al.* [32] est introduite. Une incohérence entre la transformée spectrale et la propagateur est souligné. Par conséquent, nous proposons une méthode auto-cohérente dans le domaine discret, notée DSSF-DMFT. La formulation est dérivée de l'équation discrète, similaire à celle de la DSSF.

G.1.7 Modélisation du relief irrégulier

Le relief irrégulier peut être considéré par différents modèles. La solution la plus simple est de modéliser les pentes par des marches d'escalier. L'opérateur de modélisation du relief est désignée par **L**.

G.1.8 Schéma de simulation de la propagation

La propagation sur un sol PEC de r à $r + \Delta r$ est simulée comme

$$u(r + \delta r, z) = \mathbf{LHRT}_{\mathrm{s}}{}^{-1}\mathbf{PT}_{\mathrm{s}}u(r, z). \tag{G.20}$$

avec **R** est l'opérateur appliquant la méthode d'écrans de phase.

Il est répété itérativement pour des distances de plus en plus grandes pour simuler la propagation à longue distance.

G.1.9 Simulations numériques

G.1.9.a Propagation sur un sol sec

Dans ce test, nous simulons la propagation sur un terrain impédant plan. Nous comparons les résultats de simulation de SSF-DMFT et DSSF-DMFT au modèle à deux rayons.

Un point source complexe (CSP) [76] est utilisé comme source de l'onde. La source est localisée à une position complexe (x_s, y_x, z_s) avec $x_s \in \mathbf{C}$ tel que $x_s = x_{w0} + jkW_0^2/2$. Son

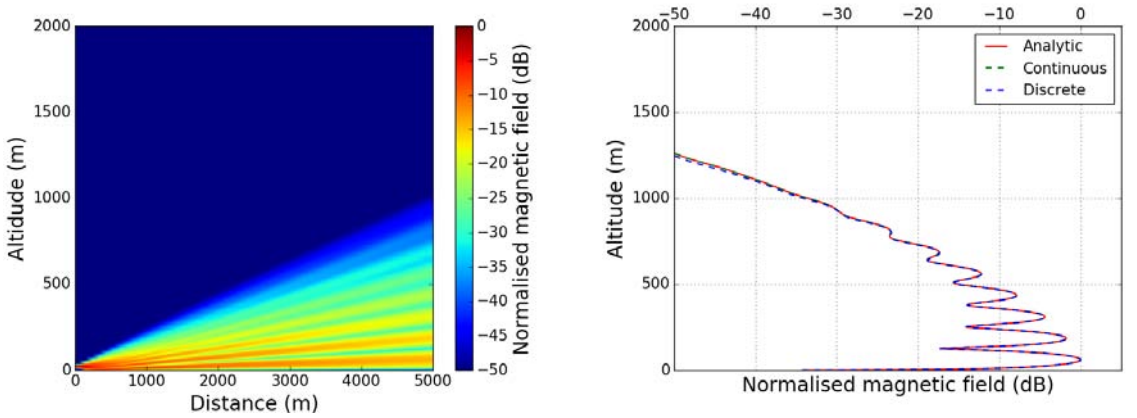

(a) Propagation utilisant DSSF-DMFT (b) Comparaison du champ final électrique

Figure G.3: Propagation d'une source complexe 2D sur un sol sec.

rayonnement peut être obtenu analytique au moyen de la fonction de 2D / 3D Green. Les résultats de simulation de SSF et DSSF sont comparés à la solution analytique du CSP.

Les paramètres du CSP sont: fréquence $f = 300$ MHz, $z_s = 20$ m, $x_{w0} = -50$ m, et $W_0 = 3$ m (3λ). Les paramètres de la simulation sont les suivants: $r_{\max}$ is 5000 m, Δx is 100 m, $z_{\max} = 4000$ m, et $\Delta z = 0.2$ m.

La propagation de DSSF-DMFT est représentée sur Fig. G.3a. La réflexion est bien simulée. Les champs finaux des SSF-DMFT, DSSF-DMFT et du modèle à 2-rayons sont représentés sur Fig. G.3b. Les résultats de SSF-DMFT, DSSF-DMFT sont les mêmes que ceux du modèle à 2-rayons.

G.1.9.b Propagation sur un sol très sec

Nous choisissons maintenant un sol très sec avec une permittivité relative $\epsilon_r = 2$ et une conductivité $\sigma = 0.001$ S/m. Les autres paramètres sont les mêmes que dans le test précédent.

La propagation en utilisant SSF-DMFT est montrée sur Fig. G.4a. Le champ a une oscillation parasite. Le résultat de DSSF-DMFT est montré dans Fig. G.4b. Le résultat reste précis. Il simule la propagation aussi précisément que le modèle 2-rayons.

La comparaison des champs électriques finaux est montrée sur Fig G.4c. Les champs électriques finaux du modèle DSSF-DMFT et du modèle à 2-rayons sont les mêmes avec une erreur acceptable. SSF-DMFT a beaucoup d'oscillations parasites.

L'intérêt de DSSF-DMFT par rapport à SSF-DMFT est que DSSF-DMFT est une méthode auto-cohérente dans le domaine discret. Ainsi, comme le montre notre test, il évite les problèmes numériques parasites qui peuvent survenir dans certaines conditions.

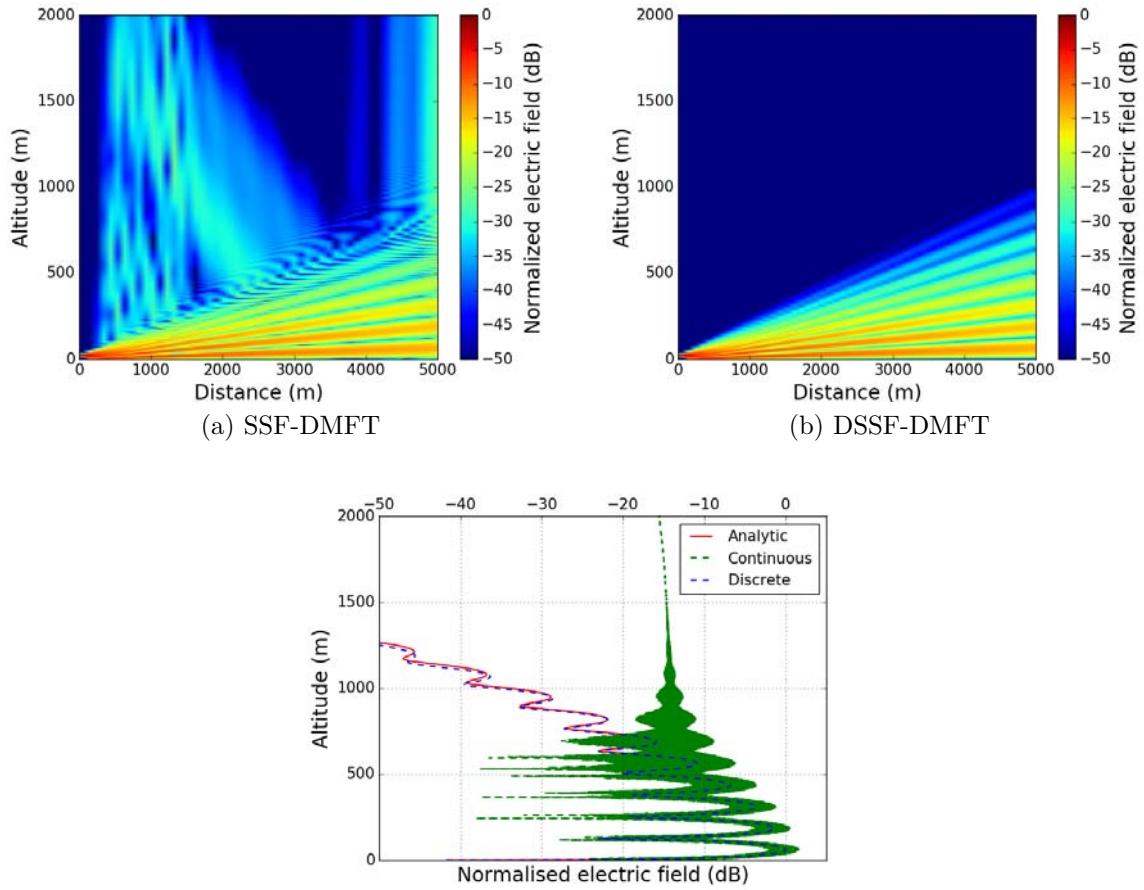

(a) SSF-DMFT

(b) DSSF-DMFT

(c) Comparaison des champs électriques finaux

Figure G.4: Propagation d'une source complexe 2D sur un sol très sec pour 5000 m.

G.1.10 Conclusion

Dans ce chapitre, les méthodes de modélisation d'une propagation à longue distance avec un relief irrégulier dans une atmosphère inhomogène ont été introduites.

Nous proposons une formulation discrète, nommée DSSF. La méthode est basée sur l'équation de propagation discrète.

Ensuite, la condition du sol de l'impédance discrète est supposée. SSF-DMFT est une méthode efficace pour modéliser la propagation sur un terrain d'impédance. Son propagateur est dérivé de l'équation continue. Cependant, la transformée spectrale est dérivée de la discrète. Cette incohérence a été mise en évidence. Par conséquent, une méthode auto-cohérente a été introduite, nommée DSSF-DMFT.

Des expériences numériques ont été effectuées. Pour la propagation sur un sol impédant, SSF-DMFT a des oscillations parasites dans certaines conditions, tandis que DSSF-DMFT reste précis. En effet, DSSF-DMFT est auto-cohérent et évite les instabilités numériques.

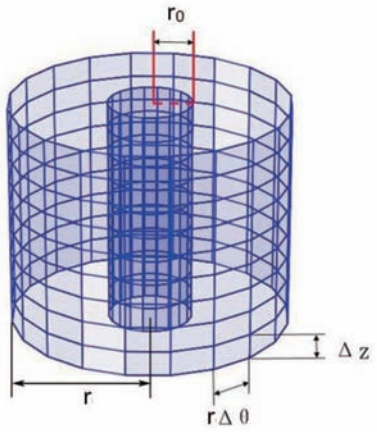

Figure G.5: Grille le long de z et θ sur le cylindre initial à la distance r_0 et sur un cylindre à distance $r > r_0$.

G.2 Méthode Split-Step Fourier Discrète en 3D

La méthode split-step Fourier discrète en 3D basé sur une représentation spectrale exacte de l'équation de propagation est proposée. Cette formulation est d'une plus grande précision que l'équation parabolique. De plus, l'algorithme proposé en coordonnées cylindriques est plus cohérent avec la propagation radar que ceux en coordonnées cartésiennes.

Ce chapitre correspond au contenu de Zhou *et al.*[3] [4] [5].

G.2.1 Configuration

Le système de coordonnées cylindriques est utilisé avec les vecteurs unitaires $(\hat{\boldsymbol{r}}, \hat{\boldsymbol{\theta}}, \hat{\boldsymbol{z}})$. Nous supposons que les sources sont situées dans le cylindre $r \leq r_0$ et que les champs sont connus à $r = r_0$. Un sol plan parfaitement métallique et infini est situé à $z = 0$. La propagation est calculée dans la région, $r > r_0$, $z \geqslant 0$.

Pour des raisons numériques évidentes, le domaine de calcul est discrétisé et de taille finie.

Le domaine vertical est limité à $z \in [0, z_{\max}]$ et la grille uniforme suivante est utilisée

$$\begin{array}{lll} z = p_z \Delta z & \text{for} & p_z = \{0, ..., N_z\}, \\ \theta = p_\theta \Delta\theta & \text{for} & p_\theta = \{0, ..., N_\theta - 1\}, \end{array} \tag{G.21}$$

avec $\Delta z = z_{\max}/N_z$ et $\Delta\theta = 2\pi/N_\theta$. La grille est montrée sur la Fig. G.5.

Le potentiel $\Psi(r_0 + p_r\Delta r, p_z\Delta z, p_\theta\Delta\theta)$ est noté $\Psi[p_r, p_z, p_\theta]$.

À $z_{\max}$, nous supposons une condition de conduction parfaite. Par conséquent, le problème est simplifié comme la propagation dans un guide d'onde. Les potentiels tels que $p_z = 0$ et $p_z = N_z$ sont des zéros. Ainsi, le potentiel $\Psi(r_0 + p_r\Delta r, p_z\Delta z, p_\theta\Delta\theta)$ avec $p_z = \{1, ..., N_z - 1\}$ est considéré.

Dans une étape préliminaire, un indice de réfraction homogène, *i.e.* n constant, est considéré.

G.2.2 Potentiels de Hertz

Les champs peuvent être décomposés en une composante électrique transversale (TE) et une composante magnétique transversale (TM) par rapport à z au moyen des potentiels de Hertz orientés selon $\hat{\boldsymbol{z}}$. Pour le champ électrique, en omettant la dépendance en temps $e^{j\omega t}$, on a

$$\boldsymbol{E} = k_0^2 n^2 \boldsymbol{\Pi}_\mathrm{e} + \boldsymbol{\nabla}\boldsymbol{\nabla}\cdot\boldsymbol{\Pi}_\mathrm{e} - k_0\zeta_0 n \boldsymbol{\nabla}\times\boldsymbol{\Pi}_\mathrm{h}, \tag{G.22}$$

où $\boldsymbol{\Pi}_\mathrm{e}$ et $\boldsymbol{\Pi}_\mathrm{h}$ sont les potentiels vectoriels électrique et magnétique, k_0 est le nombre d'onde en espace libre, et ζ_0 est l'impédance de l'espace libre. Enfin, remplacer $\boldsymbol{\Pi}_\mathrm{e}$ par $\frac{\Psi}{\sqrt{r}}\hat{\boldsymbol{z}}$ donne le champ électrique TM

$$\begin{aligned}\boldsymbol{E} =& \frac{\partial}{\partial r}\left(r^{-\frac{1}{2}}\frac{\partial}{\partial z}\Psi\right)\hat{\boldsymbol{r}} + r^{-\frac{3}{2}}\frac{\partial^2\Psi}{\partial z\partial\theta}\hat{\boldsymbol{\theta}} \\ &+ \left(r^{-\frac{1}{2}}\frac{\partial^2\Psi}{\partial z^2} + k_0^2 n^2\Psi\right)\hat{\boldsymbol{z}}.\end{aligned} \tag{G.23}$$

Notons que le cas TE peut être formulé de la même manière à partir d'un potentiel magnétique $\boldsymbol{\Pi}_\mathrm{h} = \frac{\Psi}{\sqrt{r}}\hat{\boldsymbol{z}}$. La principale différence est une expression différente du champ électrique.

G.2.3 Formulation discrète dans une atmosphère homogène

Dans cette section, nous proposons une formulation discrète du propagateur spectral pour atteindre l'auto-cohérence. La formulation est basée sur l'équation de propagation discrète.

G.2.3.a Équation discrète

Pour obtenir la contrepartie discrète de l'équation de propagation en 3D, les dérivées spatiales de second ordre par rapport à θ et z sont discrétisées sur les points intérieurs de la grille en utilisant l'approximation de différences finies centrées. Cela donne

$$\frac{\partial^2\Psi_{p_z,p_\theta}}{\partial r^2} + \frac{1}{r^2}d_\theta^2\Psi_{p_z,p_\theta} + d_z^2\Psi_{p_z,p_\theta} + \left(k_0^2n^2 + \frac{1}{4r^2}\right)\Psi_{p_z,p_\theta} = 0, \tag{G.24}$$

avec

$$\begin{aligned} d_z^2\Psi_{p_z,p_\theta} &= \frac{1}{\Delta z^2}(\Psi_{p_z+1,p_\theta} - 2\Psi_{p_z,p_\theta} + \Psi_{p_z-1,p_\theta}), \\ d_\theta^2\Psi_{p_z,p_\theta} &= \frac{1}{\Delta\theta^2}(\Psi_{p_z,p_\theta+1} - 2\Psi_{p_z,p_\theta} + \Psi_{p_z,p_\theta-1}), \end{aligned} \tag{G.25}$$

où $\Psi_{p_z,p_\theta} = \Psi(r, p_\theta\Delta\theta, p_z\Delta z)$.

G.2.3.b Représentation spectrale discrète

Pour rendre notre représentation spectrale numériquement cohérente, nous partons directement de (G.24). L'application de la transformée spectrale en z et θ donne

$$r^2\frac{\partial^2\tilde{\Psi}}{\partial r^2} + (r^2k_r^2[q_z] - \kappa^2[q_\theta])\tilde{\Psi} + \frac{1}{4}\tilde{\Psi} = 0, \tag{G.26}$$

où

$$\kappa[q_\theta] = \frac{2}{\Delta\theta}\sin\left(\frac{\pi q_\theta}{N_\theta}\right) \text{ for } q_\theta = \{0, ..., N_\theta - 1\}, \tag{G.27}$$

et $k_r^2[q_z] = k_0^2n^2 - k_z^2[q_z]$ avec

$$k_z[q_z] = \frac{2}{\Delta z}\sin\left(\frac{\pi q_z}{2N_z}\right) \text{ for } q_z = \{1, ..., N_z - 1\}. \tag{G.28}$$

Dans une atmosphère homogène, le champ peut être propagé de r_{p_r} à r_{p_r+1} dans le domaine spectral. En effet, la solution analytique de (G.26) est [80]

$$\tilde{\Psi}_{p_r+1,q_z,q_\theta} = \frac{H^{(2)}_{\kappa[q_\theta]}(k_r[q_z]r_{p_r+1})}{H^{(2)}_{\kappa[q_\theta]}(k_r[q_z]r_{p_r})}\sqrt{\frac{r_{p_r+1}}{r_{p_r}}}\tilde{\Psi}_{p_r,q_z,q_\theta} \tag{G.29}$$

où $H^{(2)}_{\kappa[q_\theta]}$ indique la fonction de Hankel du second type et de l'ordre $\kappa[q_\theta]$.

Cette équation est similaire à la propagation d'harmoniques cylindriques à l'exception des expressions de k_r et κ à cause de la formulation discrète. Quand $q_\theta \ll N_\theta$, *i.e.* pour les modes variant lentement avec θ, l'ordre de la fonction de Hankel devient un entier ($\kappa \approx q_\theta$).

G.2.4 Schéma numérique

Comme pour les autres méthodes split-step [12], le calcul est effectué itérativement en distance. Entre deux cylindres consécutifs, nous propageons le potentiel à travers un milieu homogène à l'aide du propagateur spectral. Ensuite, nous appliquons un écran de phase pour tenir compte des variations de l'indice de réfraction.

A chaque itération p_r, la propagation, l'apodisation et l'indice de réfraction local sont considérés en utilisant les 5 étapes décrites ci-dessous:

1. Le potentiel Ψ sur le cylindre à la distance $r_0 + p_r\Delta r$ est exprimé dans le domaine spectral au moyen de la transformée $\mathbf{T}_\mathrm{s}$.

2. Le spectre est multiplié par l'opérateur spectral $\mathbf{P}_{p_r,q_\theta,q_z}$ représentant la propagation de r_{p_r} à r_{p_r+1} donné par

$$\mathbf{P}_{p_r,q_\theta,q_z} = \frac{H^{(2)}_\kappa(k_r r_{p_r+1})}{H^{(2)}_\kappa(k_r r_{p_r})}\sqrt{\frac{r_{p_r+1}}{r_{p_r}}}. \tag{G.30}$$

3. Le potentiel est exprimé dans le domaine spatial avec la transformation ${\mathbf{T}_\mathrm{s}}^{-1}$.

4. Pour supprimer les réflexions sur la limite supérieure, une apodisation est appliquée avec une fenêtre Hanning sur la moitié supérieure du domaine. Cela équivaut à une multiplication terme à terme représentée par un opérateur diagonal $\mathbf{H}$.

5. Un écran de phase est appliqué qui correspond à une multiplication par

$$R[p_r, p_\theta, p_z] = \exp\left(jk_0(n_{p_r,p_\theta,p_z} - 1)\Delta r\right), \tag{G.31}$$

où n_{p_r,p_θ,p_z} est l'indice de réfraction à la position $(p_r\Delta r, p_\theta\Delta\theta, p_z\Delta z)$. Le terme de réfraction peut être vu comme une perturbation du cas homogène.

Pour conclure, la propagation de r_{p_r} à r_{p_r+1} est simulée étape par étape

$$\Psi_{p_r+1} = \mathbf{H}\mathbf{R}{\mathbf{T}_\mathrm{s}}^{-1}\mathbf{P}\mathbf{T}_\mathrm{s}\Psi_{p_r} \tag{G.32}$$

où $\mathbf{H}$, $\mathbf{R}$, et $\mathbf{P}$ sont des opérateurs diagonaux, *i.e.* des multiplications par terme.

La complexité de calcul finale de cette méthode est de l'ordre $N_r N_\theta N_z \log_2 N_\theta \log_2 N_z$.

Dans la dernière étape, le champ est calculé à partir des potentiels. Pour ce faire, le spectre de champ est obtenu à partir du spectre potentiel en appliquant (G.23) dans le domaine spectral. En effet, les dérivées sont plus faciles à calculer dans le domaine spectral. Finalement, ${\mathbf{T}_\mathrm{s}}^{-1}$ est appliqué pour obtenir les potentiels.

G.2.5 Méthode de propagation en 3D sur un sol d'impédance

Pour simuler la propagation sur un sol impédant, la méthode discrete mixed Fourier transform (DMFT) est utilisée. Cette méthode, initialement développée en 2D, est ici étendue en 3D.

L'extension en 3D de DMFT est décrite comme suit:

1. Sur θ, la transformée spectrale est une DFT. Le spectre de Ψ est noté $\bar{\Psi}$.

2. Sur z, la DMFT est appliquée à $\bar{\Psi}$ comme en 2D.

3. La propagation de r à $r + \Delta r$ est calculée en multipliant les propagateurs des ondes spatiales et de surface.

4. Sur z, la DMFT inverse est effectuée. $\bar{\Psi}$ est récupéré.

5. Enfin, une DFT inverse le long de θ est effectuée pour obtenir le potentiel propagé Ψ.

Les propagateurs des ondes spatiales et de surface sont dérivés soit par des équation continues (3D-SSF-DMFT), soit par des équation discrètes (3D-DSSF-DMFT). Comme en 2D, 3D-DSSF-DMFT est auto-cohérente dans le domaine discret.

G.2.6 Test numérique

L'objectif de la simulation est de vérifier que la méthode 3D proposée permet de modéliser les effets verticaux et azimutaux. Au contraire, les méthodes N×2D ne peuvent pas prendre en compte les effets latéraux.

Un scénario complexe avec des effets 3D dans les directions verticale et azimutale est présenté. Nous considérons un modèle d'indice de réfraction identique dans les deux directions avec 2 conduits sur z et θ. Par conséquent, des effets similaires sont attendus dans les deux directions.

L'indice de réfraction dans le plan z/θ est obtenu par $M = \sqrt{M_z M_\theta}$, où M_z et M_θ sont des fonctions associées à l'indice de réfractivité modifié le long de z et θ. Dans la direction verticale, nous considérons un conduit de surface, qui est modélisé par une fonction trilinéaire M_z, comme illustré dans Fig. G.6a.

Les paramètres sont: $M_0 = 330$ M-units, $z_b = 950$ m, $z_t = 100$ m, $z_{\max} = 2000$ m, gradients $c_0 = 0.118$ M-units/m, $c_2 = -1.0$ M-units/m. Dans la direction azimutale, nous utilisons le même modèle mappé en coordonnées cylindriques. De telles variations d'indice d'azimut ne sont pas réalistes dans la troposphère, mais sont utilisées pour comparer l'effet 3D en θ et z. Enfin, l'indice de réfractivité modifié sur le plan z/θ est obtenu. Le gradient est représenté sur la Fig. G.6b.

Pour la simulation, la fréquence est de 3 GHz. La source complexe est à une altitude de 1000 m avec $W_0 = 1$ m. Les paramètres de simulation sont: $r_0 = 2$ km, $r_{\max} = 12$ km, $\Delta r = 500$ m, $z_{\max} = 2000$ m, $\Delta z = 0.2$ m, et $N_\theta = 30000$.

Des résultats similaires sont attendus le long des 2 directions puisque les conduits sont les mêmes le long des 2 axes. Le champ électrique normalisé obtenu à la distance $r_{\max} = 12$ km est représenté sur la Fig. G.7. Nous pouvons voir les effets 3D dus aux 2 conduits le long des directions azimutale et verticale. La valeur maximale du champ final est située à $63,0$ m du centre dans la direction verticale et à $62,8$ m dans la direction azimutale. Les 2 valeurs sont les mêmes à une erreur près acceptable.

Pour comparaison, avec la méthode N × 2D, seuls les effets verticaux sont comptabilisés dans ce cas.

G.2.7 Conclusion

La méthode de propagation en 3D dans les coordonnées cylindriques basée sur la méthode split-step Fourier a été introduite.

Premièrement, une atmosphère homogène a été considérée pour exprimer le problème au moyen de potentiels de Hertz. Une formulation discrète de la propagation en 3D a été présentée. Un propagateur spectral discret a été dérivé.

Deuxièmement, un schéma numérique explicite pour considérer une réfractivité variant lentement a été introduit. La méthode d'écran de phase est appliquée dans le domaine spatial.

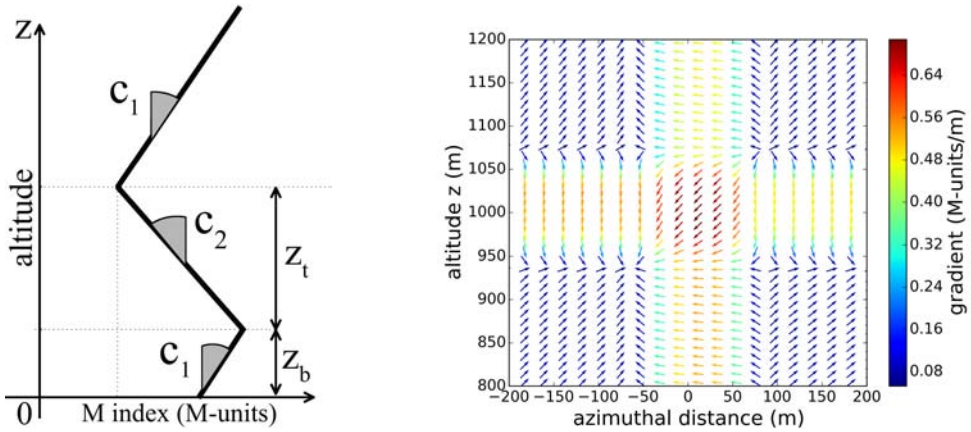

(a) Modèle trilinéaire de conduits à base de surface.

(b) Gradients vecteurs de réfractivité (M-units/m) sur le plan $z - \theta$

Figure G.6: Modèles de réfractivité.

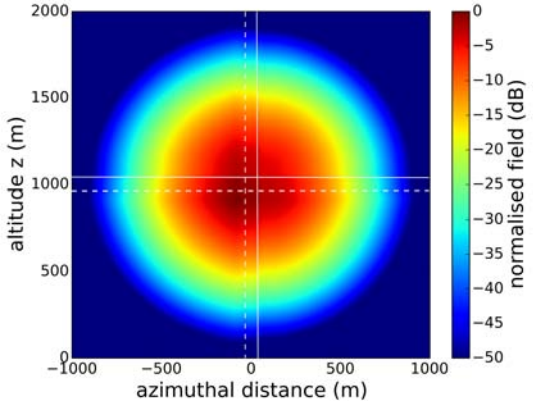

Figure G.7: Champ final de la simulation utilisant 3D-DSSF.

Considérant un sol plan impédant, la méthode 2D-SSF-DMFT a été étendue en 3D. Ensuite, les formulations continues et discrètes pour le propagateur ont été présentées, nommée 3D-SSF-DMFT et 3D-DSSF-DMFT, respectivement. 3D-SSF-DMFT est une extension naturelle de 2D-SSF-DMFT. Cependant, une incohérence de cette méthode a été mise en évidence. Ensuite, 3D-DSSF-DMFT a été proposée pour atteindre l'auto-cohérence dans le domaine discret.

Enfin, un scénario avec des effets 3D complexes dans les directions verticale et azimutale a été introduit. Nous avons considéré les conditions de réfractivité avec 2 conduits atmosphériques le long des directions verticale et azimutale. Notons que les effets de réfraction ont été modélisés avec succès dans les deux directions. Cette méthode prend en compte les effets azimutaux qui sont un avantage sur les modèles $N \times 2D$.

G.3 Méthode Split-Step en Ondelettes

G.3.1 Introduction

Dans ce chapitre, nous introduisons une méthode alternative à SSF en 2D. Il est également basé sur la méthode split-step. La différence est que la transformée rapide en ondelettes (FWT) [96] est utilisée à la place de FFT. Il est désigné par la suite par la méthode "Split-Step Ondelettes" (SSW).

Les transformées en ondelettes sont utilisées, l'objectif principal étant de réduire le temps de calcul. La méthode SSW proposée est basée sur la FWT multirésolution le long de la verticale. Cela entraîne une complexité inférieure à celle de la FFT. De plus, la décomposition en ondelettes donne une représentation creuse du signal. La propagation est réalisée par une combinaison linéaire des ondelettes propagés individuellement. Ces propagations individuelles sont stockées en tant que données précalculées. L'objectif est de réduire le temps de calcul par rapport à la SSF tout en gardant une bonne précision.

Ce chapitre correspond au contenu de Zhou *et al.* [6].

La configuration et la discrétisation est le même que dans le section 1.

G.3.2 Formulation de le méthode split-step en ondelettes

G.3.3 Aperçu de la méthode

Basée sur la transformée en ondelettes et la compression, la méthode SSW est dérivée. La SSW est effectuée en allant et venant d'une représentation spatiale à une représentation en ondelettes de l'onde de manière à évaluer la propagation de manière itérative à des distances croissantes. La propagation de r à $r+\Delta r$, avec $r = p_r \Delta r$, est simulée étape par étape comme suit:

1. Le champ $u(r, p_z\Delta z)$ est représenté par un vecteur d'ondelettes creuses $U(r)$ après application de FWT (noté $\mathbf{W}$) et une compression (notée $\mathbf{C}$), tel que

$$U(r) = \mathbf{CW}u(r, \cdot). \tag{G.33}$$

2. La propagation est considérée dans le domaine des ondelettes. Les coefficients vectoriels $U_{\mathrm{p}}(r+\Delta r)$ après la propagation en espace libre sur Δr sont donnés par

$$U_{\mathrm{p}}(r+\Delta r) = \mathbf{M}U(r), \tag{G.34}$$

   où $\mathbf{M}$ est la matrice de propagation en espace libre précalculée qui modélise les propagations d'ondelettes.

   Les éléments de $\mathbf{M}$, *i.e.* $M_{(l,p),(l',p')}$ satisfont

$$U_{\mathrm{fs}(l,p)}(r+\Delta r) = \sum_{l',p'} M_{(l,p),(l',p')} U_{(l',p')}(r), \tag{G.35}$$

où (l', p') et (l, p) indice de la translation-dilatation des ondelettes situées à r et $r+\Delta r$, respectivement.

3. Le champ propagé $u_{\mathrm{p}}(r + \Delta r, z)$ est recomposé par IFWT (noté $\mathbf{W}^{-1}$) à partir des ondelettes propagées
$$u_{\mathrm{p}}(r + \Delta r, \cdot) = \mathbf{W}^{-1} U_{\mathrm{p}}(r + \Delta r). \tag{G.36}$$

4. L'apodisation, l'atmosphère et le relief sont appliqués dans le domaine spatial, représentés par les opérateurs $\mathbf{H}$, $\mathbf{R}$ et $\mathbf{L}$, respectivement.

En conclusion, la propagation de r à $r + \Delta r$ est simulée étape par étape par

$$u(r + \Delta r, \cdot) = \mathbf{HRLW}^{-1}\mathbf{MCW}u(r, \cdot). \tag{G.37}$$

G.3.4 Condition au sol PEC

Dans SSW, la théorie de l'image classique [97] pourrait être appliquée. Cette méthode double le domaine de calcul, un domaine image étant ajouté. le fardeau serait considérablement accru.

Pour pallier ce problème, nous introduisons un algorithme d'image locale avec une couche d'image plus mince qu'avec la théorie d'image classique, l'idée clé étant que le champ d'une couche image mince soit mis à jour par symétrie à chaque étape de propagation.

L'algorithme d'image locale est illustré dans Fig. G.8. Une condition aux limites PEC est appliquée en suivant ces étapes:

1. A la distance r, nous connaissons le champ u décrit sur N_z points, puis il est étendu à u_{t} en ajoutant une couche d'image locale sous u sur N_{im}. Le champ entier u_{t} est défini par
$$u_{\mathrm{t}}(r, p_z\Delta z) = \begin{cases} u(r, p_z\Delta z) & \text{for } p_z \in [1, N_z - 1], \\ 0 & \text{for } p_z = 0, \\ -u(r, -p_z\Delta z) & \text{for } p_z \in [-N_{\mathrm{im}}, -1]. \end{cases} \tag{G.38}$$

2. u_{t} est propagé de r à $r + \Delta r$ en utilisant la méthode SSW.

3. Le champ $u_{\mathrm{p}}(r + \Delta r, z)$ est obtenu comme
$$u_{\mathrm{p}}(r + \Delta r, p_z\Delta z) = u_{\mathrm{t}}(r + \Delta r, p_z\Delta z), \tag{G.39}$$
pour $p_z \in [1, N_z - 1]$.

Comme seule l'image du champ dans le voisinage proche du sol est utilisée, nous appelons cet algorithme *la méthode de l'image locale*.

En bas de la couche image, aucune apodisation n'est appliquée. Une réflexion parasite peut donc apparaître. Par conséquence, N_{im} est choisi pour que cette erreur n'atteigne

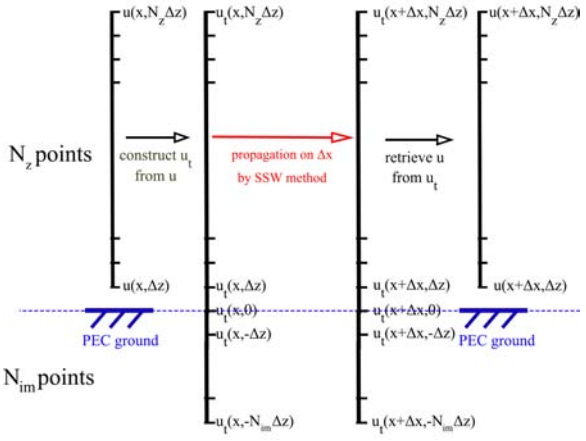

Figure G.8: Condition du terrain du conducteur électrique local parfait pour SSW.

pas le domaine d'intérêt (*i.e.*, $p_z > 0$). À chaque étape, le champ dans la couche image est mis à jour en utilisant (G.38). Ainsi, l'erreur dans la couche image est nettoyée à chaque étape et n'a jamais atteint ce domaine.

N_{im} est choisi supérieur à la largeur maximale des ondelettes après propagation sur Δr. Cette largeur est connue à l'avance lors de la création de la matrice $\mathbf{M}$. Une ondelette sur une étape Δr est beaucoup plus petite que le domaine de calcul total, $N_{\text{im}} \ll N_z$, ce qui rend la méthode d'image locale efficace.

G.3.5 Atmosphère et relief

Pour considérer une atmosphère variant lentement, la méthode des écrans de phase est appliquée au champ. Un relief irrégulier est considéré en utilisant un modèle de marches d'escalier exactement comme pour la SSF (cf. section G.1.7).

G.3.6 Comparaison de la complexité

Comparée à la méthode SSF classique, la transformée de Fourier est remplacée par la décomposition et la recomposition des ondelettes. À chaque étape en distance, La complexité de la FFT est en $O(N_z \log N_z)$. La complexité de la FWT est en $O(N_z + N_{\text{im}}) \approx O(N_z)$ car en pratique $N_{\text{im}} \ll N_z$.

La complexité de calcul de l'étape de propagation dans SSF est $O(N_z)$. La propagation dans SSW est donnée par la multiplication de $\mathbf{M}$ par U. Comme $\mathbf{M}$ et U sont creuses, le coût de multiplication effectif N_{e} est

Table G.1: Complexité computationnelle de SSW et SSF sur un pas Δx

	SSW	SSF
wavelet dec. / DFT	$O(N_z)$	$O(N_z \log N_z)$
propagation	$O(N_\mathrm{e})$	$O(N_z)$
wavelet rec. / IDFT	$O(N_z)$	$O(N_z \log N_z)$

$$\begin{aligned} N_\mathrm{e} &= \sum_{(l,p)\in\mathcal{I}_\mathrm{nz}(U)} \mathcal{N}_\mathrm{nz}\left(M_{(l,p),(\cdot,\cdot)}\right) \\ &\leq \underbrace{\max_{(l,p)}\left(\mathcal{N}_\mathrm{nz}\left(M_{(l,p),(\cdot,\cdot)}\right)\right)}_{N_M}\underbrace{\mathcal{N}_\mathrm{nz}(U)}_{N_\mathrm{s}}, \end{aligned} \tag{G.40}$$

où $\mathcal{I}_\mathrm{nz}$ et $\mathcal{N}_\mathrm{nz}$ donnent respectivement les indices et le nombre de coefficients non nuls dans un vecteur.

La complexité de cette étape dans SSW est $O(N_\mathrm{e})$ avec $N_\mathrm{e} \leq N_M N_\mathrm{s}$. Notez que, N_M et N_s sont beaucoup plus petits que N_z en raison du taux de compression élevé de la décomposition en ondelettes.

La comparaison des complexités de calcul de SSW et SSF pour une étape est présentée dans le tableau G.1 Avec un taux de compression (CR) élevé, SSW est plus rapide que SSF. Comme la complexité des algorithmes est linéaire avec N_r, les complexités totales sont obtenues en multipliant par N_r.

Pour le remplissage de la matrice de propagation $\mathbf{M}$, la complexité des propagations SSF est en $O(LN_z \log N_z)$, et la complexité des décompositions d'ondelettes est en $O(2^L N_z)$. Ils sont également négligeables par rapport à la complexité totale de SSW, qui est en $O(N_r N_z + N_r N_\mathrm{e})$ pour $N_r \gg 1$.

G.3.7 Tests numériques

Dans cette section, plusieurs tests numériques sont effectués pour valider la méthode SSW. Dans un premier temps, des tests de propagation sur un sol plan impédant avec des compressions de matrices et de signaux sont effectués. Enfin, une propagation à longue distance sur un relief irrégulier dans une atmosphère inhomogène est réalisée.

G.3.7.a Propagation sur un sol plan d'impédance dans une atmosphère homogène

Le but de cette section est de tester SSW avec un sol plan impédant avec $\epsilon_r = 20$ et $\sigma = 0.02$ S/m en utilisant la méthode de l'image locale.

Les paramètres du CSP sont: fréquence $f = 300$ MHz, $x_{\mathrm{w}0} = -50$ m, $y_\mathrm{s} = 0$ m, $z_\mathrm{s} = 30$ m, et $W_0 = 5$ m. Les paramètres de simulation sont $r_\mathrm{max} = 50$ km, $\Delta r = 100$ m,

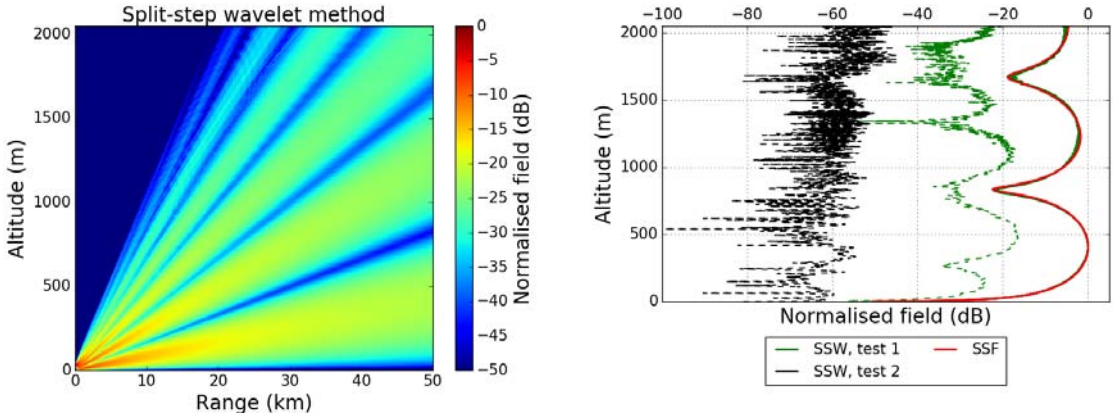

(a) Champ électrique normalisé dans le plan vertical obtenu avec SSW du test 1

(b) Champs électriques normalisés à l'étape finale obtenus par SSF et SSW (lignes complètes) et différences de SSW à SSF (lignes pointillées).

Figure G.9: Propagation sur un sol d'impédance d'un CSP avec $W_0 = 5$ m centré à 30 m.

Table G.2: Valeurs de seuils, CR, RMSE et comparaison de temps pour la propagation sur un sol plan d'impédance

SSW	test 1	test 2	SSF
V_{M}	2×10^{-4}	2×10^{-5}	
V_s	2×10^{-2}	2×10^{-3}	
CR de $\mathbf{M}$ (%)	93.4	85.7	
CR moyen de signal (%)	88.6	81.6	
Différence RMS avec SSF (dB)	-18.3	-52.8	
Temps (s)	9.1	9.3	14.2

$z_{\max} = 4096$ m, et $\Delta z = 1$ m. Ainsi, $N_r = 500$ et $N_z = 4096$. Les ondelettes choisies sont *symlets 6*, avec le niveau maximum $L = 3$.

Le schéma de propagation est représenté sur la Fig. G.9. Le modèle d'interférence réfléchi par le sol d'impédance est bien simulé. Les résultats de la simulation concernant taux de compression (CR), la différence RMS et le temps de calcul sont indiqués dans le tableau G.2. SSW avec un sol impédant est également testé avec succès.

G.3.7.b Propagation à longue distance sur un relief irrégulier d'impédance dans une atmosphère inhomogène

Dans cette partie, nous testons une propagation à longue distance sur un relief irrégulier dans une atmosphère inhomogène.

Dans la direction verticale, nous considérons un conduit de surface, qui est modélisé par une réfractivité trilinéaire modifiée. Les paramètres sont:$M_0 = 330$ M-units, $z_b = 100$ m, $z_t = 200$ m, $z_{\max} = 4096$ m, avec des gradients $c_0 = 0.118$ M-units/m, $c_2 = -0.1$ M-units/m.

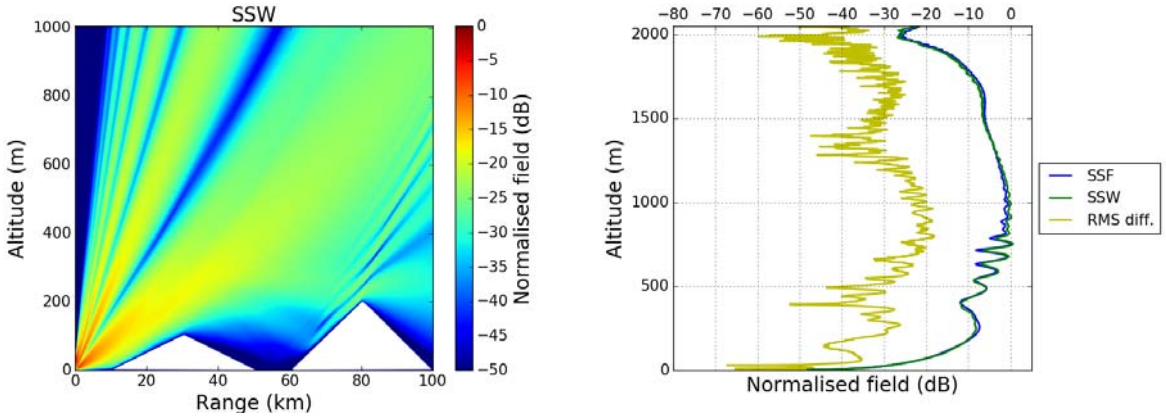

(a) Champ électrique normalisé (dB) obtenu par SSW.

(b) Champs électriques normalisés à l'étape finale obtenus par SSF et SSW et la différence SSW-SSF.

Figure G.10: Propagation sur une impédance planaire rectifiée dans une atmosphère inhomogène et sur un relief irrégulier.

Le relief est choisi comme 2 petites collines triangulaires de hauteur 100 m et 200 m. Les caractéristiques de l'impédance sont $\epsilon_r = 20$ et $\sigma = 0.02$ S/m.

Dans ce test, la plage de propagation est $x_{\max} = 100$ km. L'échelle est de 200 m, avec $N_x = 100$. Nous choisissons $V_{\mathrm{M}} = 2 \times 10^{-4}$ et $V_s = 2 \times 10^{-2}$.

La propagation en utilisant SSW dans le plan vertical est montrée sur Fig. G.10a. Les effets de réfraction du conduit de surface et la réflexion par le sol irrégulier sont correctement simulés, comme montée sur la Fig. G.10b.

La différence RMS du champ final de SSW à SSF est de $-21,6$ dB, ce qui fait que SSW fonctionne bien pour une simulation à longue distance sur un relief irrégulier dans une atmosphère inhomogène. Le temps de simulation avec SSW est de 15.1 s, ce qui prouve a une meilleure efficacité de calcul qu'avec SSF, même sur des scénarios complexes.

G.3.8 Conclusion

Sur la base de la transformée rapide en ondelettes (FWT) et de la compression de données, la méthode split-step ondelettes (SSW) pour la simulation de la propagation d'ondes électromagnétiques à longue distance a été introduite.

Dans un premier temps, la méthode SSW proposée a été introduite de manière exhaustive: le champ est représenté sous la forme d'un ensemble parcimonieux de coefficients après application de la FWT et du seuillage, puis propagé en espace libre au moyen d'une matrice de propagation pré-calculée.

Deuxièmement, en considérant un sol conducteur parfait, une méthode d'image locale a été proposée, puis cette méthode a été étendue à un sol d'impédance, et le relief irrégulier est également comptabilisé à chaque étape, le champ total étant obtenu de manière itérative.

Ensuite, la complexité de calcul de SSW a été comparée à SSF. SSW a un avantage dans l'efficacité de calcul en raison du taux de compression élevé de la décomposition en ondelettes et de la faible complexité de la transformée en ondelettes rapide.

Enfin, des tests numériques de propagation des ondes ont été présentés pour montrer la précision et l'efficacité de cette méthode. Des tests de propagation sur un sol plan impédant avec des compressions sur la matrice et les signaux ont été effectuées. L'erreur de SSW dépend des seuils et sa valeur est prévisible. SSW a une haute précision et une bonne efficacité de calcul par rapport à SSF. La méthode d'image locale a été testée avec succès. Enfin, une propagation à longue distance sur un relief irrégulier dans une atmosphère inhomogène a été réalisée. Le résultat de SSW montre un très bon match avec SSF. SSW fonctionne bien pour une propagation en distance longue avec un temps de calcul réduit.

Lists of my publications

[1] H. Zhou, A. Chabory, and R. Douvenot, "Comparisons of discrete and continuous propagators for the modelling of low tropospheric propagation," in *11th European Conference on Antennas and Propagation (EuCAP)*, 2017, pp. 1236–1238.

[2] ——, "Comparaison des propagateurs discret et continu pour la propagation dans la basse troposphère," in *20èmes Journées Nationales Micro-Ondes (JNM)*, 2017.

[3] ——, "A 3-D split-step Fourier algorithm based on a discrete spectral representation of the propagation equation," *IEEE Transactions on Antennas and Propagation*, vol. 65, no. 4, pp. 1988–1995, 2017.

[4] ——, "Comparisons of discrete and continuous propagators for simulating electromagnetic wave propagation in low troposphere in 3D," in *IEEE-APS Topical Conference on Antennas and Propagation in Wireless Communications (APWC)*, 2017, pp. 181–184.

[5] H. Zhou, R. Douvenot, and A. Chabory, "Comparison of Nx2D and 3D split-step Fourier methods in realistic 3D ducting conditions," in *International Applied Computational Electromagnetics Society Symposium (ACES)*, 2017, pp. 1–2.

[6] H. Zhou, A. Chabory, and R. Douvenot, "Modeling wave propagation by a wavelet-based split-step parabolic equation," *Journal of Computational Physics*, to be submitted, provisional title.

Bibliography

[7] *Annex 10 to convention on international civil aviation: Aeronautical telecommunications*, Sixth Edition, ICAO, 2006.

[8] L. Claudepierre, "Simulateur électromagnétique d'erreur VOR par méthodes déterministes : Application aux parcs éoliens," PhD thesis, INP Toulouse, 2015.

[9] L. Claudepierre, R. Douvenot, A. Chabory, and M. C., "A deterministic VOR error modeling method - application to wind turbines," *IEEE Transactions on Aerospace and Electronic Systems*, vol. 53, no. 1, pp. 247–257, 2017.

[10] B. R. Bean and E. J. Dutton, *Radio Meteorology*. Dover Publications, 1966.

[11] L. Barclay, *Propagation of Radiowaves*. LET, 2003.

[12] M. Levy, *Parabolic Equation Methods for Electromagnetic Wave Propagation*. IET editions, 2000.

[13] T. B. Senior and J. L. Volakis, *Approximate boundary conditions in electromagnetics*. IET editions, 1995.

[14] M. P. Hall, *Effects of the troposphere on radio communication*. Institution of Electrical Engineers, London, 1980.

[15] *Recommendation ITU P.834-9 (12/2017): Effects of tropospheric refraction on radiowave propagation*.

[16] J. G. Powers, J. B. Klemp, W. C. Skamarock, *et al.*, "The weather research and forecasting model: Overview, system efforts, and future directions," *Bulletin of the American Meteorological Society*, vol. 98, no. 8, pp. 1717–1737, 2017.

[17] A. Taflove and S. C. Hagness, *Computational Electrodynamics: the Finite-Difference Time-Domain Method*. Artech house, 2005.

[18] J.-M. Jin, *The Finite Element Method in Electromagnetics*. John Wiley & Sons, 2015.

[19] R. F. Harrington and J. L. Harrington, *Field Computation by Moment Methods*. Oxford University Press, 1996.

[20] C. Bourlier, N. Pinel, and G. Kubické, *Method of Moments for 2D Scattering Problems: Basic Concepts and Applications*. John Wiley & Sons, 2013.

[21] D. Bouche and F. Molinet, *Méthodes Asymptotiques en Electromagnétisme*. Springer, 1994.

[22] J. S. Asvestas, "The physical optics method in electromagnetic scattering," *Journal of Mathematical Physics*, vol. 21, no. 2, pp. 290–299, 1980.

[23] J. Kuttler and G. D. Dockery, "Theoretical description of the parabolic approximation/Fourier split-step method of representing electromagnetic propagation in the troposphere," *Radio Science*, vol. 26, no. 02, pp. 381–393, 1991.

[24] P. F. Goldsmith, *Quasioptical Systems: Gaussian Beam Quasioptical Propagation and Applications*. IEEE press New York, 1998.

[25] Y. A. Kravtsov, L. A. Ostrovsky, and N. S. Stepanov, "Geometrical optics of inhomogeneous and nonstationary dispersive media," *Proceedings of the IEEE*, vol. 62, no. 11, pp. 1492–1510, 1974.

[26] J. B. Keller, "Geometrical theory of diffraction," *Journal of the Optical Society of America*, vol. 52, no. 2, pp. 116–130, 1962.

[27] R. G. Kouyoumjian and P. H. Pathak, "A uniform geometrical theory of diffraction for an edge in a perfectly conducting surface," *Proceedings of the IEEE*, vol. 62, no. 11, pp. 1448–1461, 1974.

[28] M. A. Leontovich and V. A. Fock, "Solution of propagation of electromagnetic waves along Eearth's surface by the method of parabolic equations," *J. Phys. USSR*, vol. 10, pp. 13–23, 1946.

[29] A. V. Popov, "Solution of a parabolic equation of diffraction theory by a finite difference method," *USSR Computational Mathematics and Mathematical Physics*, vol. 8, no. 5, pp. 282–288, 1968.

[30] R. H. Hardin and F. D. Tappert, "Applications of the split-step Fourier method to the numerical solution of nonlinear and variable coefficient wave equations," *SIAM Review*, vol. 15, no. 1, pp. 423–429, 1973.

[31] A. E. Barrios, "A terrain parabolic equation model for propagation in the troposphere," *IEEE Transactions on Antennas and Propagation*, vol. 42, no. 1, pp. 90–98, 1994.

[32] G. D. Dockery and J. R. Kuttler, "An improved impedance-boundary algorithm for Fourier split-step solutions of the parabolic wave equation," *IEEE Transactions on Antennas and Propagation*, vol. 44, no. 12, pp. 1592–1599, 1996.

[33] W. L. Siegmann, G. A. Kriegsmann, and D. Lee, "A wide-angle three-dimensional parabolic wave equation," *Journal of the Acoustical Society of America*, vol. 78, no. 2, pp. 659–664, 1985.

[34] F. Sturm and J. A. Fawcett, "On the use of higher-order azimuthal schemes in 3-D PE modeling," *Journal of the Acoustical Society of America*, vol. 113, no. 6, pp. 3134–3145, 2003.

[35] F. Sturm, "Numerical study of broadband sound pulse propagation in three-dimensional oceanic waveguides," *Journal of the Acoustical Society of America*, vol. 117, no. 3, pp. 1058–1079, 2005.

[36] J. A. Fawcett, "Modeling three-dimensional propagtion in an oceanic wedge using parabolic equation methods," *Journal of the Acoustical Society of America*, vol. 93, no. 5, pp. 2627–2632, 1993.

[37] A. A. Zaporozhets and M. F. Levy, "Bistatic RCS calculations with the vector parabolic equation method," *IEEE Transactions on Antennas and Propagation*, vol. 47, pp. 1688–1696, 1999.

[38] R. Janaswamy, "Path loss predictions in the presence of buildings on flat terrain: A 3-D vector parabolic equation approach," *IEEE Transactions on Antennas and Propagation*, vol. 51, no. 8, pp. 1716–1728, 2003.

[39] A. Ginestet, "Modélisation de la propagation d'une onde electromagnétique sur des scènes de grande taille par résolution de l'equation parabolique 3D vectorielle," PhD thesis, Université Paul Sabatier-Toulouse III, 2007.

[40] H. Kogelnik and T. Li, "Laser beams and resonators," *Proceedings of the IEEE*, vol. 54, no. 10, pp. 1312–1329, 1966.

[41] J. T. Verdeyen, *Laser electronics*. Prentice Hall, 1989.

[42] D. Marcuse, *Light transmission optics*. Van Nostrand Reinhold New York, 1972.

[43] D. H. Martin and J. W. Bowen, "Long-wave optics," *IEEE Transactions on Microwave Theory and Techniques*, vol. 41, no. 10, pp. 1676–1690, 1993.

[44] N. J. McEwan and P. F. Goldsmith, "Gaussian beam techniques for illuminating reflector antennas," *IEEE transactions on antennas and propagation*, vol. 37, no. 3, pp. 297–304, 1989.

[45] A. Bogush and R. Elkins, "Gaussian field expansions for large aperture antennas," *IEEE Transactions on Antennas and Propagation*, vol. 34, no. 2, pp. 228–243, 1986.

[46] R. K. Arora and Z. Lu, "Graphical depiction of the electromagnetic fields of Hermite-Gaussian modes," *IEE Proceedings H*, vol. 139, no. 4, pp. 369–375, 1992.

[47] ——, "Graphical study of Laguerre-Gaussian beam modes," *IEE Proceedings*, vol. 141, no. 3, pp. 145–150, 1994.

[48] D. Gabor, *Theory of Communication*. Institution of Electrical Engineering, 1946.

[49] M. J. Bastiaans, "Gabor's expansion of a signal into Gaussian elementary signals," *Proceedings of the IEEE*, vol. 68, no. 4, pp. 538–539, 1980.

[50] P. D. Einziger, S. Raz, and M. Shapira, "Gabor representation and aperture theory," *Journal of the Optical Society of America A, Optics and Image Science*, vol. 3, no. 4, pp. 508–522, 1986.

[51] P. D. Einziger and S. Raz, "Beam-series representation and the parabolic approximation: The frequency domain," *Journal of the Optical Society of America A, Optics and Image Science*, vol. 5, no. 11, pp. 1883–1892, 1988.

[52] J. J. Maciel and L. B. Felsen, "Discretized Gabor-based beam algorithm for time-harmonic radiation from two-dimensional truncated planar aperture distributions .I. formulation and solution," *IEEE Transactions on Antennas and Propagation*, vol. 50, no. 12, pp. 1751–1759, 2002.

[53] ——, "Discretized Gabor-based beam algorithm for time-harmonic radiation from two-dimensional truncated planar aperture distributions .II. asymptotics and numerical tests," *IEEE Transactions on Antennas and Propagation*, vol. 50, no. 12, pp. 1760–1768, 2002.

[54] H.-T. Chou, P. H. Pathak, and R. J. Burkholder, "Novel Gaussian beam method for the rapid analysis of large reflector antennas," *IEEE Transactions on Antennas and Propagation*, vol. 49, no. 6, pp. 880–893, 2001.

[55] P. Schott, F. Lemaître, and O. Pascal, "Use of Gaussian beams to compute antenna pattern," *Annals of Telecommunications*, vol. 57, no. 7, pp. 775–797, 2002.

[56] A. Chabory, J. Sokoloff, S. Bolioli, and P. F. Combes, "Computation of electromagnetic scattering by multilayer dielectric objects using Gaussian beam based techniques," *Comptes Rendus Physique*, vol. 6, no. 6, pp. 654–662, 2005.

[57] A. Chabory, J. Sokoloff, and S. Bolioli, "Novel Gabor-based Gaussian beam expansion for curved aperture radiation in dimension two," *Progress In Electromagnetics Research*, vol. 58, pp. 171–185, 2006.

[58] A Chabory, J Sokoloff, and S Bolioli, "Physically based expansion on conformal Gaussian beams for the radiation of curved aperture in dimension 2," *IET Microwaves, Antennas & Propagation*, vol. 2, no. 2, pp. 152–157, 2008.

[59] A. Chabory, J. Sokoloff, and S. Bolioli, "Physics-based expansion on 3D conformal Gaussian beams for the scattering from a curved interface," *Progress In Electromagnetics Research B*, vol. 54, pp. 245–264, 2013.

[60] C.-A. L'Hour, "Modélisation de la propagation electromagnétique en milieux inhomogènes basée sur les faisceaux Gaussiens - application à la propagation en atmosphère réaliste et à la radio-occultation entre satellites," PhD thesis, Université Paul Sabatier-Toulouse III, 2017.

[61] A. Grossmann and J. Morlet, "Decomposition of Hardy functions into square integrable wavelets of constant shape," *SIAM Journal on Mathematical Analysis*, vol. 15, no. 4, pp. 723–736, 1984.

[62] S. Mallat, *A Wavelet Tour of Signal Processing*. Academic press, 1999.

[63] A. Iqbal and V. Jeoti, "A split step wavelet method for radiowave propagation modelling in tropospheric ducts," in *IEEE International on RF and Microwave Conference (RFM)*, 2011, pp. 67–70.

[64] ——, "Numerical modeling of radio wave propagation in horizontally inhomogeneous environment using split-step wavelet method," in *4th International Conference on Intelligent and Advanced Systems (ICIAS)*, 2012, pp. 200–205.

[65] W. C. Chew, "Electromagnetic theory on a lattrice," *Journal of Applied Physics*, vol. 75, no. 10, pp. 4843–4850, 1994.

[66] F. L. Teixeira and W. C. Chew, "Lattice electromagnetic theory from a topological viewpoint," *Journal of Mathematics and Physics*, vol. 40, no. 1, pp. 169–187, 1999.

[67] D. J. Donohue and J. Kuttler, "Propagation modeling over terrain using the parabolic wave equation," *IEEE Transactions on Antennas and Propagation*, vol. 48, no. 2, pp. 260–277, 2000.

[68] R. Janaswamy, "A curvilinear coordinate-based split-step parabolic equation method for propagation predictions over terrain," *IEEE Transactions on Antennas and Propagation*, vol. 46, no. 7, pp. 1089–1097, 1998.

[69] E. K. Smith and S. Weintraub, "The constants in the equation for atmospheric refractive index at radio frequencies," *Proceedings of the IRE*, vol. 41, no. 8, pp. 1035–1037, 1953.

[70] P. L. Rice, A. G. Longley, K. A. Norton, and A. P. Barsis, "Transmission loss predictions for tropospheric communication circuits," Institute for Telecommunication Sciences and Aeronomy Boulder Co, Tech. Rep., 1967.

[71] D. J. Thomson and N. R. Chapman, "A wide-angle split-step algorithm for the parabolic equation," *The Journal of the Acoustical Society of America*, vol. 74, no. 6, pp. 1848–1854, 1983.

[72] T. Huckle, "Fast transforms for tridiagonal linear equations," *BIT Numerical Mathematics*, vol. 34, no. 1, pp. 99–112, 1994.

[73] L. Brekhovskikh, *Waves in the Layered Media*. Academic Press, 1976.

[74] A. R. Miller, R. M. Brown, and E. Vegh, "New derivation for the rough-surface reflection coefficient and for the distribution of sea-wave elevations," *IEE Proceedings H*, vol. 131, no. 2, pp. 114–116, 1984.

[75] J. R. Kuttler and R. Janaswamy, "Improved Fourier transform methods for solving the parabolic wave equation," *Radio Science*, vol. 37, no. 2, pp. 1–11, 2002.

[76] G. A. Deschamps, "Gaussian beam as a bundle of complex rays," *Electronics Letters*, vol. 7, no. 23, pp. 684–685, 1971.

[77] A. Chabory, C. Morlaas, R. Douvenot, and B. Souny, "An exact spectral representation of the wave equation for propagation over a terrain," in *International Conference on Electromagnetics in Advanced Applications (ICEAA)*, 2012, pp. 717–720.

[78] R. Janaswamy, "Radio wave propagation over a nonconstant immittance plane," *Radio Science*, vol. 36, no. 3, pp. 387–405, 2001.

[79] A. Chabory, C. Morlaas, and R. Douvenot, "An exact vectorial spectral representation of the wave equation for propagation over a terrain in 3D," in *IEEE-APS Topical Conference on Antennas and Propagation in Wireless Communications (APWC)*, 2013, pp. 907–910.

[80] M. Abramowitz and I. A. Stegun, *Handbook of mathematical functions*. NBS, 1966.

[81] R. F. Harrington, *Time-Harmonic Electromagnetic Fields*, D. G. Dudley, Ed. McGraw-Hill, New York, 1961.

[82] F. B. Jensen, W. A. Kuperman, M. B. Porter, and H. Schmidt, *Computational Ocean Acoustics*. Modern Acoustics and Signal Processing, 2011.

[83] Y.-S. Lin, T. F. Duda, and A. E. Newhall, "Three-dimensional sound propagation models using the parabolic-equation approximation and the split-step Fourier method," *Journal of Computational Acoustics*, vol. 21, no. 01, p. 1 250 018, 2013.

[84] M. E. Austin and N. R. Chapman, "The use of tessellation in three dimensional parabolic equation modeling," *J. Comp. Acous.*, vol. 19, no. 3, pp. 221–239, 2011.

[85] C. L. Pekeris, "Accuracy of the Earth-flattening approximation in the theory of microwave propagation," *Physical Review*, vol. 70, no. 7-8, p. 518, 1946.

[86] Y. A. Kravtsov and Y. I. Orlov, *Geometrical Optics of Inhomogeneous Media*. Springer-Verlag, 1990.

[87] R. Douvenot and V. Fabbro, "On the knowledge of radar coverage at sea using real time refractivity from clutter," *IET Radar, Sonar Navigation*, vol. 4, no. 2, pp. 293–301, 2010.

[88] P. A. Ingwersen, W. Z. Lemnios, and M. L. Stone, "Radars for ballistic missile defense research," *Lincoln Laboratory Journal*, vol. 12, no. 2, 2001.

[89] S. G. Mallat, "Multiresolution approximations and wavelet orthonormal bases of $L^2(R)$," *Transactions of the American Mathematical Society*, vol. 315, no. 1, pp. 69–87, 1989.

[90] C. Van Loan, *Computational Frameworks for the Fast Fourier Transform*, ser. Frontiers in Applied Mathematics. SIAM, 1992.

[91] D. Lugara, C. Letrou, A. Shlivinski, E. Heyman, and A. Boag, "Frame-based Gaussian beam summation method: Theory and applications," *Radio Science*, vol. 38, no. 2, 2003.

[92] J. J. Maciel and L. B. Felsen, "Systematic study of fields due to extended apertures by Gaussian beam discretization," *IEEE transactions on antennas and propagation*, vol. 37, no. 7, pp. 884–892, 1989.

[93] V. Cerveny, M. M. Popov, and I. Psencik, "Computation of wave fields in inhomogeneous media-Gaussian beam approach," *Geophysical Journal International*, vol. 70, no. 1, pp. 109–128, 1982.

[94] M. Leibobich and E. Heyman, "Beam summation theory for waves in fluctuating media. part I: The beam-to-beam scattering matrix," in *URSI International Symposium on Electromagnetic Theory (EMTS)*, 2016, pp. 367–370.

[95] M. Leibovich and E. Heyman, "Beam summation theory for waves in fluctuating media. part II: Stochastic fields," in *URSI International Symposium on Electromagnetic Theory (EMTS)*, 2016, pp. 371–374.

[96] S. G. Mallat, "A theory for multiresolution signal decomposition: The wavelet representation," *IEEE transactions on Pattern Analysis and Machine Intelligence*, vol. 11, no. 7, pp. 674–693, 1989.

[97] I. V. Lindell, *Methods for Electromagnetic Field Analysis*. Oxford Univ. Press, 1992.

[98] H. Galiègue, "Modélisation des effets des scintillations ionosphériques sur la propagation des ondes electromagnétiques en bande L aux latitudes polaires," PhD thesis, Université Paul Sabatier-Toulouse III, 2015.

[99] R. Bertrand, "Modélisation de la propagation pour de la radio occultation GNSS," Ecole Nationale de l'Aviation Civile, Mémoire de fin d'études, 2017.

[100] International Telecommunication Union, "Propagation in non-ionized media," *Reports of the CCIR*, vol. 5, 1990.

[101] A. Iqbal and V. Jeoti, "A split step wavelet method for radiowave propagation modelling in tropospheric ducts," in *IEEE International RF and Microwave Conference (RFM)*, 2011, pp. 67–70.

[102] J. Gardner and R. E. Collin, "An accurate closed-form approximate representation for the Hankel function of the second kind," *IEEE Transactions on Antennas and Propagation*, vol. 48, no. 10, pp. 1699–1700, 2000.